Near-Boundary Flow Phenomena in Unmanned Aerial/Underwater Vehicles

Darius Carter

A Dissertation
Presented to the Faculty
of University of Virginia
in Candidacy for the Degree
of Doctor of Philosophy

Recommended for Acceptance
by the Department of
Mechanical and Aerospace Engineering
Advisor: Daniel B. Quinn

University of Virginia
December 2021

Abstract

The growth of the Unmanned Aerial and Underwater Vehicle (UAUV) industry is outpacing our understanding of how UAUVs behave in near boundary environments. Search and rescue UAUV applications occur in tight, confined spaces filled with complex obstacles and boundaries. Water sampling UAUV applications occur over wide-open water bodies that involve amphibious operations such as breaching the water's surface. Near-boundary flight provides aerodynamic benefits, such as the "ground effect," seen in animals and helicopters. However, near-boundary flight advantages can be hard to harness because boundary effects can also be destabilizing. They perturb lift (near ground-air or water-air boundaries) and introduce a chaotic amphibious transition region (near water-air boundaries). We studied the aerodynamics and performance of rotor blades near solid and liquid surfaces to explore these near-boundary effects. We then conducted a study of how Micro Aerial Vehicles interact in near-boundary situations and how their aerodynamic performance is affected by the ground. Third, we explored various applications that leverage the advantages of near-boundary flight. Lastly, we compared ground effect over water and solid ground surfaces. The flow structures discovered in this work can quantify the benefits of the near-boundary flight UAVs and offer design strategies for UAUVs that can fly more stably in these near boundary scenarios.

Acknowledgements

First and most important I would like to thank God for protecting and providing for me during this journey. With out his support and love I would not be able to accomplish all of this.

”In their hearts humans plan their course, but the Lord establishes their steps” - Proverbs 16:9

A special thank you to my family and friends for all your support throughout these years at UVA. I especially want to give thanks to my immediate family for all the late night phone calls, jokes in the group chat, and always welcoming me home with open arms when I went home. I want to thank my girlfriend Michelle for always being my soundboard during this process. Special thank you to my lab mates, co-workers at Biltmore and Crozet Pizza, my basketball teams, Alpha Phi Alpha Fraternity brothers, National society of black engineers, and my countless other friends and mentors.

Research wise I would be reminisced if I don’t take time to recognize my advisor Daniel Quinn and my undergraduate advisor Eric Loth. Eric thank you so much for sparking a fluids research passion in me and supporting me all these years. PS I still owe you one more noon basketball beating. Daniel you have single handily changed my life forever and i owe you the world for everything these past years. Every time life threw me a curve ball you were always there with a smile and ready to assist me. Daniel your passion for teaching and mentoring has rubbed off on me and all I want is to give at least of fraction of this to my future students.

I want to thank my committee members (Lin MA, Haibo Dong, & Matt Reidenbach) for taking time to mentor, support, and advise me throughout this journey. If i forgot to mention anyone else please don't charge to me I love and thank you all for being apart of my life.

The work presented in this thesis was supported by the University of Virginia and the National Science Foundation (# 1921809; Program Manager: Ron Joslin).

Contents

Abstract i

Acknowledgements ii

Nomenclature xiii

1 Introduction 1

1.1 Background and Motivation 1

1.2 Ground Effect Modeling and Rotor Design Dependency 4

1.3 Influence of the Ground, Ceiling, and Side Wall on Micro Quadrotors . . . 6

1.4 Near-Boundary Flight Applications 7

1.5 Rotor Property Dependencies in Solid/Water Ground Effect 8

1.6 Research Summary and Questions 9

2 Development of Two Arenas for Quantifying Rotorcraft Performance 12

2.1 Particle Image Velocimetry 13

2.2 Isolated Rotor Ground Effect Arena 15

2.2.1 Version 1.0 15

2.2.2 Version 2.0 17

2.3 Micro Aerial Vehicle Arena 22

2.4 Summary 28

3 Ground Effect Modeling and Rotor Design Dependency 29

3.1 Experiment Setup and Methods 29

3.2 Modeling 33

3.3 Results 36

3.3.1 Experimental Results 36

3.3.2 Differences between Model and Results 38

3.3.3 PIV Results 39

3.4 Discussion 42

3.5 Conclusion 45

4 Influence of the Ground, Ceiling, and Side Wall on Micro Quadrotors 47

4.1 Introduction 47

4.2 Experimental Methods 48

4.3 Mathematical Models 50

4.4 Results 52

4.4.1 Tethered force measurements 52

4.4.2 Flowfield measurements 54

4.5 Discussion 57

4.6 Conclusion 59

5 Near-Boundary Flight Applications 60

5.1 Surface Detection 60

5.2 Near-Boundary Optimal Path Planning 63

5.3 Near-Boundary Simulations 66

5.4 Multi-Vehicle Interaction Simulation 69

5.5 IMU Wind Estimation 73

5.6 Conclusion 75

6 Rotor Property Dependencies in Solid/Water Ground Effect 77

6.1 Isolated Rotor over Water 78

6.1.1 Experiment Setup and Methods 78

6.1.2 Results 79

6.1.3 Discussion 85

6.2 Dual air and water PIV 88

6.2.1 Experimental Setup: Version 1 88

6.2.2 Experimental Setup: Version 2 89

6.2.3 Results 91

6.3 Conclusion 93

7 Concluding Remarks and Future Work 94

7.1 Development of Two Arenas for Quantifying Rotorcraft Performance 94

7.2 Ground Effect Modeling and Rotor Design Dependency 95

7.3 Influence of the Ground, Ceiling, and Side Wall on Micro Quadrotors . . . 95

7.4 Near-Boundary Flight Applications 96

7.5 Rotor property dependencies in solid/water ground effect 97

7.6 Broader Impacts and Future Work 98

References 99

List of Figures

1.1 Examples of various UAVs completing designated tasks in near-boundary situations. A) Navigating into a cave [5] B) Search and rescue mission in glacier canyon C) Water sampling UAV floating on water surface [6] D) UAV conducting Bridge inspection [7] E) Waterproof UAV launching from the water's surface [8] F) UAV platform that is capable of operating in both air and water descending to the water's surface. [9] 3

2.1 a) Hsaio & Chirarattananon's [17] ceiling effect experiment utilizing two tethered Crazyflie rotors. b,c) Sanchez et al.'s [16] ground effect experiment utilizing tethered rotor or quadrotor platform. 12

2.2 PIV setup used to conduct imaging of a rotor in ground effect. A schematic showcasing the necessary components of our PIV system. 14

2.3 Image pairs vs. velocity field error. A convergence test indicated the number of image pairs needed to converge to a steady state wake field under our MAV at its highest attainable throttle. 15

2.4 Version 1.0 CAD and prototype of the isolated rotor test rig. 16

2.5 Version 2.0 CAD (top left) and prototype (top right) of the isolated rotor test rig. Bottom: Schematic of the experimental arena including PIV location, water boundary, rotor system, & counterweight. 19

2.6 Control diagram showing connections used to operate rotor and collect data signals in the isolated rotor test rig. 20

2.7 Architecture of the code and the testing sequence for the isolated rotor test rig. 21
2.8 Top: Picture of the untethered MAV arena. Bottom: Schematic of arena including PIV system, near-boundary controller, motion capture system, and MAVs. 25
2.9 MAV flight arena: control scheme utilizing our host computer to control the linear actuation as well as data collection and the Crazyflie commands. 26
2.10 Architecture of the code and the testing sequence for the tethered MAV near-boundary arena. 27
2.11 Flight altitude of two MAVs (one unperturbed and other crosses under wake of a tethered MAV) in the MAV flight arena. As the MAV crosses under the wake of the tethered MAV, its flight path was altered. 27

3.1 Left: Equipment used to measure performance of a isolated rotor. Right: Schematic of rotor above solid boundary with location of laser sheet and camera Field of View. 30
3.2 Comparison of blade pitch and diameter of our test rotors to commercially popular UAV platforms. 31
3.3 Aerodynamic forces on a rotor element in Blade Element Theory. [44] . . . 33
3.4 Top: BET combined with C-B Model shows the frequency needed to lift the experimental rig's weight. Bottom: Frequencies needed to hover at the near-boundary distances. 37
3.5 Absolute error between experimental data and model results. Left: Average error at all the distances for each rotor type. Right: Error versus distance to the ground. 38
3.6 Potential flow model of one source and mirror simulation ground as well as doublet distribution and mirror. Right: Time-averaged PIV flow field from our data set (Rotor D: 0.28 m, Pitch: 7 in, & $\hat{Z}$: 1) 39

3.7 Time-Averaged PIV flow fields for rotor diameters 25 cm & 28 cm at all 3 pitches. 40
3.8 Velocity cross section at 1/6 radius below rotor midplane at $\hat{Z}$: 2,1,0.66. . . 41

4.1 A glass arena was used to measure the lift of a tethered Crazyflie and the surrounding flow field via Particle Image Velocimetry (PIV). 50
4.2 A comparison of recent modelled and experimental data for quadrotors near the sidewall, ceiling, and ground [27][26][16][13][17][25]. 53
4.3 Time-averaged velocities near the ground ($\hat{Z} = 3.4$, center) and ceiling ($\hat{Z} = 2$, right) differ in direction and strength compared to the control ($\hat{Z} \gg 1$, left). Velocity cross-sections shown below. 54
4.4 Time-averaged velocities near the ceiling/ground are compared against the control to highlight areas of high variation. 55
4.5 Time-averaged velocities near a horizontally tilted ground plane show the sensitivity of the Crazyflie's wake to tilt angle. 57

5.1 a) Models and experimental data showcasing thrust changes due to near boundary flights preformed at UVA. b,c) Descending and ascending quadrotor data with fitted model of throttle 61
5.2 a) Time captured images of the descending and landing quadrotor b) Thrust vs time graph c) Descending quadrotor data with colors showing the three stages of landing 63
5.3 a) The paths chosen for landing including one optimized to benefit from near-boundary effects. b) Time capture of the quadrotor in testing. c) Throttle used to hover during testing sequence. 64
5.4 Frequency of Crashing due to the effects of near boundary flights 67

5.5 Left: vector field representations of each of the six flow field models used for the simulation. Right: example traces of simulated quadrotor flight through each of the flow fields. 70
5.6 Simulated flight paths at the faster of the two flight velocities. The averaged experimental data is shown for comparison. 72
5.7 Above: MAV arena and testing equipment. Below: Data connections and Picture of Arena. 74
5.8 Hover forces and motor levels on a rotor during still and gusted conditions. . 75

6.1 Left: Setup used to measure performance of the isolated rotor. Right: Schematic of rotor above water boundary with location of laser sheet and camera FOV. 78
6.2 Top: Blade Element Theory combined with C-B Model to show the frequency needed to lift the experiments rig's weight. Middle: Hover frequency required to hover above the ground. Bottom: Hover frequency required to hover above water surface. 80
6.3 Absolute error between experimental data and model results. Left: Average error at all the distances for each rotor type. Right: Error versus distance to the ground or water. 82
6.4 Time-Averaged PIV flow fields of for rotor diameters 25 cm & 28 cm at all 3 pitches. 83
6.5 Averaged water shape from raw images (photo composite made in Adobe Photoshop). 84
6.6 Wake jet directions 84
6.7 Velocity cross sections at two distances between the rotor and the ground and water surface. 85
6.8 Version 1 laser and camera set up. 88
6.9 Camera set up for dual fluid imaging 90

6.10 Left: Stitched still of seeded flow. Right: Time resolved velocity vector field. 91

6.11 Left: Stitched still of seeded flow. Right: Time resolved vorticity field. . . 92

List of Tables

2.1 Rotor Rig Equipment Parameters 17

2.2 MAV Arena Equipment Parameters 22

3.1 Experiment Parameters 32

4.1 Distances from the boundary during tethered experiments 49

5.1 Experimental results of predicted and measured energy* 65

Nomenclature

α	Angle of attack
ΔL	Relative change in lift near a boundary
ℓ	Relative change in lift near a boundary
$\hat{\ell}$	ℓ scaled by rotor radius
$\hat{E_{Traj}}$	Total energy during trajectory
$\hat{Z}$	Z scaled by rotor radius ($\hat{Z} \equiv Z/r$)
$\hat{z}_0$	z_0 scaled by rotor radius ($\hat{z}_0 \equiv z_0/r$)
ψ	Angle between plane of rotation and airflow
ρ	Density of air
θ	Airfoil section pitch angle
θ_{tilt}	Horizontal tilt angle between quadrotor and boundary
$\vec{u}$ & $\vec{v}$	In-plane flow velocity
$\vec{u}_\infty$	In-plane flow velocity far from boundaries
c	Chord
C_d	Drag Coefficient

C_l	Lift Coefficient
C_P	Rotor power coefficient
C_T	Coefficient of Thrust
D	Drag Force
d	Rotor diameter
F	Total Thrust
f	Rotor frequency
g	Acceleration due to gravity
I	Vehicle rolling moment of inertia
L	Lift Force
$L^{'}$	Simulated lift disturbance
L_∞	Lift far from the boundary
m	Vehicle mass
P	Power
r	Rotor radius
T	Thrust Force
V	Local air velocity
Z	Distance of rotor from boundary
z_0	Target height (of the rotor)
IMU	Inertial Measurement Unit

J Rotor advance ratio

Chapter 1

Introduction

1.1 Background and Motivation

Unmanned Aerial Underwater Vehicles (UAUV) are growing in popularity due to their low cost, high agility, and amphibious ability. Applications of such vehicles include mobile sonobuoys, water sampling seen in Figure 1.1 [1], and identification of unexploded ordnance such as naval mines [2]. Multirotor UAUVs are especially useful due to their precise movements and agility, which allow them to navigate narrow corridors such as those of urbanscapes and collapsed mines – places that are inaccessible to conventional aerial vehicles. The key to unlocking and utilizing a UAUV's full potential lies in the intersection of aerodynamics and the fluid-structure interactions as they encounter these different near-boundary conditions.

A key challenge of designing UAUV systems, especially micro UAUVs, is that they are easily destabilized by flow changes caused by near-boundary flight, which compromises their inherent safety and reliability [3]. The dangers of the destabilization include the safety of the physical UAUV platform as well as the safety of any surrounding vehicles, animals, or humans. In tight spaces like in Figure 1.1 parts a & b, solid boundaries create complex viscous flows around the UAUV [4]. Instabilities are seen in vehicles as they near water or solid boundaries due to interactions with this boundary. These instabilities alter the predicted flight performance of the UAUV, which can lead to unintended maneuvers and crashes [1].

While boundaries and turbulent fluctuations can alter flight performance, they also offer flight benefits to animals. Herring gulls utilize ”ground effect” to decrease their cost of transport [10]. This ground effect also applies to skimmers, pelicans, and myotid bats, which fly and forage close above water [11]. Ground effect has been shown to increase lift-to-drag ratios near both solid and water surfaces for flying fish [12]. UAV platforms have also utilized this benefit near the water surface as seen in Figure 1.1 parts c & e.

Near-boundary flight for an UAUV can offer beneficial flight opportunities that increase the efficiency and range of flight missions. As an UAUV approaches the ceiling or ground, studies show an increase in lift [13] [14] [15]. This increase in lift means that less power is necessary to maintain hovering, which could extend flight times and increase energy efficiency. As with solid boundaries, liquid boundaries also enhance lift-to-drag ratios, as seen in flying fish [11]. This increase in thrust and efficiency may also be seen when the UAUV is just below the surface utilizing the ceiling effect.

Existing studies and modeling of a UAUV’s response to disturbances are based on classical, high Reynolds number aerodynamic theories that were initially created for fixed-wing aircraft and helicopters. The helicopter ground effect theory [13] has been applied by many studies but assumes inviscid flow, which breaks down for lower Reynolds number UAUVs. There have been attempts to update this model to UAUVs, but they tend to neglect the effects of viscous forces [16] [17]. With the water-air boundary, there is a lack of understanding in how flow structures develop from a multirotor vehicle. Understanding this phenomena better would lead to safer boundary flight and more predictable flight performance near air-water boundaries. In an effort to utilize these near boundary benefits for UAV vehicles, we explored ways to increase our understanding of near-boundary flows.

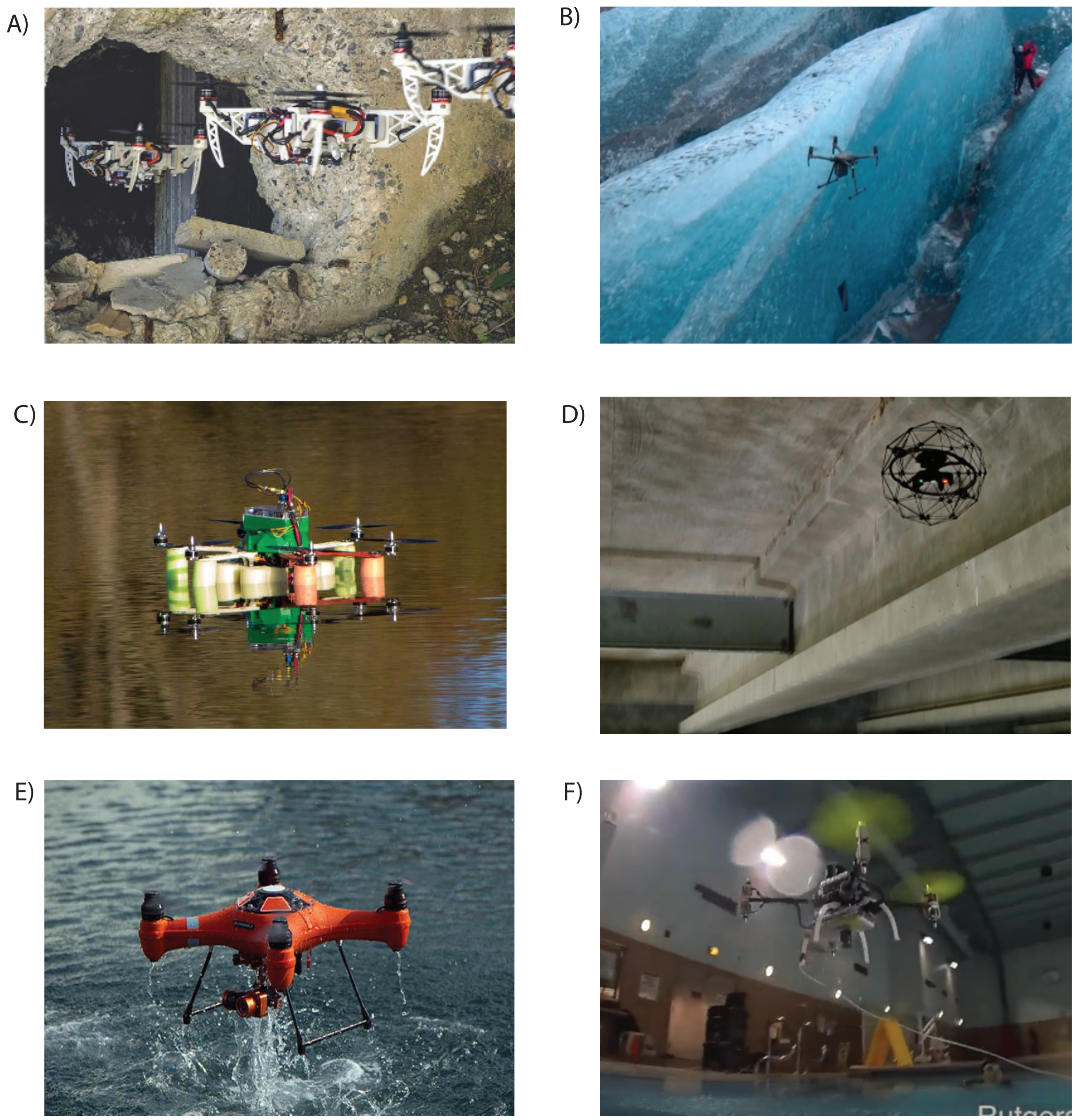

Figure 1.1: Examples of various UAVs completing designated tasks in near-boundary situations. A) Navigating into a cave [5] B) Search and rescue mission in glacier canyon C) Water sampling UAV floating on water surface [6] D) UAV conducting Bridge inspection [7] E) Waterproof UAV launching from the water's surface [8] F) UAV platform that is capable of operating in both air and water descending to the water's surface. [9]

1.2 Ground Effect Modeling and Rotor Design Dependency

The challenge of physics-driven control in UAVs is that there are various scales and multi-rotor interactions that put them in a flow regime with unique challenges compared to traditional aircraft. Because the Reynolds number (a ratio of inertial forces to viscous forces) is much lower for MAVs, phenomena such as separation, transition, and reattachment affect flight performance in ways that are less important for traditional fixed-wing aircraft [18]. Over decades of research in the early 1900s, scaling laws were developed for the flow physics of traditional aircraft. We are entering a new era of developing scaling laws for the flow physics of UAVs. Moving forward, disk actuator theory (which governs rotor thrust at high Reynolds number) will have to be combined with boundary layer theory (which governs viscous friction over surfaces) and separation theory (which governs detached flows that occur at low Reynolds number) to give more accurate scaling laws.

Previous studies of the flow around quadrotors have focused on flight far from obstacles. Motivated by the failure of traditional inviscid scalings, research groups have used Computational Fluid Dynamics (CFD) to simulate the full equations of motion. These computations rely on RANS (Reynolds-Averaged Navier Stokes), LES (Large Eddy Simulation), or DES (Detached Eddy Simulation, a RANS-LES hybrid) modeling, because resolving viscous length scales in a turbulent rotor wake is not possible with current technology. For the DJI Phantom and SUI Endurance, DES simulations slightly overpredict thrust (by $\approx 2\%$) and underpredict power (by $\approx 10\%$) [19]. DES simulations have also been used to study rotor spacing, where they predict the normalized vertical force coefficient to drop at small rotor separation distances [20]. However, experiments on Phantom-II-inspired rotors suggest that rotor spacing has a minimal effect on thrust, and instead increases thrust fluctuations and aeroacoustic noise [21]. By using Particle Image Velocimetry (PIV), the researchers were able to isolate regions of the flow responsible for these discrepancies, thereby offering suggestions for improved meshing in CFD [21].

One area where the failure of traditional models is especially noticeable is near obstacles. Near-obstacle flight is commonplace for MAVs. For example, they deal with ceiling effects when examining bridges [22] and with ground effects when performing blind terrain mapping [23] or navigating inside multi-floor buildings [24]. In general, flying near the ground leads to a boost in rotor lift due to stagnation or suction zones. Classic momentum theory predicts that lift increases by a factor of $(1 - (4\hat{z})^{-2})^{-1}$, where $\hat{z}$ is the ceiling/ground proximity normalized by rotor radius [13]. This relation is derived for single-rotor helicopters in forward flight; it assumes that viscous effects are negligible and that $\hat{z} > 0.5$. It has recently been shown that the theory over-predicts ceiling effects [25] and under-predicts ground effects [26, 27] when applied to small quadrotors. It remains unclear how these models scale with rotor size, and what flow features are responsible for lift scaling differently near the ground.

Better flow models can also be exploited to improve situational awareness. The 2016 Road map for US Robotics (a summary of progress and directions in robotics put together by 19 top robotics universities) makes it clear that better situational awareness is crucial for the next generation of robots. According to the Road map, key focus areas for robotics R&D include “richer set[s] of sensors” and a “leap in performance in terms of situational awareness” [28]. By monitoring thrust and comparing to predictive flow models, MAVs could estimate distance to nearby boundaries, similar to the way some helicopters factor ground effect into their altitude controllers to avoid crash-landings [29]. A thrust-based detection scheme could work even when landing in a dark, dusty environment, where camera, sonar, or lidar-based sensors may be inaccurate. Thrust-based detection could even replace bulky autonomous landing sensors that increase payload and require extra computational capabilities.

1.3 Influence of the Ground, Ceiling, and Side Wall on Micro Quadrotors

Micro Aerial Vehicles (MAVs) are growing in popularity due to their small size and indoor flight ability. Quadrotors are especially useful because of their ability to hover and perform precise movements. Their small size lets quadrotors navigate in narrow corridors that are inaccessible to conventional vehicles. However, these new environments lead to new challenges. Micro quadrotors are inherently unstable due to their small size and low speeds [3, 30, 31], and they can be further destabilized by their close proximity to boundaries like walls, grounds, and ceilings [4].

One solution for handling near-boundary effects is to use data-driven control. Reinforcement learning [4] and adaptive control [32], for example, have been used to train quadrotors to fly near boundaries, and centralized predictive interaction control has helped protect quadrotors from crashing into the ceiling [33]. However, even in simple environments, model uncertainty can cause data-driven quadrotor controllers to fail [34]. Aerodynamic models are therefore incorporated into many controllers to improve performance. Some state estimators have used blade element theory [35] or wind models [36] to improve stability. In other cases, aerodynamic models have enabled control compensation in near-boundary maneuvers and landings [23, 37, 38, 39].

When high-precision control is not necessary, data-driven reactive approaches may be sufficient. However, many high-impact quadrotor applications – package delivery in crowded buildings, search-and-rescue in rubble corridors, coordinated swarming, etc. – require centimeter-scale precision. Data-driven control is especially problematic if sensors are compromised by sand/dust or low lighting, because the limited payload capacity of quadrotors may preclude redundancy in their sensing systems [18]. Another key advantage of using model-based control is its importance to the future of MAV regulation. As MAVs become more mainstream, their regulation will demand physics-based models that can guarantee provably safe operation.

A challenge of model-based quadrotor control near boundaries is that existing models are rooted in helicopter theories. These classic theories use the method of images to model a helicopter's lift near the ground [13]. However, quadrotors have three additional rotors, and their smaller Reynolds numbers lead to viscous effects that are negligible at helicopter scales [15]. Recently, classic theories have been adapted with an empirical coefficient that accounts for the extra rotors [16]. Ceiling and sidewall effects have no history in helicopter research, so they are relatively unexplored in comparison. The first attempt at a near-ceiling model was made by Hsaio & Chirarattananon [17], who used blade element momentum theory to predict the increased lift seen near the ceiling. New models have inspired recent analytical and experimental studies that clearly demonstrate the advantages of near-ceiling flight, which are particularly relevant for bridge-inspection MAVs [22, 40, 41]. How well these near-boundary models apply to micro quadrotors (rotor radius $r \lesssim 50$ mm) is unknown.

1.4 Near-Boundary Flight Applications

One major issue common to all UAV platforms is that they are not energy efficient. Their battery life is short and is often the main factor limiting deployment in real-world applications. Adding payloads such as sensors further decreases their mission time due to the increase in weight and energy consumption associated with the operation of the added device.

When a UAV flies near the ground or ceiling, it experiences an increase in lift. This lift increase represents a decrease in the thrust required to keep the UAV aloft and thus a decrease in energy consumption. For example, in agricultural operations, a UAV could fly low to the ground to reduce energy consumption, especially over long distances. In indoor environments, a UAV could fly close to the ceiling, avoiding crowds and objects while also consuming less energy. A secondary desired effect is that by monitoring thrust, the UAV can detect the distance to nearby surfaces and prevent collisions. This latter effect is especially beneficial in environments where sensors may not be able to estimate the distance from the ground/ceiling. For example, in a dusty environment like a desert, a conventional camera, sonar, or lidar-based sensor may fail to detect obstacles, which may lead to crashes as a vehicle is landing.

A deeper understanding of near-boundary modeling can be can leveraged for more advanced UAV missions. Understanding the change in a vehicles lift can be used to determine the distance a vehicle is from the ground, because otherwise we would assume the performance to be consistent barring no other adjustments in its environment. We also understand that by increasing lift of a vehicle, we can increase the efficiency of this vehicle's flight. Using this concept, we can develop a way of leveraging efficiency to create more efficient flight paths. As a vehicle gets closer to said boundary, we need a better understanding for how to maintain the safety of this vehicle and avoid crashing.

1.5 Rotor Property Dependencies in Solid/Water Ground Effect

Ground effect has been studied for a long time due to its importance to helicopter landing [13] . Landing on the water is mainly used in what is known as helicopter ditching [42]. No comprehensive study to the author's knowledge has been done on the ground effect phenomenon with multirotors over a water surface. The utility of understanding near-water effects can be seen in examples like water sampling, which can be done over a large lake area shown in Figure 1.1. The energy savings and mission-extending abilities seen in solid boundary ground effect is enough to merit an investigation of near-liquid-boundary effects. Aerodynamic benefits have also been seen in animals flying over the water's surface [11] [12]. However, since most UAUVs are optimized for aerial flights, not understanding this effect physically could lead to instabilities that could cause disastrous crashes.

In comparison to a solid boundary, the ways that air interact with a water surface are different. Water being a fluid itself has the ability to allow for slip at the water surface, unlike a solid surface which has no slip. This slip condition may make the flow more similar to high-Reynolds-number flow models, which may neglect viscosity and therefore have a slip boundary condition. Near-water effects may therefore better match inviscid ground effect flow models such as [43]. Water boundaries are also unlike solid boundaries because they can accept some flux from the air flow. In theory, this could weakened the effectiveness of the overall ground effect by decreasing the interaction the ground has on the induced velocity at the rotor plane. Despite their differences, water and solid ground effects presumably share some features. For example, both must cause the wake to jet outward and change its direction. All of these effects are dependent on the conditions of the flow, which are by products of the vehicle flight conditions as well as the rotor types being utilized. Understanding what rotor factors affect the strength of the solid/liquid ground effect is crucial to developing more accurate physics-based fluid models.

1.6 Research Summary and Questions

The potential in the UAUV field is immense, and the commercial industry is rapidly expanding into various unexplored opportunities. The intersection of aerodynamics and fluid dynamics is crucial to keeping UAUVs and their surroundings safe. Physics-based models, for example, are critical for provably-safe flight. My work contributes to the UAV & UUV community by creating a bridge between fluid dynamics and near-boundary UAUV flight. I designed and built a series of experiments to specifically increase understanding of the fluid dynamics of UAUVs near solid & liquid boundaries. I studied both isolated rotors near solid and liquid surfaces, as well as full MAVs in near-boundary conditions. In each case, I compared the results with invsicid flow models. I also studied how physics-driven near-boundary models can be used in various applications. My work offers ways to strengthen the ties between fluid dynamics and quadrotor flight control – a connection that will be critical to the next generation of ultra-maneuverable UAUVs.

The driving research questions for the remaining thesis chapters is given below:

Chapter 2: Development of Two Arenas for Quantifying Rotorcraft Performance

- How can MAV performance and the surrounding flow fields be measured in tethered and untethered configurations?
- How can the effects of rotor design on near-water/solid boundary interactions be measured?

Chapter 3: Ground Effect Modeling and Rotor Design Dependency

- How does ground effect scale with rotor size and pitch?
- How do the flow features of rotors with various diameters and blade pitches change in ground effect?

Chapter 4: Influence of the Ground, Ceiling, and Side Wall on Micro Quadrotors

- How well do existing near-boundary models apply to MAVs?
- What flow features exist around MAVs as they approach boundaries?

Chapter 5: Near-Boundary Flight Applications

- What implications do ceiling/ground models have for more efficient path-planning and landing?
- What trade-offs exist when utilizing aerodynamic benefits of near-boundary flight?

Chapter 6: Rotor Property Dependencies in Solid/Water Ground Effect

- What is the difference in ground effect performance for rotors near liquid vs. solid boundaries?

- What flow features surround rotors operating near liquid and solid boundaries?

Chapter 2

Development of Two Arenas for Quantifying Rotorcraft Performance

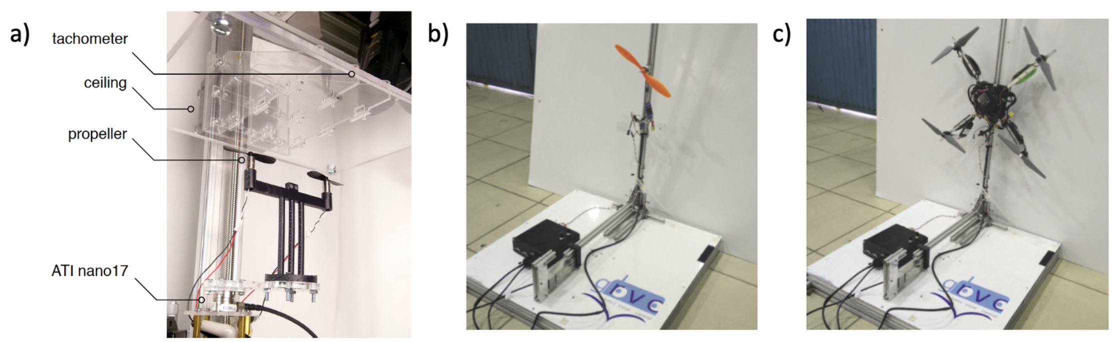

Figure 2.1: a) Hsaio & Chirarattananon's [17] ceiling effect experiment utilizing two tethered Crazyflie rotors. b,c) Sanchez et al.'s [16] ground effect experiment utilizing tethered rotor or quadrotor platform.

This Chapter describes two experimental setups for studying near-boundary flows that I developed. Some comparable experimental setups that were made in the past are seen in Figure 2.1. Sanchez [16] mounted either a rotor or a quadrotor on a force sensor and brought it closer to a solid ground panel to study ground effect. Hsaio & Chirarattananon [17] used a Crazyflie MAV platform and brought it near a solid ceiling panel. We are interested in more versatile experiments such as flow field imaging, untethered UAVs, and different boundary types. My goal was to develop two arenas to allow for various rotors types to be tested as well as untethered and tethered MAV platforms.

2.1 Particle Image Velocimetry

Particle Image Velocimetry (PIV) is a system used to spatially measure flow fields. For my analysis of near-boundary flows, PIV was a critical component in this endeavour. The basic components within a PIV system are a high powered laser, seeding particles, trigger system, and a high-speed camera all seen in Figure 2.2. The fluid is filled to the desired density of seeding particles. The density is chosen to allow for a clear signal-to-noise ratio and resolution of analysis. The particles are neutrally buoyant so that they follow the motions of the fluid. These particles are then illuminated by a sheet of laser light synchronized with a high-speed camera. Images of the fluid are taken at a high frame right showing the particles that are illuminated by the plane of laser light. The image pairs are cross-correlated to measure particle movement in the interrogation area or window. The change in position of the particles within in the interrogation area is used to determine the velocity in the interrogation area. To analyze our near boundary flow data, we created two systems to match the two experimental arenas.

The PIV system was carefully designed to achieve the resolution and frame rate necessary to capture time-averaged near-boundary flow fields. The laser our system used was a dual-cavity pulse laser (Litron, 200 mJ @ 15Hz). This laser has two cavities which gives us the ability to alter the time between pulses depending on the given flow conditions. This was crucial because with our project we measured different rotor combinations and flow conditions. The seeding particles used for our air flow experiments were neutrally-buoyant aerosolized particles of glycol and water (diameter u$\approx$ 14 μm). The particles were created using a fog machine that regulated the particle density in our closed arenas. Particle motion was triangulated by two high-speed cameras (Phantom SpeedSense M341, 4MP) that fed into cross-correlation software (Dantec Dynamic Studio).

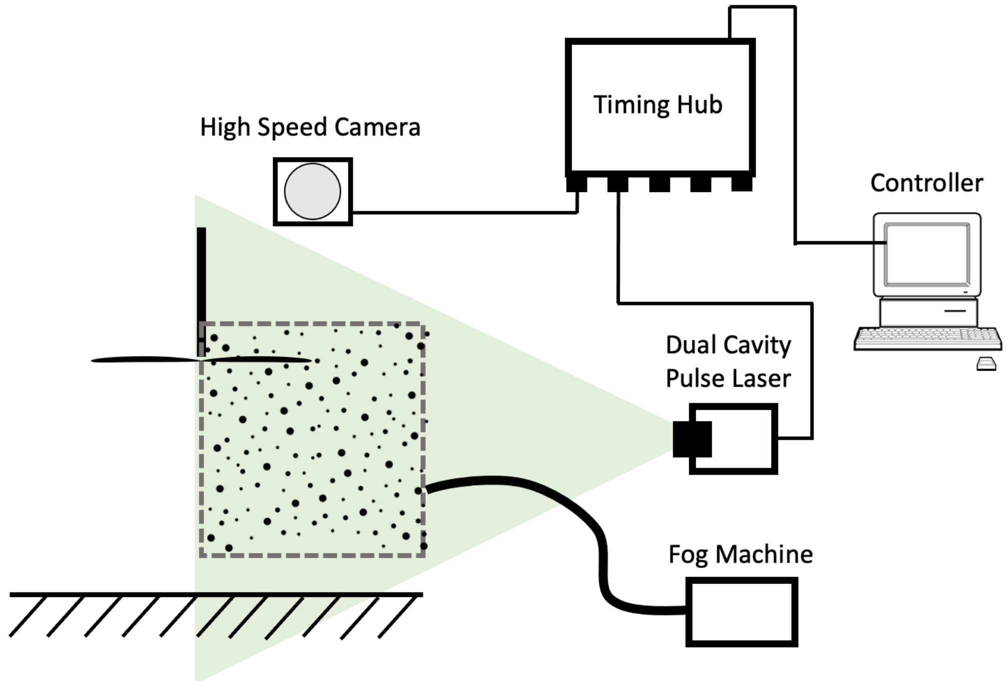

Figure 2.2: PIV setup used to conduct imaging of a rotor in ground effect. A schematic showcasing the necessary components of our PIV system.

Convergence of our PIV images was essential in our PIV analysis to ensure we were capturing steady state flow conditions. Due to limitations of our dual cavity laser, we could only take imaged pairs at 15 Hz which was too slow to resolve the instantaneous flow conditions. We therefore focused on time-averaged flow fields. Convergence graphs were used to make sure the flow vectors showcased the steady state of our system. To find out the convergence of the image pairs, we took the fastest flow condition for our MAV platform (Crazyflie 2.0) experiment and measured 150 image pairs seen in Figure 2.3. We then compared the absolute difference between each each image pair and the average of the past pairs combined. In Figure 2.3, we see that the difference is $< 1\%$ at about 50 image pairs. In an effort to be extra cautious, we chose to do 100 image pairs to be confident we were seeing steady state flow conditions with our PIV images.

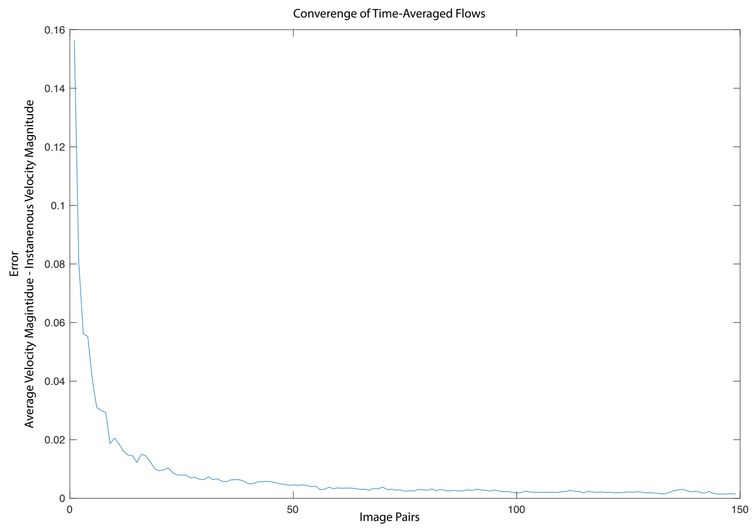

Figure 2.3: Image pairs vs. velocity field error. A convergence test indicated the number of image pairs needed to converge to a steady state wake field under our MAV at its highest attainable throttle.

2.2 Isolated Rotor Ground Effect Arena

The first of the two experimental setups I developed was designed to investigate the ground effect and that measures different rotor designs. Our goal of this rig was to test aerodynamic performance and flow field structure of various rotor configurations in ground effect. A 1m x 1m x 1m glass cube was utilized to allow for water boundaries and to hold in the seeding particles. A design constraint of the system was to create a hovering rotor. The rotor system needed to be able to dynamically move without friction in the Z or lift direction. We made two versions of this systems in which Version 2.0 allowed us to achieve our goal of dynamic rotor ground effect experiments.

2.2.1 Version 1.0

Version 1.0, shown in Figure 2.4, was developed by fellow graduate student Lauren Bouchard and me. Our main goal was to spin a 5 cm four blade propeller at around 3000-5000 revolutions per minute (RPM) to replicate hover conditions of a quadrotor. In Figure 2.4, you

Figure 2.4: Version 1.0 CAD and prototype of the isolated rotor test rig.

can see both the CAD model and prototype of this version. A key component of this design was that we utilized six linear bearings that rode along three stainless steel shafts. The six bearings and three shafts were used to account for the torque force that the propeller would apply to the system especially when operating within a more dense fluid such as water. We also designed a large outer 3D printed cage to make the entire system more stable counteracting the vibrations from the high-speed rotations.

Version 1.0 ultimately did not work due to excessive friction and other design concerns. Aligning the three shafts and linear bearings proved to be very difficult, leading to increased friction. The DC motor we were using added considerable weight to the system, which increased the required rotor speeds. The motor provided more power than was necessary for the size rotor we chose. There was no system to easily switch between the different rotors. Most importantly, the entire rig itself was heavier than the max lift of our rotor, so we were not able to achieve free hovering. In pursuit of our next iteration, we set out to reduce friction and weight, and to use a more efficient DC motor.

2.2.2 Version 2.0

Table 2.1: Rotor Rig Equipment Parameters

Rig Weight	560 grams
Electronic Speed Controller	Castle Talon 35
Encoder	CUI AMT-103-V [15000 RPM Range & 2048 PPR]
Laser Distance Sensor	Sharp GP2Y0A21YK [10 - 80 cm Range]
Motor	DJI E800
Torque Sensor	JNNT [1Nm Range]
Microcontroller	Arduino MEGA
Data Aquistion	National Instruments USB-6009

For Version 2.0 (Figure 2.5), fellow graduate student Qiang Zhong designed and I modified a version with reduced friction and weight. Figure 2.5 shows how we used two shafts and four linear bearings. We utilized the four bearings to counteract the lateral forces and torques created by the rotating rotor. The housing was placed on four linear bearings to allow for low friction in the vertical direction even when torque from the rotor was applied. The friction in the vertical direction was low enough to enable freely hovering rotors. Directly underneath the motor connected to the shaft was an encoder to determine the rotation speed of the rotor. A 4 mm shaft rotated inside a 10 mm tube that was almost the entire length of the shaft. The 10 mm tube contained two flanged rotary bearings on each end used to reduce vibrations and shaft flexing. A laser distance sensor was incorporated above the housing in the rig to measure the location of the housing. The distance of the housing was directly related to the distance of the rotor and the ground boundary. The distance reading was coupled with a PID control system to allow for the system to simulate hover conditions. To decrease the weight of the rig, the frame was recycled from a commercial drone and was made out of carbon fiber. The other experimental components (Table 2.1) were all lighter than in Version 1.0, allowing for dynamic movement of our platform. We switched from a generic DC motor to a specific UAV motor (DJI E800) which was more power dense. A connector was 3D-printed out of ABS to allow for easy switching of various rotors.

Despite the reduced weight, a counterweight system was still needed to counter-act the experimental rig (560 grams). A goal of this experimental rig was to allow for hovering conditions of various rotors including smaller diameters that did not produce enough lift to raise the initial payload. A counterweight system was designed (Figure 2.5) to reduce the effective weight of the rig. This system allowed us to make the rig effectively as light as we wanted with the only unavoidable effective weight being the static friction in the pulleys (≈ grams). The system was able to allow us to operate each rotor within its designed thrust specifications.

The rotor system was controlled by a computer connected through both Arduino and National Instruments data acquisition system (NI-DAQ) (Table 2.1). Our system used 3 sensors and a motor controlled through an electronic speed control (ESC) seen in Figure 2.6. The torque sensor was fed through an external amplifier to increase the outputted voltage signal. After being amplified, the signal fed into our NI-DAQ system. The laser distance sensor and encoder voltage were directly sent to the Arduino Mega. The ESC received its commands from the Arduino Mega. On the computer, a LabVIEW Virtual Instrument controlled and spliced all data together (code layout in Figure 2.7).

A Proportional-Derivative-Integral (PID) control scheme was used to hover our rotor system above the ground at prescribed distances seen in Figure 2.7. After the appropriate rotor was mounted on the rotor shaft, the user inputted the distance the rotor should be from the ground. The PID then controlled the rotor by sending signals to ESC and motor. The controller sped up the rotor's rotation if it the height was below the user set distance and vice versa. Once the rotor was stable at its set distance, the user then initiated data collection. The data from all sensors was converted and saved into text files.

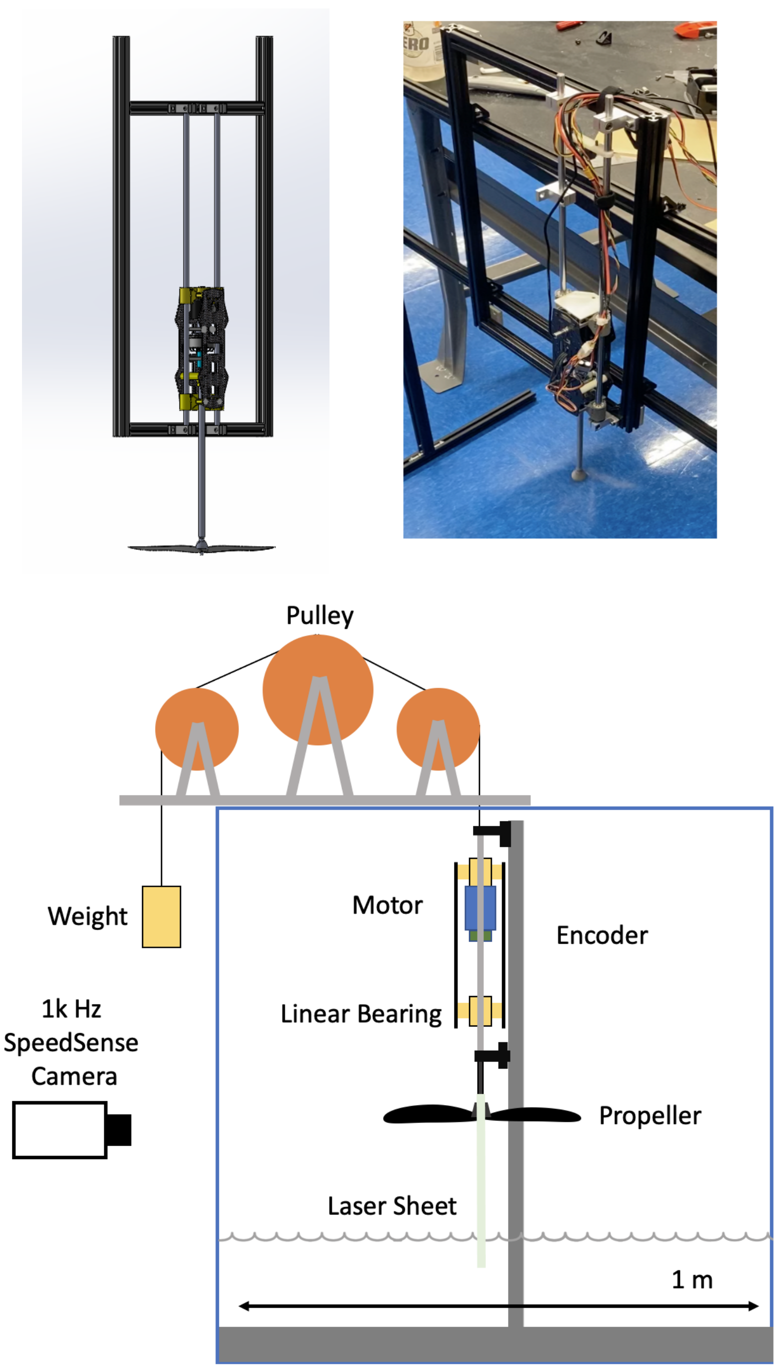

Figure 2.5: Version 2.0 CAD (top left) and prototype (top right) of the isolated rotor test rig. Bottom: Schematic of the experimental arena including PIV location, water boundary, rotor system, & counterweight.

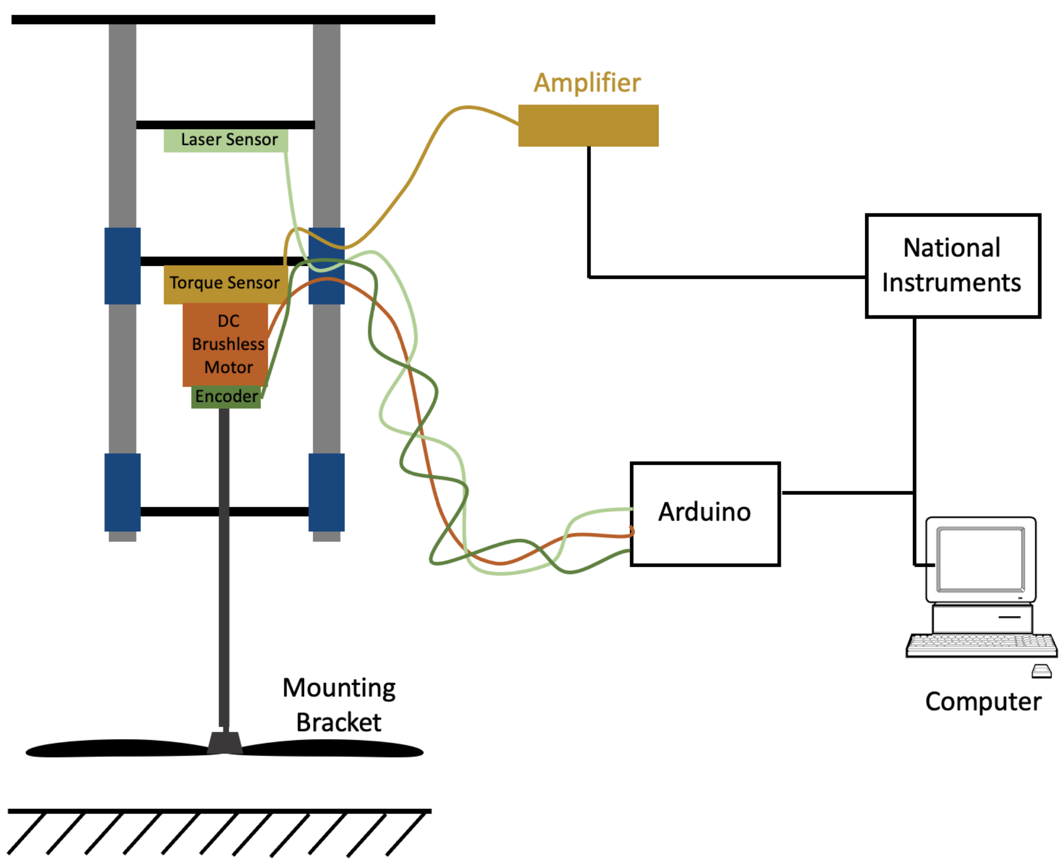

Figure 2.6: Control diagram showing connections used to operate rotor and collect data signals in the isolated rotor test rig.

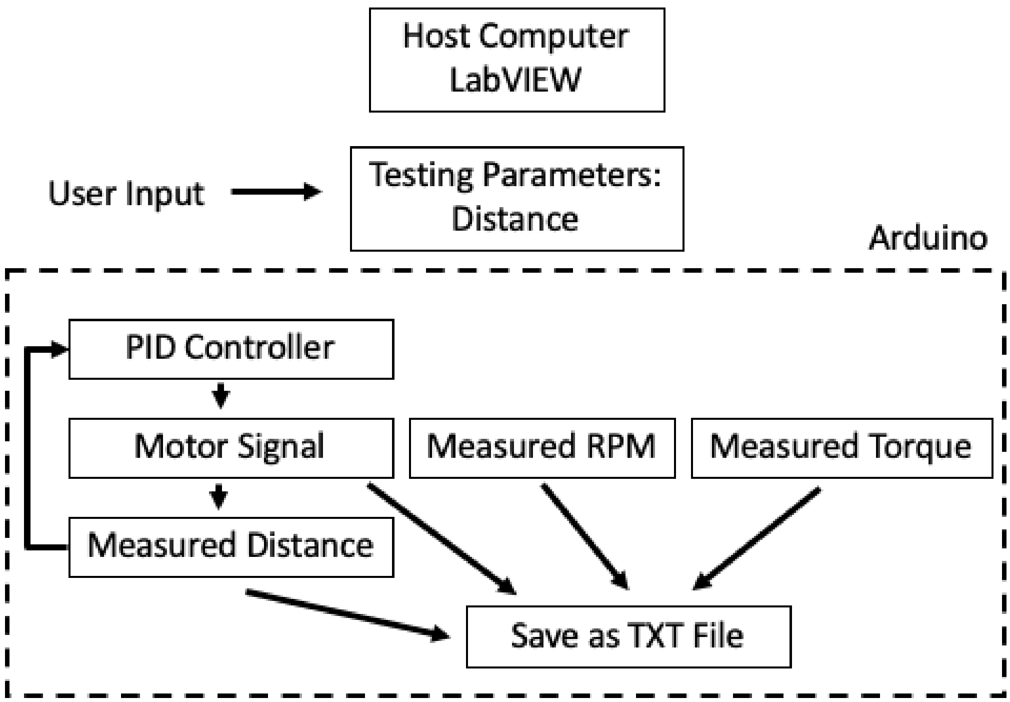

Figure 2.7: Architecture of the code and the testing sequence for the isolated rotor test rig.

2.3 Micro Aerial Vehicle Arena

Our first rig (Section 2.1) was designed to study single rotors in isolation. To study full MAVs in tethered and autonomous flights, I designed and built a second, larger arena. To conduct PIV, this arena needed to be an enclosed space to contain the seeding particles. This arena needed to be able to use a motion capture system to track the movement of untethered MAVs. This arena also needed to allow for precise positioning of a MAV platform near different solid boundaries. Figure 2.8 shows the arena that was designed and built according to the afforementioned design constraints.

Table 2.2: MAV Arena Equipment Parameters

MAV	Crazyflie 2.0
Motion Capture	Optitrack [Motive 2.0]
Load Cell	LCFD [1 kg Range]
Structure	80/20 T-Slotted Aluminum
Power Supply	3.7 V [20 Amp]
Fan	Sky Genius AM-F130
Microcontroller	Arduino MEGA
Data Aquistion	National Instruments USB-6009

The closed arena had to be precisely constructed to allow us to get the most accurate PIV flow images that our system allowed. With that in mind, the first step was determining the size, in which our main concern was wall interference with the flow. To avoid any unintentional influence from the walls, I made the cube 1.5 meters in length. This would ensure that our MAVs (which are ≈ 0.1 meter in total length) would have negligible wall interference in the flow when centered in the arena. Our arena used glass and black high-density polyethylene walls and were secured together by a black-anodized T-slotted aluminum frame. The glass was to allow entrance of laser light and give optical access to our high-speed cameras. Matte black was chosen where possible to lessen reflections of the laser and increase contrast in our PIV images. To allow for flight of our MAV platforms, we installed an infrared camera tracking system (Optitrack Prime 13) (see Table 2.2). Our system uses 6 cameras to track one or multiple MAVs using 3D localization. The Optitrack system was connected to our software tracker Motive. Through Motive, we had the ability to calibrate our camera tracking system and send live position information to different flight controllers.

Many components seen in Figure 2.8 were linked within this arena that allowed for untethered & tethered MAV flight and PIV. On the top of the arena were 6 Optitrack cameras that would allow for 3D infrared position tracking within the volume of our arena. The dual cavity laser was placed to the side of the arena, pointing through the glass and ending on the black back wall reducing reflections. The high-speed camera is outside of the plane of the schematic but was aimed perpendicular to the glass, and the dashed lines indicate its field of view. A stepper motor and linear actuator system was used to traverse the MAV along an axis perpendicular to the false ground/ceiling platform.

Communication for testing inside the arena was a combination of wired and wireless signals (Figure 2.9). The MAV was controlled through Robotic Operating System or ROS. The data was sent wirelessly using the specific Crazyflie radio antenna. During untethered tests, the Crazyflie was powered using its supplied battery pack. However, for tethered tests, the Crazyflie was connected to an external power supply to allow for longer testing periods. The linear actuator was controlled by a servo motor which was sent signals via Arduino. The lone sensor in this setup was a load cell whose signal was amplified and then sent to the Arduino.

An iterative control scheme was developed to allow for large trial sets of our MAV near-boundary data set in Figure 2.10. Our system goes to each distance from the boundary and measures lift at each of the prescribed throttle values. Because our testing sequence took hours, we were sure to account for sensor drift. We adjusted our data capture in two ways account for this potential drift. First, once a list of near-boundary distances were selected, we used the Latin square method to make sure we had a list of the distances where every order of distances was in the list. Secondly, before each set of throttles was run, the load cell was zeroed with a throttle of 0% while the motor was off.

The testing sequence was as follows. First, the LabVIEW code read in the user-submitted list of distances and throttle values (Figure 2.10). The load cell would then move to the distance (i), then the load cell would zero. After these steups, ROS would send the throttle (g) to the Crazyflie. If the command was received successfully, the Labview Virtual Instrument would collect 30 seconds of lift force data from the load cell.

To test the motion-tracking capability of the flight arena, I partnered with fellow graduate student Bruce Zhang to conduct a series of untethered Crazyflie test flights. In these tests, the Crazyflie was commanded to fly in a figure-eight pattern, with the center of the trajectory passing through a downward jet produced by a second Crazyflie tethered above in Figure 2.11. Our systems allowed for two Crazyflies to be operated by one radio. The throttle data was captured by the Crazyflie platform and the altitude data from the motion capture system.

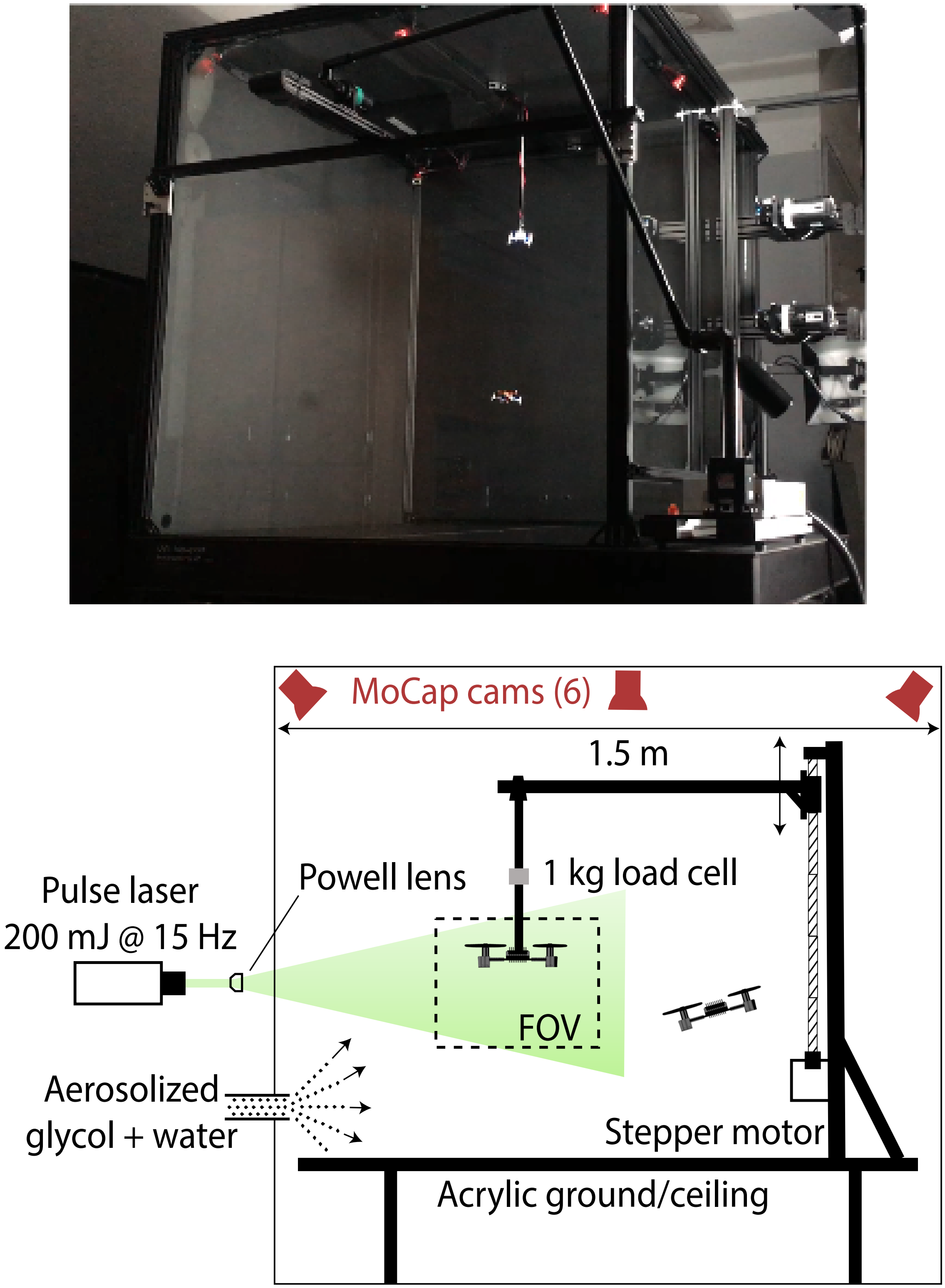

Figure 2.8: Top: Picture of the untethered MAV arena. Bottom: Schematic of arena including PIV system, near-boundary controller, motion capture system, and MAVs.

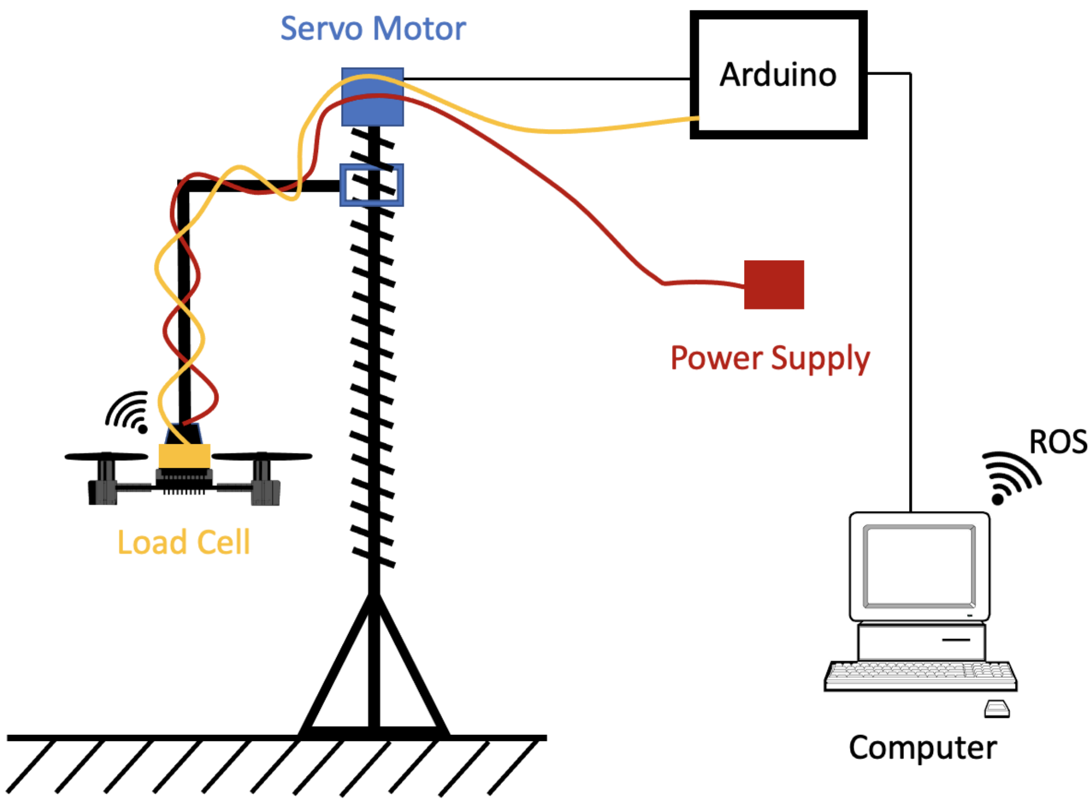

Figure 2.9: MAV flight arena: control scheme utilizing our host computer to control the linear actuation as well as data collection and the Crazyflie commands.

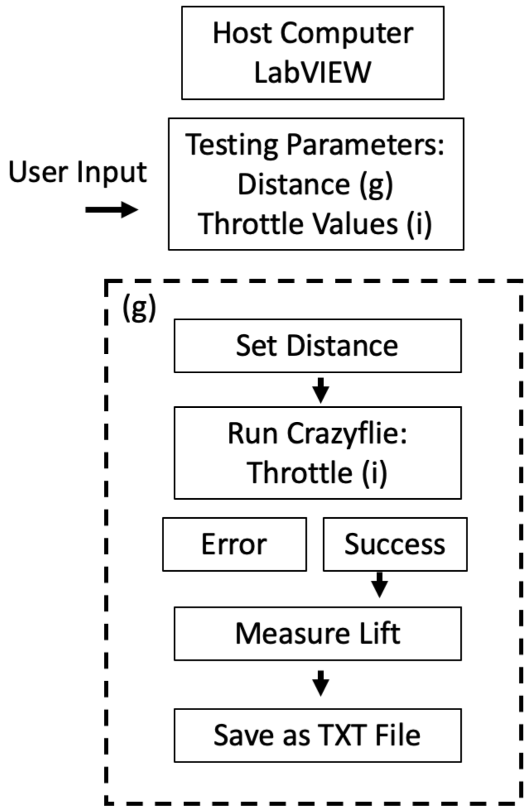

Figure 2.10: Architecture of the code and the testing sequence for the tethered MAV near-boundary arena.

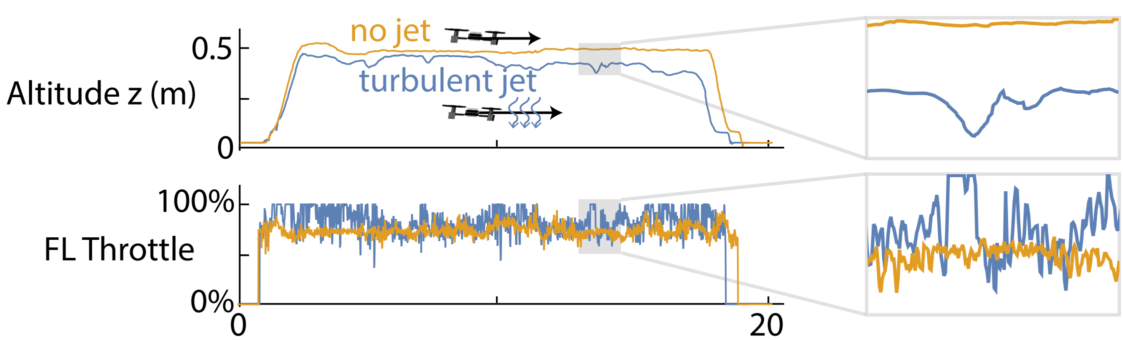

Figure 2.11: Flight altitude of two MAVs (one unperturbed and other crosses under wake of a tethered MAV) in the MAV flight arena. As the MAV crosses under the wake of the tethered MAV, its flight path was altered.

2.4 Summary

This Chapter described the construction of two arenas: one for isolated rotors and one for untethered MAVs. The isolated rotor rig was designed to test in multiple mediums of fluids dynamically. The MAV arena was designed to support tethered and untethered MAV platforms such as the Crazyflie 2.0. Both arenas are designed to allow Particle Image Velocimetry. The two arenas were used in the remaining Chapters as follows. For Chapter 3 and 6: the isolated rotor system was used to measure aerodynamic performance of different rotors. For Chapter 4 and 5: The MAV arena was used to investigate near boundary MAV flight and applications of near boundary flight.

Chapter 3

Ground Effect Modeling and Rotor Design Dependency

Ground effect is vital for future opportunities for UAVs in Urban Air Mobility. We first explored ground effect for isolated rotor systems. By focusing on a single rotor system, we could isolate the fundamental physics before extrapolating to more complex multirotor configurations. First, we developed a model that describes a rotor in ground effect. To test the validity of the model, we measured a rotor as it hovered in various ground conditions. We compared rotors of different diameters and pitches to see their effect on performance near the ground. Lastly, we conducted Particle Image Velocimetry (PIV) on these rotors for more fluid flow insights.

3.1 Experiment Setup and Methods

Ground effect generates more lift for a rotor then when in open air. Our goal from our system was to show that lift efficiency is increased as a rotor nears a ground plane. The isolated rotor system from Chapter 3.1 was used for this chapter. Since the rotor system is dynamic, a traditional compression load sensor was not an option. To measure the performance of rotor, we therefore utilized angular velocity. A CUI AMT-103 encoder was

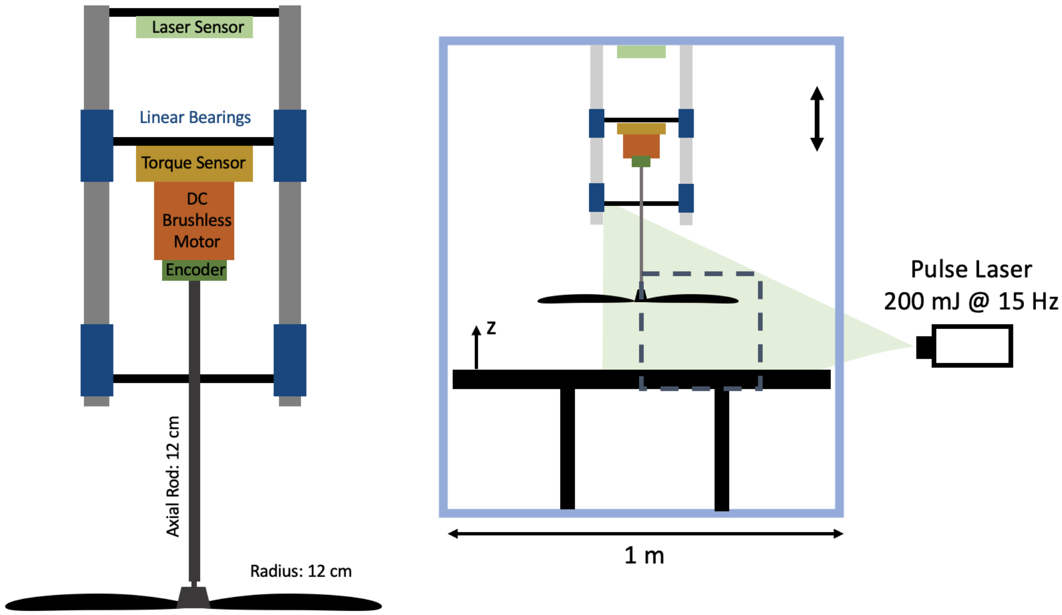

Figure 3.1: Left: Equipment used to measure performance of a isolated rotor. Right: Schematic of rotor above solid boundary with location of laser sheet and camera Field of View.

used to measure the angular velocity of the hovering rotor. A simple PID controller seen in Figure **??** was used for the hovering rotor to match the desired height above the ground. A laser distance sensor was used to measure the height of the rotor above the ground plane.

Rotor scale and twist were decided based on commercially available rotor blades. We used 3 DJI drones seen in Figure 3.2 to compare their diameters and blade pitches. The three drones have three distinct mission types. The larger rotors and blade pitches are meant for high altitude sensing, whereas the smaller rotors and blade pitches are meant for indoor flights in cluttered environments. We created a rotor parameter sweep with diameters 18 cm to 28 cm and blade pitches of 3, 5, & 7 inches. The blade pitches match a majority of the cases within which commercially-available UAV drones operate. The main objective of the different rotor diameters is to understand the effect that rotor size has on the rotor's near-ground performance. The different sized rotors would allow for our testing rig to operate in different Reynolds number regimes. Typically, models of rotors in ground effect are done in high-Reynolds number regimes which assume inviscid flow. As rotors get smaller in

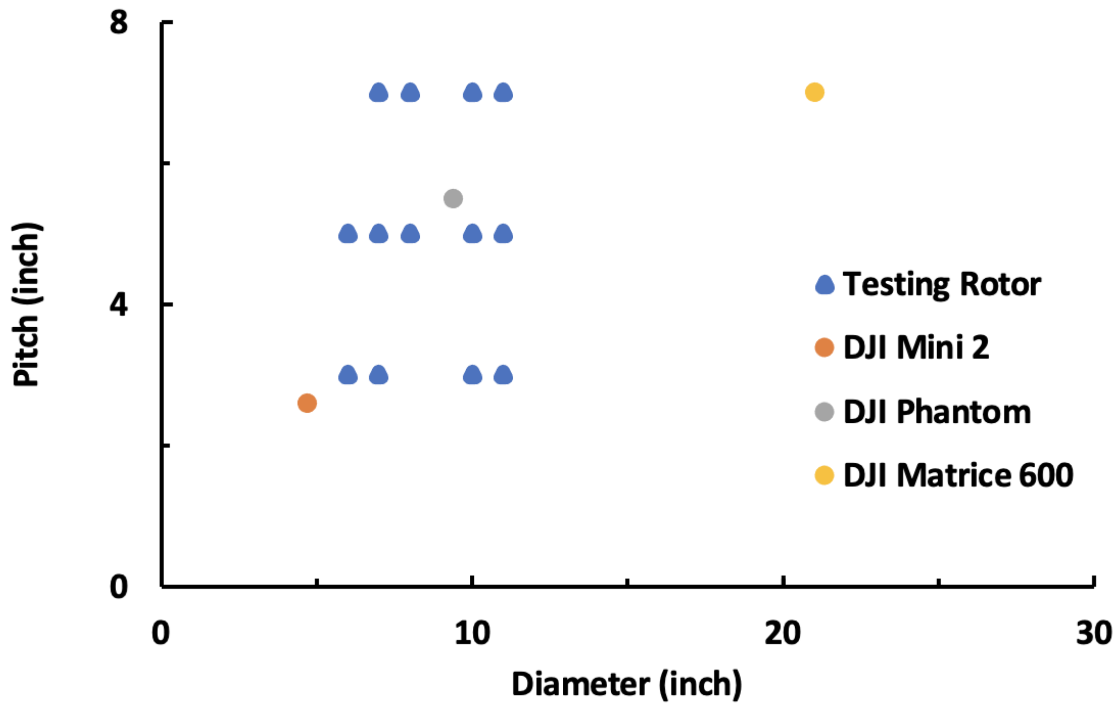

Figure 3.2: Comparison of blade pitch and diameter of our test rotors to commercially popular UAV platforms.

diameter, we are interested in how the viscous forces can affect our previous understanding of ground effect.

Boundaries within our testing arena play an important role in our experiment. The main boundary we are interested in studying and manipulating is the ground plane. For our ground plane, we used a black High Density Poly Ethylene (HDPE) smooth surface. For our experiment, we were not interested in varying or studying the roughness of the surface. Within the testing cube itself (Figure 3.2), which measures 1 m in all directions, the rotor was placed directly in the middle of the cube so the closest distance between the largest rotor tip and side wall was ~ 36 cm. The walls of the cube presumably cause boundary affects on the flow around the rotor and secondary flows in the cube. However, based on work from Chapter 4, we estimate that this interference was negligible on the lift force.

A primary function of this testing sequence was for the ability of our rotor to simulate

Table 3.1: Experiment Parameters

Length of Data Capture	120 seconds
PID Gains	K_p = 5, K_i = 1, & K_d = 0.01
Rotor Frequency	4000 to 6800 RPM
Reynolds Number	250,000 to 815,000

flight by being able to hover. To understand the change in lift or thrust, we needed the frequency of the rotor at a given height above the ground plane. The Arduino recorded the distance data and averaged it at 1k Hz to determine its height. The PID controller then adjusted the signal to the ESC which then controlled the motor.

An important feature of our set up was the ability to measure the flow fields of the rotor. Since our PIV system was limited to time-averaged flow fields, we could not have a rotor that moved in the vertical direction during imaging. Therefore, after the data were collected from our PID hovering tests, we selected the ground distances, rotors, and frequencies at which to measure flow conditions. For our PIV, we matched the dimensionless distances to the ground $\hat{Z}$ for all the rotors. Rotor frequencies measured during our hovering experiments were used for PIV. This method in turn gave us a spread of Reynolds number flows for each case and also made the induced velocities different for each condition tested.

PIV was captured using a time-averaged dual cavity pulse laser system. Particle motion was triangulated by a high-speed camera (Phantom SpeedSense M341, 4MP) that fed into cross-correlation software (Dantec Dynamic Studio). Based on a convergence test (Figure 2.3), we determined that 100 image pairs (7 s of data) were sufficient for time-averaged velocity fields to converge to < 0.1% of the average projection error per 10 μm. The result of the averaged cross-correlations was a grid of velocity vectors, one for each 32 x 32 px window. We used the velocity grids to plot airspeed density and trace streamlines (DensityPlot $\&$ StreamPlot in Mathematica 10). Since the field of view was limited, only half of the rotor was initially imaged and was then reflected across the rotor axis. Areas that were blocked due to poor contrast near the illuminated rotor blade are shown as blacked areas in the figures. Downwash velocities were estimated by using a cross-section of the velocity field of the wake beneath each rotor.

The testing in this experiment was done in two parts: (1) rotors were hovered at specific $\hat{Z}$ values above the ground and frequencies were measured, and (2) PIV images were taken of the near-ground rotors. The first step was determining the $\hat{Z}$ distances from the ground which were limited by the constraints of the system. We could not go above $\hat{Z} = 2$ due to the size of the cube, and we could not go below $\hat{Z} = 0.5$ without having the rotor strike the ground plane. With this in mind, we measured data at $\hat{Z}$: [.5, .65, 1, 1.5, 2]. To average out the small oscillations from our PID control and the associated friction on the bearings, we captured dated for 120 seconds. From these results, we conducted PIV on 6 different rotors (2 diameters [25 & 28 cm] with 3 pitches [3, 5, & 7 inches]).

3.2 Modeling

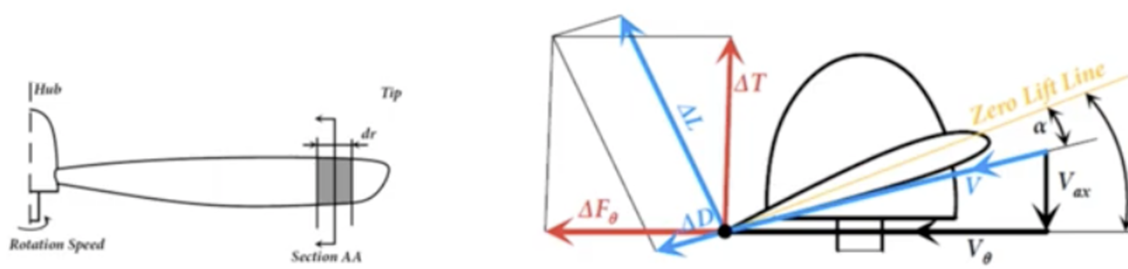

Figure 3.3: Aerodynamic forces on a rotor element in Blade Element Theory. [44]

Blade Element Theory was used to model the performance of propellers. The basis of this theory is slicing the propeller into finite width dr airfoils seen in Figure 3.3. Now imagine this 3D slice is small enough to be considered a 2D airfoil. This section of airfoil uses the standard aerodynamic equations for lift and drag (Eq. 3.1). Because every section of the blade is treated separately, we can use the specific angle of attack of each section. In this analysis, we are interested primarily in the scaling of the lift and drag values, so we are only using the proportions and neglecting the lift and drag coefficients (C_l & C_d).

$$dD \& \, dL \propto \frac{\rho V^2}{2} c \, dr \qquad \text{(Eq. 3.1)}$$

$$\psi = \theta - \alpha, V_\theta = 2\pi r f \qquad \text{(Eq. 3.2)}$$

One of the main differences between 2D airfoil theory and 3D Blade Element Theory is the direction of the desired resultant force. In traditional airfoil theory, the direction of drag is parallel to airflow, and the lift is perpendicular to the drag. However, this lift/drag orientation is not usually true for a propeller section. The plane of rotation V_θ is always constant and is perpendicular to the thrust T. To increase efficiency, modern propellers have a twist angle which alters the blade angle θ at each section. The blade angle θ refers to the angle between the zero lift line and the plane of rotation V_θ. The ψ angle represents the angle of airflow relative to the plane of rotation V_θ. This angle relates the lift and drag components to the thrust and torque component of force on a propeller. This angle also represents the incoming flow speed felt by the airfoil element. The flow based on rotation is V_θ and is calculated based on the angular velocity of the entire propeller equation 3.2.

$$dT \propto \; dL \cos \psi - \; dD \sin \psi \qquad \text{(Eq. 3.3)}$$

$$T \propto \int_0^r dT \, dr \qquad \text{(Eq. 3.4)}$$

Thrust for a propeller is calculated by adding up the components of lift and drag on the 2D airfoil section. Using the angle ψ, the lift and drag from the 2D airfoil can be resolved into its thrust and torque components (Eq. 3.3). Equation 3.3 shows how the lift and drag are proportional to the thrust. As mentioned, we are neglecting other effects such as airfoil shape at this point. Now that we calculated thrust for one 2D airfoil component, the thrusts can be summed up over the entire radius of the blade.

$$T = C_T \rho f^2 d^4 \qquad \text{(Eq. 3.5)}$$

The thrust for a propeller approximated by Blade Element Theory is then fitted based on experimental data. In equation 3.4, the thrust is only a proportional scaling because we neglected the lift and drag coefficients in airfoil theory. During lift and drag calculations, a coefficient is added that is experimentally determined and is a function of the airfoil shape, its Reynolds & Mach number. The thrust equation (Eq. 3.5) has its own experimentally-determined coefficient, C_T, which is a function of propeller shape, number of blades, and Reynolds number. With the coefficient of thrust already known for our propellers, we are easily able to determine the approximate thrust of our system.

$$\frac{L}{L_\infty} = \frac{1}{1 - \frac{1}{16\hat{Z}^2}}, \qquad \text{(Eq. 3.6)}$$

Ground effect on various rotor shapes can be determined by combining Blade Element Theory and a ground effect model. The model we chose was [13], the potential flow high-Reynolds number helicopter theory ground effect model widely used today. In the model, the rotor's image leads to downwash velocities at the rotor plane. The result is an increase in rotor lift compared to its value far from the ground (L_∞). Near-ground lift therefore depends on the altitude, Z, according to where $\hat{Z}$ is the altitude scaled by rotor radius ($\hat{Z} \equiv Z/r$). The method, which is based on potential flow theory, assumes that the flow is incompressible and inviscid. It also assumes that the downwash is constant across the rotor disk, that the rotor disk is infinitely thin, and that $\hat{Z} > 0.25$.

$$f(\hat{Z}) = \sqrt{\frac{Wg}{1 - \frac{1}{16\hat{Z}^2}} \frac{1}{C_T \rho d^4}} \qquad \text{(Eq. 3.7)}$$

$$\frac{f(\hat{Z})}{f(\hat{Z})_\infty} = \sqrt{\frac{1}{1 - \frac{1}{16\hat{Z}^2}}} \qquad \text{(Eq. 3.8)}$$

To compare to our system, we needed the model to incorporate ground effect and allow us to compare rotor frequency to the distance of a hovering rotor system to the ground. The C-B Model (Eq. 3.6) produces a dimensionless thrust scalar at each $\hat{Z}$ value. We inverted the thrust equation (Eq. 3.5) to isolate frequency f as the dependent variable and thrust T as the independent variable. The thrust was an independent variable, because we used the results from our experiments to influence the inputs to the model. The model is based on potential flow so it cannot be used to measure the Reynolds number effect. A correction factor that needs to be included should have a component that is relevant for Reynolds number effects.

All of our experiments were focused on hovering conditions, meaning that the thrust or lift of the rotor had to equal the weight force off the rotor system. The weight of the system was considered to be the near boundary lift L, and this was converted to our ground effect lift L_∞ by the C-B model. Using this scaled lift value, the frequency was then converted using Blade Element Theory and changes based on the blade's $\hat{Z}$ in equation 3.7. The coefficient of thrust for our rotors was experimentally-determined by the rotor manufacturer (APC Propellers).

3.3 Results

3.3.1 Experimental Results

The model follows intuition by increasing the hover frequency as the payload of a rotor increases. In Figure 3.4 the top row of the figure shows the model results as line plots and delimited into four plots showing the four tested rotor diameters. The colors reflect the diameter of the rotors, where the smallest rotor (d = 18 cm) is the lightest as yellow and

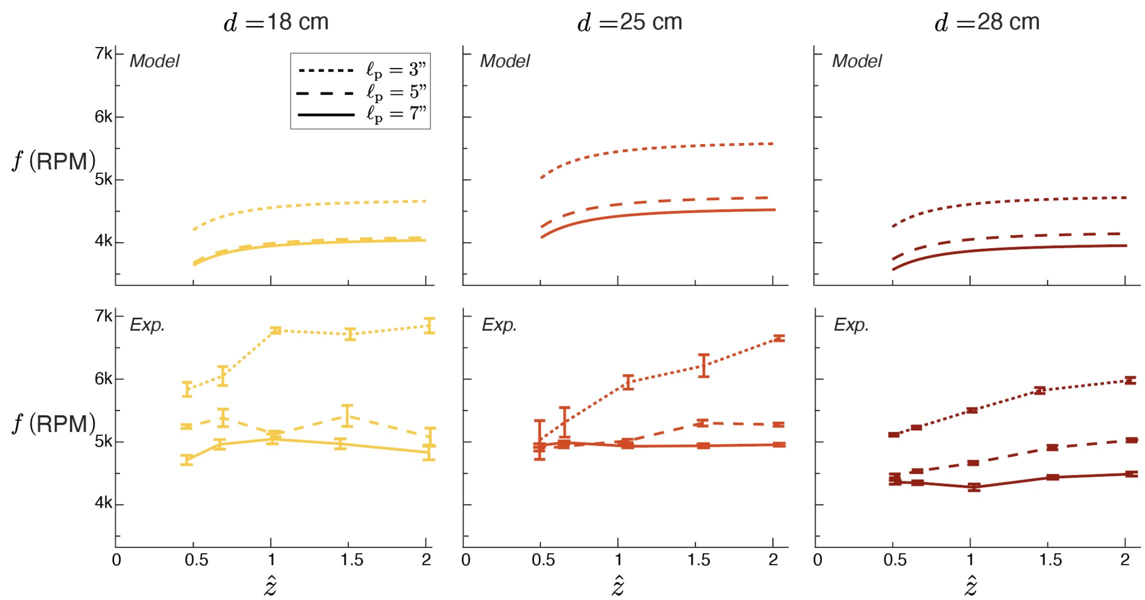

Figure 3.4: Top: BET combined with C-B Model shows the frequency needed to lift the experimental rig's weight. Bottom: Frequencies needed to hover at the near-boundary distances.

the largest rotor (d = 28 cm) is the darkest as maroon. The type of line from dashed to solid indicates the rotor's blade pitch. The model was created by using equation 3.7. The different pitches of the blades create three distinct levels of frequencies with similar paths to one another. The weight used for each model is based on the experimental weight which was consistent for each rotor diameter, e.g. for d = 28 cm the rotor system weight was 0.425 kg. All three rotor diameters show that the frequency decreases as the $\hat{Z}$ decreases. The frequency range for each rotor is similar for each test because we used counterweights in a way to match the rotor's rated payload capacity. For all the rotor diameters, we see that as pitch decreases, the frequency decreases as well.

The experimental data show what frequencies are necessary to maintain hovering of our rotor system. In Figure 3.4 (bottom row), we measured the required frequency's average and standard deviation at each of our prescribed $\hat{Z}$'s. The colors and line styles match the same pattern seen above for the rotors. Most of the lines show a decrease in frequency needed for the rotors as the $\hat{Z}$ decreases. The larger negative slopes are coming from the rotors when their pitch is 3 inches and tend to decrease as the pitch increases. The standard deviations of the frequencies are small enough to indicate that friction effects are low and that oscillations of our rotor system were minimal. Although the rotor system weight was chosen to reflect each rotor's payload recommendations, there is a slight drop in the overall frequency required as the rotor diameter increases.

Scaling the model and experimental results by the largest $\hat{Z}$ gives perspective about the effect that the ground has on frequency. Instinctively as the lift increases near the ground, less frequency is needed to lift the same payload, and the scaling shows this effect. The model creates one line plot for all the rotor types. This collapse is due to the fact that scaling by the largest $\hat{Z}$ eliminates all the rotor coefficients, and the only factor of the model ends up being the C-B Model or the effect of the ground. For our experimental results, we see a similar trend across all rotors: lower frequencies are required to hover as $\hat{Z}$ decreases. The level of slope increases as blade pitch becomes smaller.

3.3.2 Differences between Model and Results

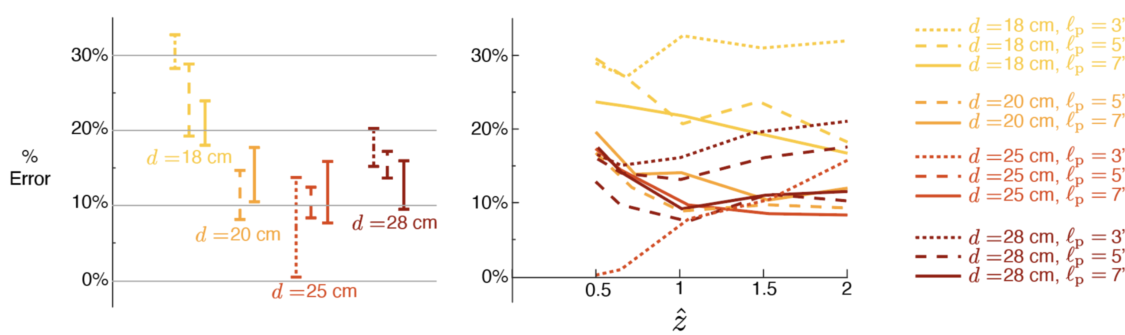

Figure 3.5: Absolute error between experimental data and model results. Left: Average error at all the distances for each rotor type. Right: Error versus distance to the ground.

The percent error we calculated between experiments and model shows no major trends in regards to the $\hat{Z}$ value. As $\hat{Z}$ decreases, there was a small increase in error as $\hat{Z} < 1$. For the error $\hat{Z} > 1$, we see a very steady error for most cases except the case of d = 18 cm and pitch = 5 inches. For the case of d = 25 cm and pitch = 3 inches, we see a decreasing error as $\hat{Z}$ approaches 0.5. The error in this case approaches zero, which implies good alignment between the model and experimental data. For the cases in which d = 18 cm, we do not see the trends as clearly as in the other diameters, and the error for these rotors is much higher. There does not seem to be a difference based on the pitch values of blades of the same diameter.

When averaging the percent error across all $\hat{Z}$s, multiple patterns and trends appear. The d = 18 cm cases all have substantially higher errors with means above 20%. The highest error was fora pitch of 3 inches at around 30%, where pitches of 5 inches and then 7 inches followed. For d = 20, 25, and 28 cm, the errors were concentrated in the 10-20% range and were similar to each other. In the case of d = 25 cm and pitch = 3 inches, we see a high variation that brings the error from ~ 15% to 0%, causing this case to have the lowest error range. The cases do not all follow the same order in error for the pitches, but the median average percent error for each diameter is the case where pitch = 5 inches. This indicates that the pitch has an effect on the model's accuracy but that it varies with rotor diameter.

3.3.3 PIV Results

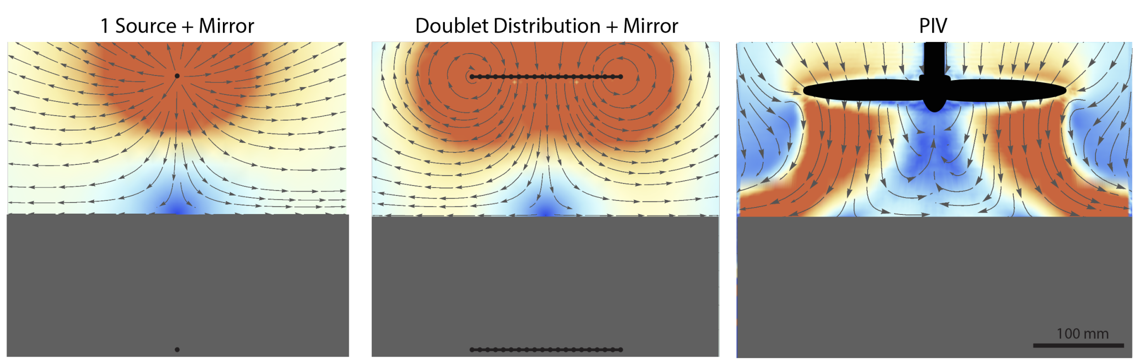

Figure 3.6: Potential flow model of one source and mirror simulation ground as well as doublet distribution and mirror. Right: Time-averaged PIV flow field from our data set (Rotor D: 0.28 m, Pitch: 7 in, & $\hat{Z}$: 1)

The ground effect model by Cheeseman & Bennett [43] was designed using a simple source potential flow model. In figure 3.6, we compared two potential flow models to an example from our PIV data set to explore similarities and differences. On the left, we used a single source that was mirrored to create a ground plane. In this flow field, there is no flux across the ground plane, and there is slip along the surface. To expand upon the idea of a single source flow, we created a mirrored doublet distribution, which more closely resembles the flow field around a rotor. Unlike the source, the doublet has inflow and has a finite diameter, which is similar to rotors. Being that these models are potential flow, the operating environment is inviscid. For both models, we have a stagnation zone in the middle on the ground plane where the vertical flow slows to zero speed because of the no flux condition. In our sample PIV case, we see all the expected flow features on the rotor, such as inflow to the rotor plane and a high velocity wake beneath. The one similarity we see between both cases is the presence of a stagnation zone beneath the rotors. One major difference in both cases is the appearance of two strong momentum jets that are curved to the sides. The flow for the two potential flow models follow the same general pattern but are drastically slowed down by the presence of the ground plane.

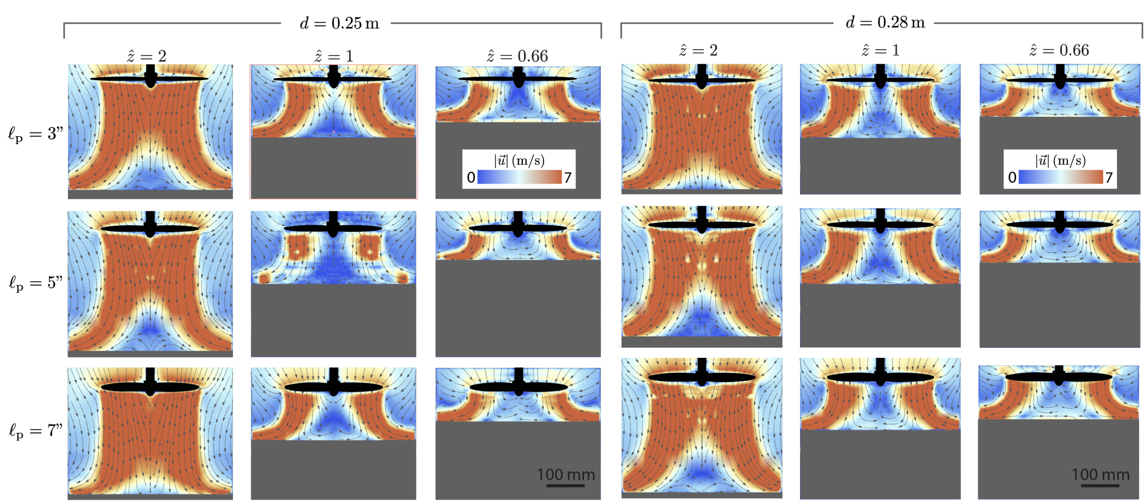

Figure 3.7: Time-Averaged PIV flow fields for rotor diameters 25 cm & 28 cm at all 3 pitches.

The flow fields of the rotor shapes depend on the $\hat{Z}$ value and but are less dependent on rotor size and pitch. We considered PIV for the two largest diameter cases in Figure

3.7. The shapes of the steady state wake conditions were consistent across the three $\hat{Z}$ values: 2, 1, and 0.66. For the furthest from the ground case of $\hat{Z}$ = 2, the rotor created a defined full wake from the rotor all the way to the ground with a small stagnation zone in the middle (~ 2 cm from the ground plane). However, in the two other $\hat{Z}$ cases, we see the stagnation zone reach all the way to the rotor plane and split the wake into two jets. In the closest case, the stagnation zone went above the rotor plane, reducing the loading on the rotor blade. For some of the $\hat{Z}$ = 1 cases, the stagnation zone reached all the way to the rotor blade and even slightly above the rotor plane. The differences between the pitch values are negligible in comparison. The one minor difference between different pitches was the height of the stagnation zone in the $\hat{Z}$ = 2 case.

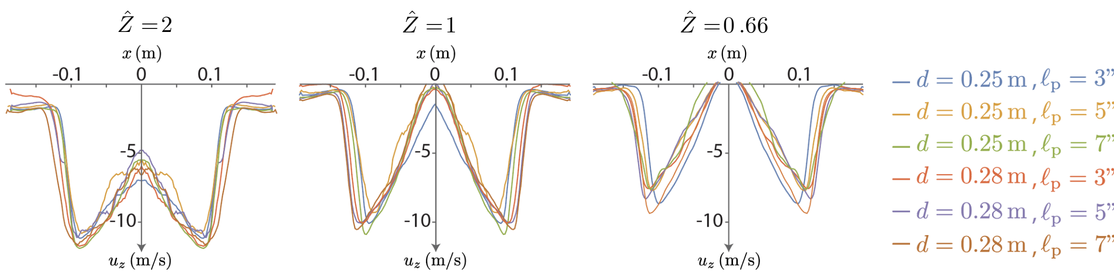

Figure 3.8: Velocity cross section at 1/6 radius below rotor midplane at $\hat{Z}$: 2,1,0.66.

The cross sections of velocity show that the direction and intensity of the flow depends on distance from ground. In Figure 3.8, we see the velocity cross section 1/6 of a rotor diameter under the rotor plane. As seen in Figure 3.7, the trends across the pitches and diameters are very similar to each other. In each $\hat{Z}$ case, we see large velocities under the rotor reaching ~ 10 m/s. Closer to the central axis underneath rotor, these velocities dip for all cases to around 5 m/s. In the two other $\hat{Z}$ cases, the peak velocity gets slower, and the area in which it decreases turns into a more triangle region. For the cases where $\hat{Z}$ is 1, the velocity decreases to 0 whereas in the cases where $\hat{Z}$ is 0.66, the velocity becomes positive. This positive velocity is known as the fountain effect in which the air in the wake changes direction due to the stagnation zone. For all velocity fields, there is a sharp increase from the surrounding air velocity to the high velocity on the edge of the wake.

3.4 Discussion

Our model equation (Eq. 3.7) shows the trend that the rotor frequency needed for a prescribed payload changes as the distance from ground changes. By employing the ground effect to blade element theory, we were able to see the exponential change in the frequency as the ground is approached. The coefficient of thrust increases as the rotor blades pitch increases. This increase in thrust is due to the higher angular velocity which causes higher thrust for rotors with higher blade pitches. This model and theory do not account for the added drag and torque caused by the higher blade pitch. The model uncovered the direct relationship between frequency to the square root of weight and coefficient of thrust. The model also showed the direct relationship to the diameter squared. The diameter has a power to the four stronger relationship to the frequency compared to the payload and the coefficient of thrust. This has huge importance when it comes to UAVs, especially MAVs whose sizes are much smaller in diameter than traditional vehicles like helicopters. By applying the C-B model equation 3.6, we see the instinctual decrease in frequency as the $\hat{Z}$ value decreases. The influence of the ground has a direct square root dependence on the change in frequency. The model provides a quick and simple way to estimate the influence of the ground effect on the frequency of a prescribed rotor and payload system.

The pitches dictated the effectiveness of the ground effect within our experiments. An instinctual decrease in frequency as seen as the $\hat{Z}$ value decreasd and the influence of the ground on the flow increased. In Figure 3.4, we see that rotors with higher blade pitches require higher frequencies to hover, and the ground effect is less prominent on those rotors. The influence of the ground is less noticeably for rotors with lower pitches. Most UAVs, especially smaller ones, have lower-pitched blades. The influence of the ground begins earlier for these vehicles compared to larger higher-pitched rotor vehicles. Our results show that the slopes of the higher-pitched blades are more horizontal as the pitch of the blade increases. In comparison to the model, the increase in pitch does lead to higher frequencies for the same payload, and our experiment validates this effect. However, the model only determines the influence of the ground based on $\hat{Z}$ and not rotor type. The model falls short in determining the influence of ground effect based on the rotor type. The model also predicts a strong drop off in frequency at $\hat{Z} < 1$ which our experimental data doesn't support.

Percent error is not dependent on the influence of the ground effect. The percent error was consistent for most cases when $\hat{Z} > 1$. The outlier case was d = 18 cm, which had both the highest error as well as the highest frequency in our experiments. The model predicted much lower frequency requirements for this rotor diameter and payload. The smaller diameter rotor case is perhaps most important due to the widespread use of small rotors in modern MAVs. MAVs tend to deviate from the traditional ground effect models like the C-B model equation 3.6. For smaller sized rotors the viscous effects tend to be more important as Reynolds number decreases. The d = 18 cm rotor has the lowest RPM/thrust ratio especially as the pitch decreases. The higher the RPM/thrust ratio, the more accurate the model is with our experiment.

Average percent error was consistent for the d = 20, 25, and 28 cm cases, and much higher for d = 18 cm case. The consistent 10-20% error can be attributed to an offset of the model and/or of the experimental setup. The coefficient of thrust, which was determined by the manufacturer, could be a source of the error, as well as the weight determined during our experiment. The percent error tended to increase as $\hat{Z}$ decreased, indicating that the ground effect model is over-predicting the influence in our experiments. The error in each rotor blade is influenced by the blade's pitch. This difference is not seen as $\hat{Z}$ changes, meaning it is all in the coefficient of thrust. Error seems to be averaged by the blades with pitch = 5 inches, and the blades with pitches of 3 and 7 inches are either larger or smaller than this.

The potential models fell short in comparing to the sample PIV images of ground effect. The models show a stronger influence of the ground than the actual flow field. The momentum jets go much closer to the surface than the models predict. Both the models and the actual flow show an indication of a stagnation zone. However, in the flow models, which include source objects, the stagnation zone can never reach the rotor plane. In the actual image, the stagnation zone increases all the way to the rotor plane and even goes beyond it. Unlike the models, it seems that viscosity plays a role and can explain the increase in the size of the stagnation zone. The effectiveness of inviscid models for predicting near-boundary flows will decrease as rotor sizes decrease and the Reynolds numbers increase.

In the flow images ,there is good agreement between the rotor diameters and the pitches of these rotors. The mean flow field and wake structure matches what is seen in other ground effect studies. The pitch seems to have negligible effect on the structure of the wake. However, the intensity and velocity tends to change to some degree. The stagnation zone grows in height and width as the rotor gets closer to the ground. The current models do not account for the decrease in rotor loading as the stagnation zone grows and even goes past the rotor plane. At its closest point, the stagnation zone even includes upward flow. This upward flow is seen in UAV vehicles and is thought to increase pressure and therefore lift on the vehicle increasing the apparent ground effect. The momentum jets change shape as the rotor approaches the ground. As the stagnation zone increases, the jets spread further from the center of the rotor. The angle of the jet increases as the rotor approaches the ground.

In the velocity cross section, there is indication of a fountain effect. The smallest $\hat{Z}$ case of 0.66 shows flow going upward. As the rotor approaches the ground plane, the velocity at the center of the rotor gets slower until it reverses direction and circulates upward. This is caused by the growing stagnation zone from the ground. As flow enters this stagnation zon,e it interacts with the wake on the opposite side, and the air can only go one direction, which causes recirculating flow. The highest velocity in our cross section is at around

2/3 R, which matches propeller theory and is also a factor of the design of the rotors and their twist. The profile due to this peak shows that its sharpness is increased as the rotor approaches the ground plane. The jets and this peak become thinner and more triangular. Using the jet's peak as a guide for air direction, the angle of the flow becomes large as it approaches the ground plane.

With the experimental rig that we used, there are a few limitations that are of note. The first was the unpredictable nature of the friction on the rails as the rotor was hovering. The vibration from the rotor as it spun could have increased the friction for some rotors compared to others. The torque sensor could not give information, and we believe this was due to the high vibrations that were in our system. All of our PIV images are time-averaged due to the refresh rate of our laser, but we are confident that we were able to capture the steady state wake fields. Within our PIV images, there were some light streaks caused by defects in the glass walls. We interpolated over these streaks in our final PIV output, but further modifications could be done to remove the streaks entirely. PIV was also not conducted on smaller diameter rotors in our work.

3.5 Conclusion

Our simple model predicts that the required frequency of isolated rotors can decrease as they approach the ground. From the model, we unlocked the relationship between rotor frequency, hover weight/ thrust, coefficient of thrust, and rotor radius. The error between our model and the experiment was consistent and indicates that a simple correction factor can be used to create a predictive model. The rotor's blade pitch had minimal effect on the accuracy of our models. However, in our experiments a lower RPM/thrust ratio tended to increase the influence and prominence of the ground effect. Flow images confirm the presence of a stagnation zone under each rotor that grows as the ground distance decreases. In some cases, the stagnation zone grows all the way past the rotor plane and even includes upward flow (fountain effect). The wake momentum jets sharpen to a triangle shape and decrease in amplitude as rotors near the ground. The jets change direction as well and point outward as the ground distance decreases.

Chapter 4

Influence of the Ground, Ceiling, and Side Wall on Micro Quadrotors

4.1 Introduction

To contribute to the growing field of near-boundary quadrotor research, we investigated the forces on a micro quadrotor (Crazyflie 2.0) near the ground, ceiling, and sidewall. Like groups that considered larger quadrotors [16, 14], we found power law dependencies between lift and ground proximity. In some regimes, however, existing models underpredicted the ground's effect and overpredicted the ceiling's effect. We therefore used Particle Image Velocimetry (PIV) to explore the time-averaged flowfields surrounding the micro quadrotors. We found that standing vortices beneath the quadrotor were highly sensitive to quadrotor attitude, and we did not observe the "fountain effect" seen beneath larger quadrotors [16]. These effects may account for some of the differences experienced by micro quadrotors.

4.2 Experimental Methods

The experiments described in Chapter 4 used the larger MAV arena (Section 2.3). For our first round of tests, we mounted a micro quadrotor (Crazyflie 2.0, rotor radius $r = 23$ mm) to a 1-kg load cell (Omega LCFD, $\pm$ 1.5 g accuracy) in the center of the arena. The load cell was suspended from a custom traverse that positioned the quadrotor near a horizontal plane or a sidewall. We chose the Crazyflie because of its open-source support and its popularity in the hobbyist community, and we chose a tethered arrangement so we could measure time-averaged flow fields and collect force data simultaneously. Boundary proximity Z is the distance between the rotor midline and the ground/ceiling/sidewall (in the sidewall cases, proximity is measured from the rotor nearest to the wall). Ceiling tests were done by inverting the quadrotor and using the same horizontal plane. We checked that orientation had negligible effects by comparing flow fields between upright and upside-down cases (along typical streamlines in our setup, dynamic pressures are about 50 times higher than gravitational pressures).

At 20 different distances from the ground/ceiling/sidewall Table 4.1, we recorded time-averaged lift for 4 throttle levels: 25%, 50%, 75%, and 92% (max reliable throttle). For reference, Crazyflies with no payload hover at 60% throttle. The traverse automatically visited each distance 15 times in a randomized order, averaging 10 s of lift at 1000 Hz for each trial. The force sensor was re-zeroed between each trial to minimize sensor drift between trials, and no observable drift took place within each trial. To facilitate comparisons between cases, we calculated the percent increase of net lift compared to its value far from boundaries: $\Delta L \equiv (L - L_\infty)/L_\infty$.

To visualize the flow around the Crazyflie, we used the PIV system described in Section 2.1. As a reminder, the system used a sheet of illuminated aerosolized glycol droplets visualized by two high-speed cameras. For these experiments, the laser sheet cut through the midline of the Crazyflie and included regions both above and below the rotors (Fig.

Table 4.1: Distances from the boundary during tethered experiments

Distance to Ceiling (cm)	Distance to Ground (cm)	Distance to Sidewall (cm)
5	57	15
6	58	16
7	59	17
8	60	18
9	61	19
10	62	21
11	63	22
12	64	23
14	66	24
15	68	26
18	70	28
22	74	32
25	77	35
29	82	40
34	86	44
38	90	48
55	108	66
68	121	79
90	142	101
525	577	535

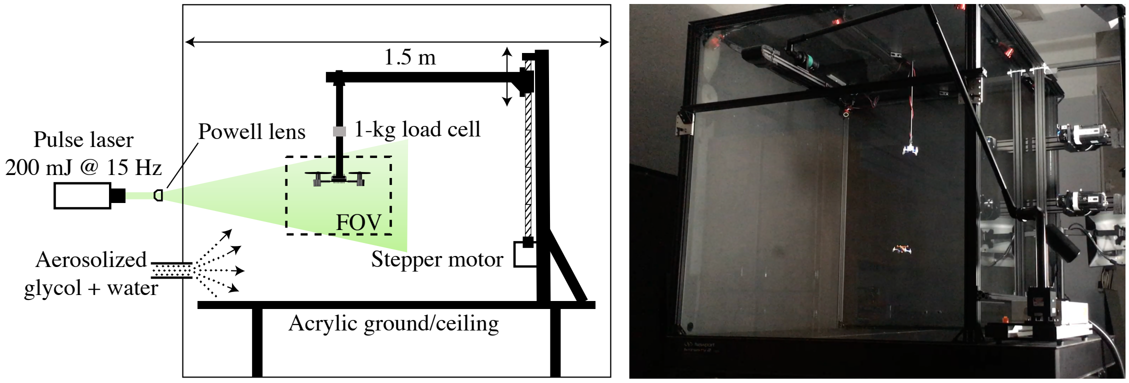

Figure 4.1: A glass arena was used to measure the lift of a tethered Crazyflie and the surrounding flow field via Particle Image Velocimetry (PIV).

4.1). Based on a convergence test, we determined that 150 image pairs (10 s of data) were sufficient for time-averaged velocity fields to converge to < 0.1% of the average projection error per 10 μm. The result of the averaged cross-correlations is a grid of velocity vectors, one for each 32 x 32 px window.

We used the velocity grids to plot airspeed density and trace streamlines (DensityPlot $\&$ StreamPlot in Mathematica 10). Areas that were unobservable due to poor contrast near the illuminated Crazyflie are shown as grayed areas in the figures. A light reflection caused the one-pixel outlier seen in the ceiling case. Downwash velocities were estimated by using a cross-section of the wake 1 rotor diameter beneath each rotor. The momentum jet was angled slightly to the left in some flowfields near the ground (see Results, Fig. 4.4), which motivated us to test the sensitivity to rotor angle. We therefore ran an additional set of tests with the artificial ground plane at 6 angles off the horizontal (+4.6°, +3.1°, +1.5°, -1.7°, -3.2°, -4.9°; each $\pm 0.05^{\circ}$).

4.3 Mathematical Models

The first attempt to model rotors in ground effect was done for helicopter landings. Cheeseman and Bennett [13] used mirrored source elements (method of images) to model the lift of a rotor (L) as it approaches the ground. Hayden [45] later added power to the model using a correlation based on flight test data. In the model, the rotor's image leads to downwash velocities at the rotor plane. The result is an increase in rotor lift compared to its value far from the ground (L_∞). Near-ground lift therefore depends on the altitude, Z, according to

$$\frac{L}{L_\infty} = \frac{1}{1 - \frac{1}{16\hat{Z}^2}}, \tag{Eq. 4.1}$$

where $\hat{Z}$ is the altitude scaled by rotor radius ($\hat{Z} \equiv Z/r$). The method, which is based on potential flow theory, assumes that the flow is incompressible and inviscid. It also assumes that the downwash is constant across the rotor disk, that the rotor disk is infinitely thin, and that $\hat{Z} > 0.25$.

To account for the extra rotors of a quadrotor, Sanchez-Cuevas et al. [16] modeled four sources (arranged in a square with side length ℓ), then applied the method of images. A secondary effect of there being four rotors comes from the quadrotor's symmetry. The flows from the four jets converge beneath the quadrotor, rise up in the center, further reduce the downwash at the rotor planes, and therefore cause an increase in lift. To account for this "fountain effect"[16], Sanchez-Cuevas et al. added a semi-empirical term with a fitted coefficient K_b. Their modified expression for near-ground lift is

$$\frac{L}{L_\infty} = \frac{1}{1 - \frac{1}{16\hat{Z}^2} - \frac{\hat{Z}}{\sqrt{\left(\hat{\ell}^2+4\hat{Z}^2\right)^3}} - \frac{\hat{Z}}{2\sqrt{\left(2\hat{\ell}^2+4\hat{Z}^2\right)^3}} - \frac{\hat{Z}}{2K_b\sqrt{\left(\hat{\ell}^2+4\hat{Z}^2\right)^3}}}, \tag{Eq. 4.2}$$

where $\hat{\ell} \equiv \ell/r$. The model is based on the same assumptions as the original helicopter theory [13]. Sanchez-Cuevas et al. found good agreement with experimentally-calculated lift when $K_b \approx 2$.

Ceiling effect analysis is fairly new due to the fact that previous ground effect studies were done for helicopter flight. Hsaio & Chirarattananon [17] modeled ceiling effect using blade element momentum theory and a control volume analysis. They found that – like in ground effect – the presence of the boundary decreases the downwash velocity at the rotor plane. Their model predicts a sharp increase in rotor lift near the ceiling, an effect that has been confirmed in experiments [33]. Specifically, their model predicts that

$$\frac{L}{L_\infty} = \frac{1}{2} + \frac{1}{2}\sqrt{1 + \frac{1}{8\hat{Z}^2}}, \tag{Eq. 4.3}$$

where here z is the distance between the rotors and the ceiling plane. Like ground effect theories, the model assumes that the flow is incompressible and inviscid, that the rotor disk is infinitely thin, and that the downwash through the rotor is uniform. They further assumed that the flow entering a control volume above the rotors was entirely horizontal. All of these models assume hovering flight, i.e. an advance ratio ($J \equiv \dot{Z}/(2rf)$) of zero, and assume lift coefficients that are independent of Reynolds number and rotor solidity.

4.4 Results

4.4.1 Tethered force measurements

Our tethered force measurements confirm that micro quadrotors – like their larger counterparts [16] – see a boost in lift near the ground (Fig. 4.2*a*). The lift increase that we measured (up to 20%) was more than twice what classic theory predicts [13]. Sanchez-Cuevas et al. [16] observed similarly high lift values and attributed the deviation from theory to the "fountain effect". When we use their one-parameter fit for modeling fountain effect (Eq. 4.2), we see a good match ($R^2 = 95.6\%$) for $1 < \hat{Z} < 3$. This suggests that their semi-empirical model scales well to smaller quadrotors. Fig. 4.2 includes all four of the throttles we considered; the collapse to a single curve illustrates that the relative lift increase near boundaries is insensitive to air flow speeds. For comparison, we show existing quadrotor data, classic helicopter theory (C-B Model; Eq. 4.1), and the Sanchez-Cuevas Model (S-C Model; Eq. 4.2) with its original fit (PQuad; $r = 120$mm, $K_b = 2$) and a new fit (Crazyflie; r = 23mm, K_b = 2).

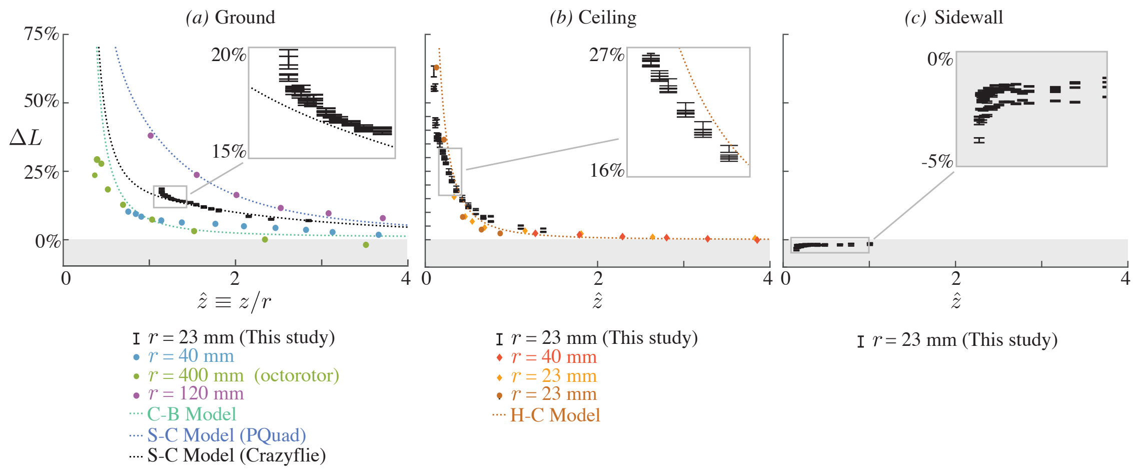

Figure 4.2: A comparison of recent modelled and experimental data for quadrotors near the sidewall, ceiling, and ground [27][26][16][13][17][25].

Near the ceiling, the Crazyflie experienced a sharp increase in lift (up to 60%) very close to the boundary (Fig. 4.2*b*). Our data go to lower $\hat{Z}$ values near the ceiling because the underside of the quadrotor prevents closer ground proximities. Like larger quadrotors, the Crazyflie had to be closer to the ceiling than the ground to experience the same increase in lift [16, 14]. Near the ground, effects on rotor lift were significant when $\hat{Z} \lesssim 4$; near the ceiling, effects only were significant when $\hat{Z} \lesssim 1$. The ceiling model of Hsaio & Chirarattananon [17] gives a good estimate of the lift increase except for very low $\hat{Z}$ values, where the model over-predicts our measurements.

Unlike near the ground and ceiling, the lift decreases slightly ($< 5\%$) near a sidewall (Fig. 4.2*c*). The sidewall effects are small in comparison to those seen near the ground and ceiling. The quadrotor has to be very close to the wall before changes in lift are noticeable ($|\Delta L| > 2\%$ for $\hat{Z} \lesssim 0.3$). This proximity, corresponding to just a few millimeters, would be outside the scope of most applications. However, unlike the ceiling and ground, which has a symmetric effect on the rotors, the sidewall presumably affects the rotors unequally, which would lead to destabilizing rolling torques. These torques are known to affect larger quadrotors [32]. For the Crazyflie, it appears that differential lifts of up to $\approx 0.03L_\infty$

are possible very close to the wall (Fig. 4.2*c*). Using the mass and moment of inertia of the Crazyflie (27 g, 2-3*10^{-5} kg m^2 [46]), we estimate rolling torques of ≈ 0.2 N mm and angular accelerations of $\approx$ 400 deg/s^2.

4.4.2 Flowfield measurements

Motivated by the slight differences between our measurements, existing models, and existing data for larger quadrotors, we conducted PIV to measure the time-averaged flowfields around the Crazyflie (Fig. 4.3). To avoid a laser shadow, we measured the flow around one rotor and reflected across the midplane the Crazyflie. The wake of the rotors is significantly different near boundaries, particularly near the ground. The ground causes each rotor wake to diverge into two momentum jets. Near both the ground and the ceiling, PIV reveals a reduction in the rotor downwash of $\approx 22\%$ (ceiling) and 6% (ground). In comparison, the classic model of Cheeseman & Bennett predicts only a 0.4% decrease in downwash at the same ground proximity. This discrepancy helps to explain why our lift increase near the ground was higher than what classic theory predicts (Fig. 4.2*a*).

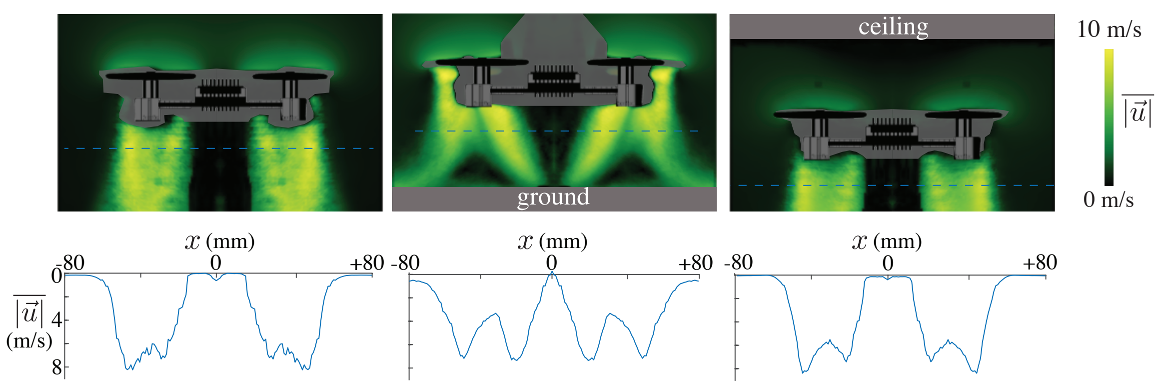

Figure 4.3: Time-averaged velocities near the ground ($\hat{Z}$ = 3.4, center) and ceiling ($\hat{Z}$ = 2, right) differ in direction and strength compared to the control ($\hat{Z} \gg 1$, left). Velocity cross-sections shown below.

To better understand how the ground affected the flow, we considered multiple ground proximities and compared with the control case (Fig. 4.4). In the comparison, negative values imply that the flow is slower than the control case; positive values imply that the flow is

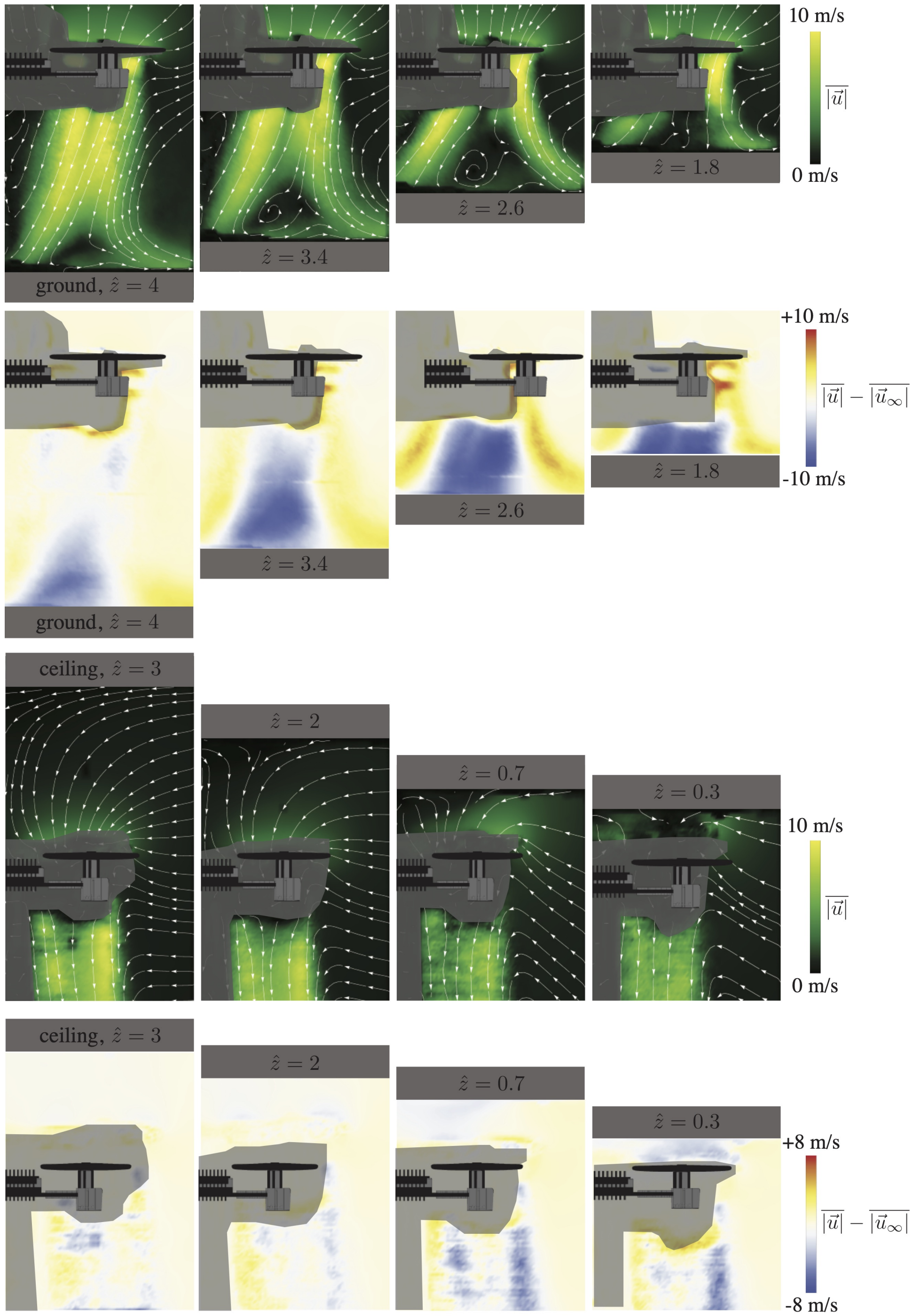

Figure 4.4: Time-averaged velocities near the ceiling/ground are compared against the control to highlight areas of high variation.

faster. As the Crazyflie approaches the ground, the momentum of the rotor wake is directed to either side, leaving a triangular stagnation zone beneath the rotor. As $\hat{Z}$ decreases further, the stagnation zone grows until it nearly reaches the bottom of the quadrotor. Quasisteady analyses would suggest high pressures in this zone, which could help to explain why the ground causes lift to increase even at relatively high $\hat{Z}$ values (up to ≈ 4). Compared with the control case, the near ground wakes also show relatively high airspeeds just outside the stagnation zone. These higher airspeeds are particularly pronounced very close to the wall (Fig. 4.4, $\hat{Z} = 2.6$, $\hat{Z} = 1.8$), suggesting that near-ground dynamics may also be affecting jet entrainment below the rotor.

In comparison to the ground, the change in downwash of the ceiling on the flow was less pronounced (Fig. 4.4). For the first two cases we considered ($\hat{Z} = 3$, $\hat{Z} = 2$), the flowfields are almost identical to the control case. In contrast, even when $\hat{Z} = 4$ near the ground, the flow is significantly altered by the boundary (Fig. 4.4). This difference is consistent with our lift results (Fig. 4.2*a,b*), which showed how lift was affected at higher $\hat{Z}$ values near the ground compared with the ceiling. As $\hat{Z}$ reduces further near the ceiling ($\hat{Z} = 0.7$ and $\hat{Z} = 0.3$), the flow both above and below the rotor becomes less uniform than in the control case. The streamlines bringing air to the rotors now approach at an upward angle, and the airspeeds are slower just above the rotor and beneath the rotor tips.

To test the sensitivity of rotor angle, we also performed PIV with rotated ground planes (Fig. 4.5). We observed no noticeable affects of rotor tilt angle on the flow above the rotor. In contrast, the wake beneath the rotor was considerably affected by tilt angle. In all cases, the jet beneath the rotor split in two and left a region of slow-moving flow, as we had seen previously. However, the topology of the split and the streamlines in the slow-moving region were very sensitive to tilt angle. At some tilt angles ($\theta_{\text{tilt}} = +4.6^{\circ}$, $+3.1^{\circ}$), two stable pairs of counter-rotating vortices are seen beneath the rotor. As the tilt angle decreases, the vortices are replaced by a single counter-clockwise vortex. This sensitivity could explain some of the asymmetries seen in the jet near the ground. Even slight imperfections in rotor tilt angle could cause different wake dynamics in and around the stagnation zones beneath the rotors.

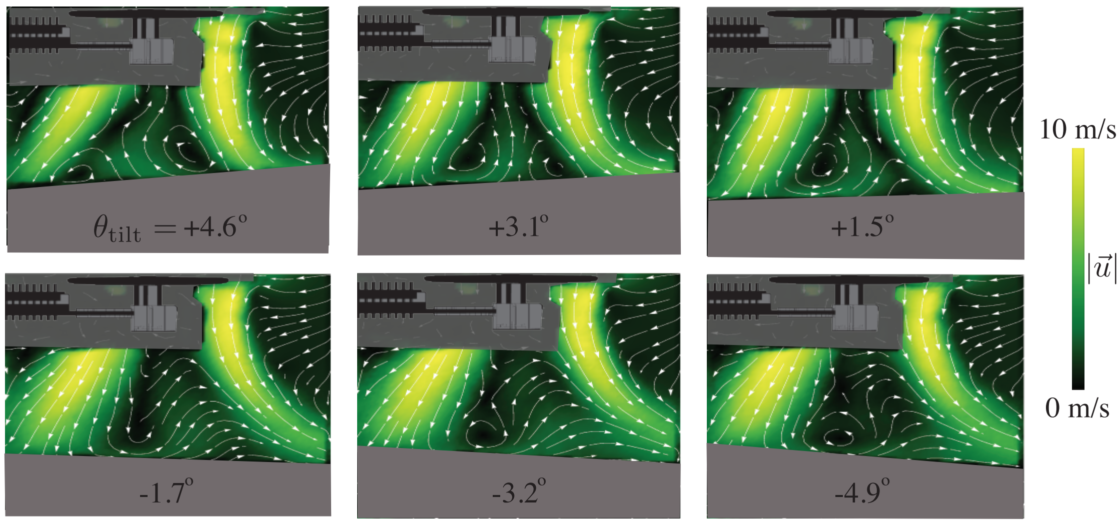

Figure 4.5: Time-averaged velocities near a horizontally tilted ground plane show the sensitivity of the Crazyflie's wake to tilt angle.

4.5 Discussion

In general, the Sanchez-Cuevas model works well to model the lift forces we observed near the ground. The same K_b value that they used to account for the ”fountain effect” (2) also fit our data well (Fig. 4.2). In the final few altitudes we tested, just before the quadrotor touched the ground, our lift results began to deviate from the Sanchez-Cuevas model. We did not see strong evidence of an upward jet beneath the rotors (Fig. 4.3, 4.4), which could perhaps explain the discrepancy. However, there may be an upward jet beneath the center of the quadrotor, out of the plane of the laser. Understanding these subtle changes in the rotor wakes is important for developing more advanced near-boundary models, especially because rotor-rotor interactions also affect performance [21].

In light of our tilt analysis (Fig. 4.5), modeling secondary vortices may also help improve near-ground MAV models. The robust appearance of the vortices in time-averaged flow fields suggests that they are stable. However, their topology is sensitive to tilt angle, and they can disappear with even slight ($\approx 3^{\circ}$) changes in attitude (Fig. 4.5). We did not record any significant sensitivity to tilt angle in the thrust, so these vortices may play a minor role in scaling the time-averaged forces/torques on the vehicle, but their appearance could have important implications for landing stability or ground particle dispersion.

Except for very close ceiling proximities, the ceiling model from Hsaio & Chirarattananon, [17] also gives good estimates of our lift results. It appears that both the Sanchez-Cuevas and Hsaio & Chirarattananon models can scale down to micro quadrotors. As for the deviation from model predictions that we see very close to the ceiling (Fig. 4.3, $\hat{Z} \lesssim 0.5$), we suspect that viscous effects are no longer negligible over such small length scales. In the inviscid model of Hsaio & Chirarattananon, rotor downwash is assumed constant, the streamlines entering the control volume above the rotor are horizontal. Our PIV measurements reveal that these assumptions begin to break down very close to the ceiling. However, we expect that the more dominant effect is a change in pressure above the quadrotor caused by interactions between the rotor and the boundary layer on the ceiling.

One application of near-boundary models is sensorless boundary detection. Using known lift-altitude relations, a quadrotor could predict its proximity to a boundary based on throttle alone. This type of heightened situational awareness would be particularly helpful in situations where other sensing modalities may be compromised. Using a ground model has, for example, been shown to facilitate sensorless landings [37, 38, 39] and swarm-based blind terrain mapping [23]. Our force measurements and simulations offer design suggestions for this technique. The collapse we observed with throttle (Fig. 4.2) implies that model-based boundary detection could work with the same calibration even with different payloads. Sensorless sidewall detection is unlikely to be accurate enough based on changes in lift (Fig. 4.2*c*).

Perhaps the most promising application of near-boundary models is safer, more efficient path-planning – especially in boundary-rich environments. It has been shown that flying near boundaries can save energy [22, 17], and thus path-planning algorithms can be made more efficient by incorporating near-boundary models [39].

4.6 Conclusion

Micro aerial vehicles demonstrate the near-boundary effects seen in larger flight vehicle systems. Sidewall boundaries create a small change in lift force compared to ground and ceiling planes. Ground and ceiling effects on MAVs match the trends of current models and experimental data. The variation between the models and data may stem from differences in vehicle size and shape. The flow field images indicate a stagnation zone between the rotors, while in ground effect no sign of fountain effect was observed. We show a prominent boundary layer for our MAV platform due to stronger viscous forces. The flow field of a ceiling effect MAV indicated upward angled inflow, indicating vertically-directed momentum on the MAV. At small horizontal tilt angles, there were small alternating vortices in some cases, but they did not cause noticeable changes in lift.

Chapter 5

Near-Boundary Flight Applications

As mentioned in the introduction, UAVs have become very popular in recent years due to their myriad of potential applications. Micro Aerial Vehicles (MAVs) enable particularly novel applications thanks to their lower cost and multidisciplinary use. When a UAV flies near a ground or ceiling, it experiences an increase in lift. This lift increase represents a decrease in the thrust required to keep the UAV aloft and thus a decrease in energy consumption. This chapter will discuss different applications that can utilize these surface effects to create a more efficient and versatile flying vehicle.

Five potential applications will be discussed here: (1) We will investigate the ability to detect surfaces and land without sensor input. (2) We will use boundary models to develop optimal energy efficient flight plans. (3) We will investigate the connection between crashing frequency and near boundary flight. (4) We will simulate the gust forces on quadrotors to determine how this would effect other vehicles nearby. (5) We will link a vehicle's IMU (Inertial Measurement Unit) to the wind velocities in the surrounding flow field.

5.1 Surface Detection

Ground and ceiling effects have been used actively in many robotics applications. In [22], the authors leveraged the ceiling effect to perform bridge inspections by maintaining con-

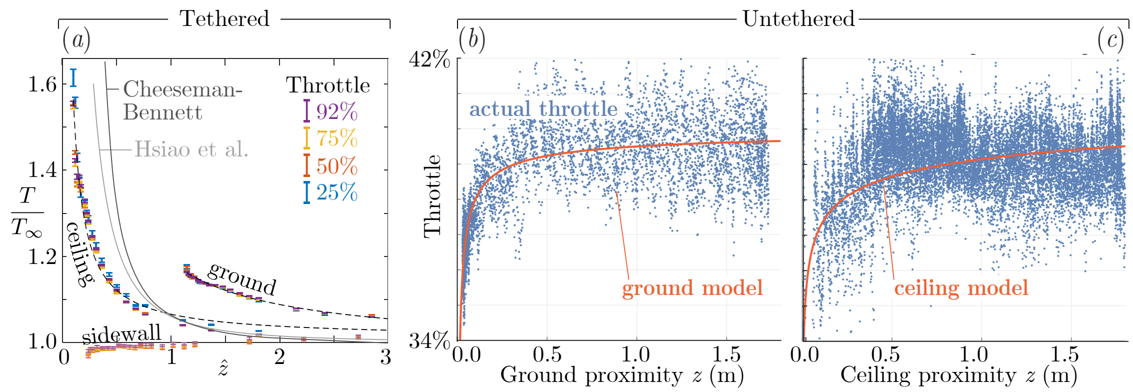

Figure 5.1: a) Models and experimental data showcasing thrust changes due to near boundary flights preformed at UVA. b,c) Descending and ascending quadrotor data with fitted model of throttle .

tact between a specially-designed UAV and the ceiling. Authors in [23] exploited the ground effect to perform blind terrain mapping, and [24] treated near-surface effects as disturbances in order to improve multi-floor navigation and mapping inside buildings. In [29], the authors took into account the ground effect to improve the altitude controller of a helicopter approaching the ground. In particular, the authors adapt in realtime the gains of the collective controller and the engine gas controller according to the current height of the vehicle.

Although ground and ceiling effects have been actively used in many applications such as the ones described above, they have never been used for detecting near surfaces and for motion planning. For instance, it could be possible to detect the presence of the ground or the ceiling and leverage this information for collision avoidance or autonomous landing. Indeed, autonomous landing is currently performed using sensors such as cameras, ultrasonic sonars, IMU, GPS, optic flow, and Barometric pressure sensors [47]. These approaches, however, may require computational capabilities or heavier payloads, which are challenging in small-sized UAVs. Moreover, some sensors may be malfunctioning or could be inaccurate in harsh conditions such as low-light and dust.

We propose here a sensorless surface detector that leverages the thrust reduction occurring when approaching a surface. The surface detector could be used for collision avoidance or autonomous landing. Additionally, the thrust reduction could be used to reduce energy consumption and increase flight time. For instance, in [22], the authors observed an increase in the maximum flight time of the UAV while being in contact with the ceiling.

When a quadrotor is close to a surface, it benefits from an increased lift, i.e., the thrust required for hovering decreases. To further characterize such a behavior, we performed a set of experiments by flying an untethered quadrotor at different distances from the ground and a ceiling surface.

To explore how ground effect models could improve sensorless landings, I teamed up with the Autonomous Mobile Robots Lab at UVA (PI: Nicola Bezzo). We designed a set of experiments that used untethered AscTec Hummingbird quadrotors controlled by Robot Operating System (ROS). The experiment was performed indoors in order to capture the motion of the quadrotor with high precision through the use of a VICON motion capture system. A 1.8 m by 0.9 m PVC transparent board was placed at the height of 1.95 m and used as a ceiling surface.

We performed two experiments to characterize the impact of the ground and ceiling effects on the thrust given to the quadrotor and to confirm the results presented in the previous section. In the first experiment, the quadrotor hovered for 10 s at 12 different positions from the ground and ceiling, respectively. For each distance, we collected the throttle given to the UAV.

In the second experiment, we measured the throttle during an ascending trajectory from the ground to the ceiling surfaces, and vice-versa without stopping at intermediate points. We repeated the ascending and descending trajectories 5 times.

The results presented above confirm the analysis provided in Figure 5.1. The maximum thrust reduction from these experiments was 9.63% obtained by hovering at 5 cm above the ground. In the previous section, we recorded a 60% reduction because it was possible to move the Crazyflie propellers up to a few millimeters away from the surface since it was tethered. We obtained curves that are in line to the values observed in Fig. **??**.

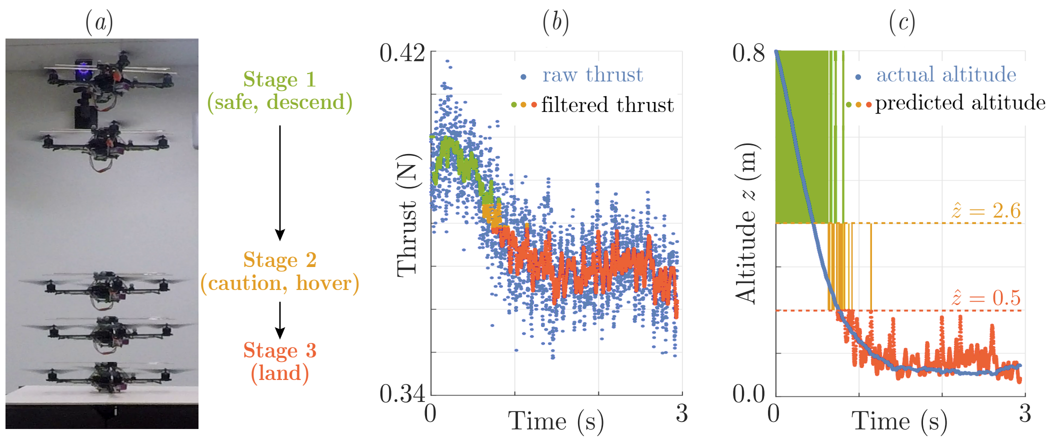

Figure 5.2: a) Time captured images of the descending and landing quadrotor b) Thrust vs time graph c) Descending quadrotor data with colors showing the three stages of landing .

To validate the floor-detecting method, we have used an AscTec Hummingbird quadrotor. We used ROS to control the quadrotor and the VICON motion capture system to get the ground truth of the quadrotor's position. The throttle was measured at the frequency of 100 Hz, with the quadrotor descending at a speed of 0.1 m/s. The position control algorithm loop was run at a frequency of 10 Hz.

Sensorless landing is possible using experimentally-captured lift curves. Our work used a closed laboratory setting to determine the near-boundary lift curves. My work in understanding the scaling laws of near boundary flight can lead to model corrections without the use of motion capture equipment. Another consideration is that the lift curves and testing were done within the same conditions. In a real world application, understanding how the environmental changes can affect the lift curves are critical to allow for sensor-less landings.

5.2 Near-Boundary Optimal Path Planning

From a path-planning point of view, some algorithms minimize energy consumption by monitoring and re-planning based on wind disturbances [48] and by setting an optimal speed along the path [49]. While roboticists have studied path planning approaches that leverage characteristics of the environment, ground and ceiling effects are not typically exploited for navigation purposes. To test how well ground effect models could improve efficient path-planning, I again teamed up with the Autonomous Mobile Robotics Lab. For these experiments, we commanded the AscTec Hummingbird to fly in a 'U' shape near a series of 'ground' and 'ceiling' obstacles.

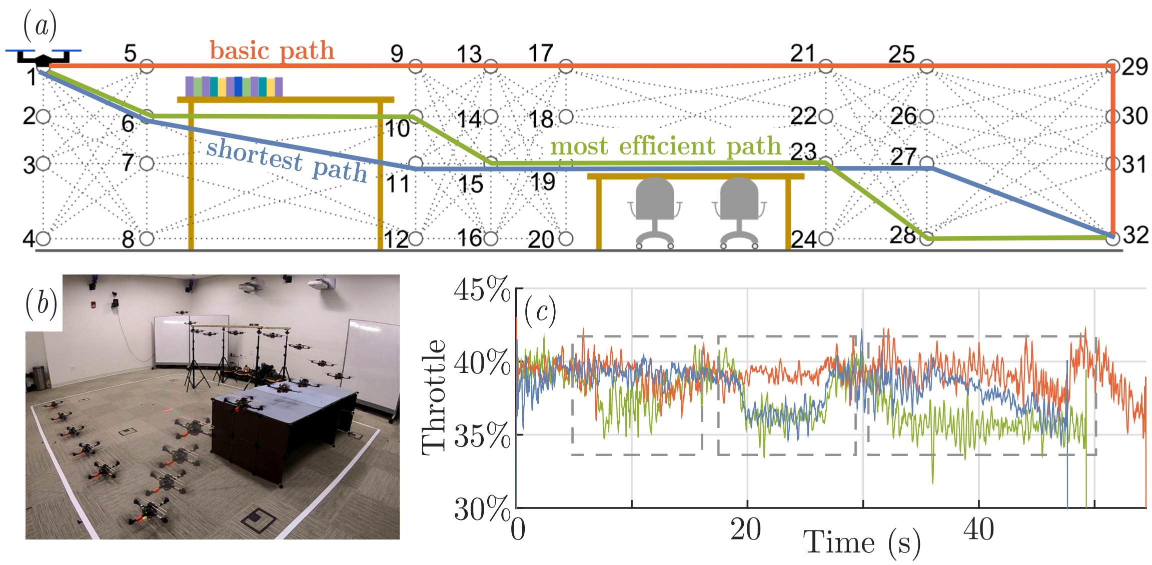

Figure 5.3: a) The paths chosen for landing including one optimized to benefit from near-boundary effects. b) Time capture of the quadrotor in testing. c) Throttle used to hover during testing sequence. .

Two intermediate waypoints were placed at each of the corners of the U shape. A 0.9 m $\times 1.8$ m transparent PVC board was set at 1.14 m above the ground as the shelf. The table (0.9 m $\times 1.8$ m $\times 0.6$ m) was between B, and C. Most of the ground surface was available except the part under the table. Four different cases were tested: 1) a basic path in which the quadrotor started from A and traveled in mid-air through the intermediate waypoints and landed in D; 2) the shortest distance path computed using the distances between vertices as edge weights; 3) the minimum energy path computed with our approach; and 4) the minimum energy path computed with our approach, but in a scenario without two of the surfaces.

The first path was chosen since it was the most intuitive way to operate if the surrounding environment is not exploited. The second path is the one that is typically used since it aims at minimizing the travel distance. The third path is the one that leverages the surrounding surfaces to minimize energy consumption while the last one is used for comparison purpose.

For each experiment, we performed five flights in which we measured the total throttle given to the quadrotor.The total thrust is proportional to the total energy:

$$\hat{E}_{Traj} = \int P dt \propto \int F^{3/2} dt. \qquad \text{(Eq. 5.1)}$$

For ease of discussion, here we will use the last term on the right-hand side of (Eq. 5.1) to compute the total energy during a trajectory since we can measure the throttle provided to the UAV.

Consider the throttle differences between the basic path and the optimal path. We can see a significant thrust reduction for the optimal path. The optimal path consumed 15.86% less energy and also took less time. The figure also shows three dashed rectangles highlighting the average throttle reduction given by traveling close to the surfaces. This comparison highlights the throttle reduction that appears when the UAV flies underneath the shelf and above the table. In fact, the same path without the surfaces consumes about 4% more energy. Finally, consider the shortest distance path with our approach. Although the shortest path travels a shorter distance and takes less time to complete the mission, our boundary-effect-driven approach still consumed less energy.

Table 5.1: Experimental results of predicted and measured energy*

Path	Predicted total energy	Measured total energy	
		mean	***std***
Basic path	13.0843	13.3168	0.0221
Shortest path	11.2445	11.5944	0.0289
Optimal path	10.7906	11.2050	0.0111
Optimal path (no surfaces)	11.2622	11.6627	0.0587

∗ The energy consumption is estimated as a function of the throttle.

Table 5.1 summarizes the total energy computed using (Eq. 5.1) for both the simulation and the actual experimental trials. For the experiments, we provide the mean value and standard deviation over five executions.

It is possible to see that the total measured throttle during the real flights is very close to the predicted one, confirming the effectiveness of our energy model. The slight difference between the values is due to noise, modeling errors, and the fact that the actual distance of the UAV from the surface may be different from the fixed value chosen for computing the edges.

Path planning is optimized by using a surface-based method. The two assumptions that were used with this method were constant distance away from boundary and one distance was used for either ground or ceiling effect. Using our modeling, this algorithm could be optimized to use varying distances from the boundary. In order to better understand how close a vehicle can safely get to a boundary, we conducted simulations as well.

5.3 Near-Boundary Simulations

Better ground effect models could also inform near-boundary risk-analyses. These types of analyses will be critical for generating the provably safe flights that MAVs will need before operating in human-rich environments. To explore how ground effect models could inform risk analyses, I worked with fellow graduate student Lauren Bouchard to generate reduced-order simulations of near-boundary quadrotor dynamics to determine relative crash propensities. The simulation allowed us to compare crash rates of different boundary models across a range of flight altitudes, using the Crazyflie's dimensions ($r = 23\,\mathrm{mm}$, $\ell = 90\,\mathrm{mm}$) and weight ($27\,\mathrm{g}$) as an example. We also analytically estimated the relative power required to maintain a given altitude. This information, together with the crash propensities, highlights efficiency-safety tradeoffs inherent in near-boundary flight.

To estimate L at distances far from a boundary, the simulations used blade element theory: $L = 4C_L \rho f^2 r^4$, where C_L is the lift coefficient of the rotor blade. We included the 4 to account for the four rotors, and we held C_L constant at 1.6 (in doing so, we assumed lift coefficient to be independent of Reynolds Number). This lift force served as L_∞ for the calculation of the near-boundary lift indicated by the Hsaio-Chirarattananon and Sanchez-Cuevas models (Eqs. 4.2 and 4.3). We used Sanchez-Cuevas's empirically fit $K_b = 2$ in our ground effect model [16]. To avoid unreasonably large lift values (and the singularity near $\hat{z} = 0.25$ in the ground model), we bounded L/L_∞ to its value computed at $\hat{z} = 0.5$. To assess the sensitivity of vehicle safety to the accuracy of the boundary model, we also simulated vehicle dynamics with boundary models scaled by powers of 0.6, 0.8, 1.2, and 1.4. For example, the lift in one simulation would be computed as $(L/L_\infty)^{1.4}$, such that the lift is always greater than L/L_∞ indicated by the model yet still approaches L_∞ at distances far from the boundary.

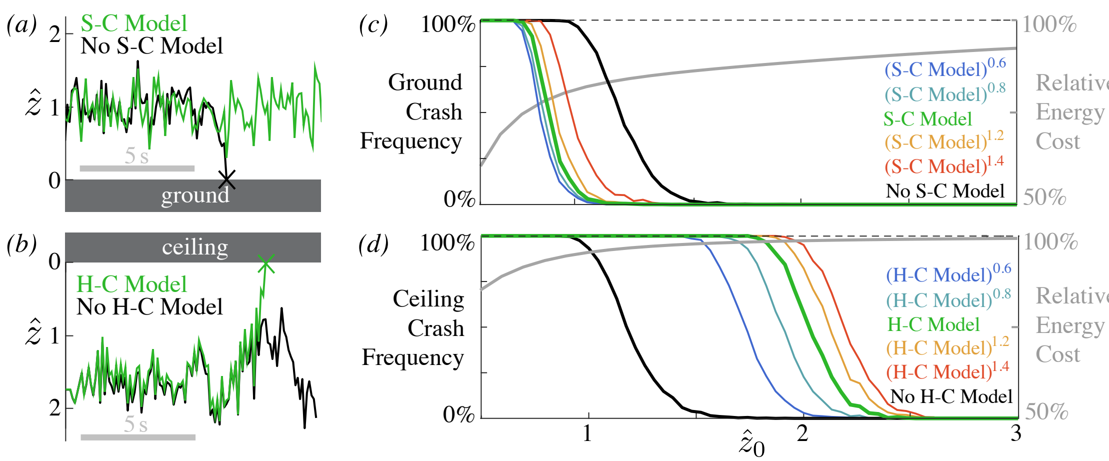

Figure 5.4: Frequency of Crashing due to the effects of near boundary flights .

Vehicle target heights ranged from $\hat{z}_0 \approx 0.5$ to 2 above ground and $\hat{z}_0 \approx 1$ to 2.5 below the ceiling (where $\hat{z}_0 \equiv z_0/r$). If at any time during the simulation $\hat{z} \leq 0$, we considered the vehicle to have crashed into the boundary and thus stopped the simulation, adding to a counter whenever this happened. Simulations of each combination of setpoint and boundary model magnitude were repeated 1000 times to determine an average crash rate at each parameter combination.

In contrast, the relative energy cost of hovering near a boundary can be determined analytically since it reduces to a function of our boundary model. We combined our lift models with blade element theory, which provides the mechanical power generated by a rotor as $C_P \rho f^3 r^5$, where C_P is the power coefficient. For the small advance ratios ($J \equiv \dot{z}/(2rf)$) of hovering, C_L and C_P are relatively constant (e.g. ¡ 5% change for $J < 0.2$ for a typical rotor [50]). The ratio of power consumed in two different flight conditions 1 and 2 is therefore $\approx (f_1/f_2)^3$. Inverting $L = C_L \rho f^2 r^4$ gives the frequency f required for hover as a function of $\sqrt{L}$. Therefore, the mechanical power generated near a boundary compared to the power far from the boundary (”relative energy cost”) is $(L/L_\infty)^{-3/2}$.

Our reduced-order simulations demonstrate that the ground has a stabilizing effect while the ceiling has a destabilizing effect. Random fluctuations cause the quadrotor to deviate from its target height, which could potentially lead to crashes with a nearby boundary. However, as a quadrotor approaches the ground, the heightened lift pushes the quadrotor upwards and prevents a crash (Fig. 5.4*a*). In contrast, approaching a ceiling leads to higher forces toward the boundary, which can result in a crash (Fig. 5.4*b*). To explore the likelihood of crashes, we aggregated hundreds of trials and looked at average crash rates.

On average, the simulated quadrotor crashes less near the ground when a ground model is included in the simulation. With no boundary model, random fluctuations cause crashes as high as $\hat{z}_0 \approx 1.5$ (Fig. 5.4*c*). When a ground model is added, the quadrotor can be about half of a rotor radius closer to the ground before this rise in crash rate. Scaling the ground model causes only slight changes in the $\hat{z}_0$ value at which this rise occurs.

Unlike a quadrotor near the ground, a quadrotor near the ceiling experiences more crashes. On average, the quadrotor is likely to crash into the ceiling when $\hat{z}_0 <\approx 2$ (Fig. 5.4*d*). Scaling the models has a stronger effect on the safe $\hat{z}_0$ range near the ceiling than it does for the safe range near the ground. The effects differ in magnitude because they are caused by different mechanisms. The ground acts as a buffer that pushes the quadrotor away; crashes require large random fluctuations. The ceiling acts as an attractor, pulling the quadrotor into a positive lift feedback loop; crashes are inevitable unless the controller can reverse course in time.

For comparison, we also plotted the relative energy costs of near-boundary flight in order to highlight the tradeoff between safety and efficiency. This relation makes it clear why near-boundary flight is more efficient: as $\hat{z}$ drops, L/L_∞ goes up, requiring a smaller rotor frequency and less energy to maintain altitude. Chances of crashing increase with smaller $\hat{z}_0$, however, so accurate models are critical for balancing safety and efficiency near the ground/ceiling (Fig. 5.4*c,d*).

Note that the value of the safe/unsafe $\hat{z}$ values depends on the disturbance intensity and the PID gains injected into our model. Varying the intensity or the gains would rescale the $\hat{z}$ values in Fig. 5.4, though the relative positioning of the curves – and therefore our conclusions about crash frequency – would be unaffected.

5.4 Multi-Vehicle Interaction Simulation

To explore the accuracy of reduced ordered quadrotor flight simulation, I worked with fellow graduate student Lauren Bouchard. Together, we analyzed a set of flight tests conducted by Esen Yel in the Autonomous Robotics Lab at UVA. In the experiments, a quadrotor was commanded to move horizontally above or below a second hovering quadrotor. This was repeated with two flight velocities across eight relative altitudes. We compared these experimental flight paths to our simulated flight paths with six different flow models. Our simulations first used heuristically-determined parameters based on physical aircraft dimensions and common gain tuning methods. Lastly, we explore a variety of fitting scenarios to determine how our inputs relate to the accuracy of the model predictions.

To simulate a quadrotor's flight, we employed a reduced-order simulation of the vehicle's dynamics and controls. While several quadrotor control models exist [51], [52],[53] we chose to use a cascaded Proportional-Derivative (PD) controller similar to prior work

[54] because of its simplicity and tracking efficacy. An external forcing representing a flow field is included in the dynamic equations of this model.

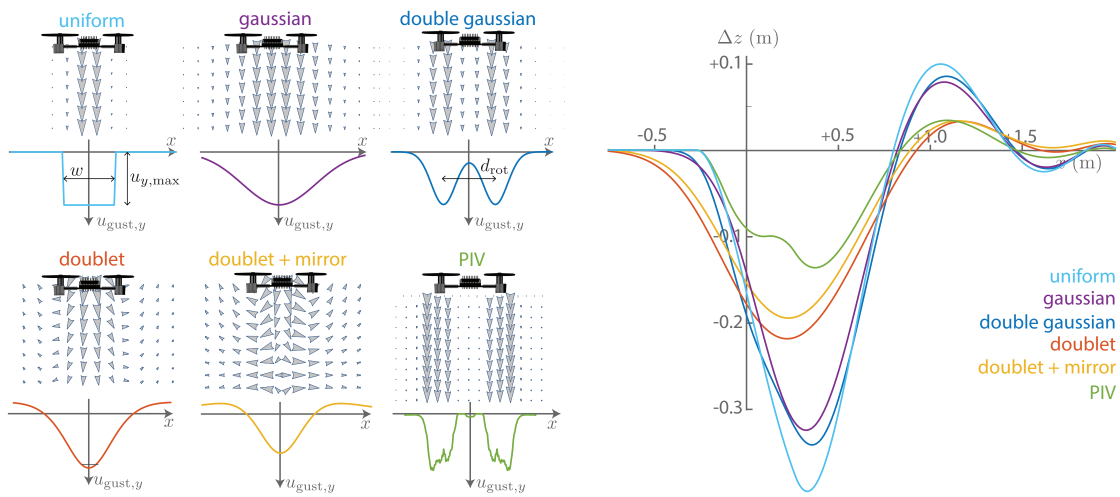

Figure 5.5: Left: vector field representations of each of the six flow field models used for the simulation. Right: example traces of simulated quadrotor flight through each of the flow fields. .

The simulated quadrotors were flown through six different flow field shapes (Figure 5.5). These models provided horizontal and vertical velocity components (u and v, respectively) as functions of the relative position of the two quadrotors (x_d and z_d). The speeds u and v are ultimately used to estimate the force on the aircraft.

The last flow model we tested used Particle Image Velocimetry (PIV) data from this thesis [55] to estimate the velocities below a hovering quadrotor. The flow field measurements were taken around a Crazyflie micro quadrotor, thus we scaled the position of all the measurements by the relative arm length of the hummingbird compared to the Crazyflie. The cross-section of data was taken at half an arm length below the vehicle. We considered only the vertical component of the flow, thus treating the PIV-informed model similarly to the vertically-independent functions described above.

The PIV flow was also normalized by its maximum value for equal comparison to the other flow models, i.e. the maximum value of the normalized flow is 1. The other models are normalized as follows: the maximum value 1 m below the doublet is 1, the maximum value of the Gaussian is 1, and the uniform flow has a magnitude of 1. The maximum values of the doublet plus mirror and double Gaussian models are not exactly 1 because of the interference of the second flow. Their maximum values are 0.94 and 1.02, respectively.

While the six flow models describe the general shape of the flow field, the magnitude of each flow must be scaled to better approximate real velocities beneath a hovering quadrotor. Our baseline simulation used an anemometer measurement beneath the hovering hummingbird quadrotor to do this: we multiplied the normalized flow field velocities by our measured value of 6 m/s for a more realistic estimate of the flow's strength.

The experimental data reveal several notable trends (Figure 5.6). First, when the moving quadrotor flew above the hovering quadrotor, its flight closely adhered to the commanded flight path. This is in contrast to the flights below the hovering quadrotor, where the vehicle was deflected downward by 7-8 cm. Of those flights, there is no discernible pattern in the effect of relative commanded altitude on the magnitude of deflections.

We first consider the results of the heuristic baseline simulations (Figure 5.6a). All the simulations were successful at predicting a downward deflection as the moving quadrotor passed beneath the hovering quadrotor. The simulation with the PIV-based flow field was the most successful at predicting the actual flight path while the other models predicted vertical deflections several times larger than the actual deflection. In the slow case, the simulated flights also overshot the target altitude after they recovered from the disturbance.

The actual PIV flow had the lowest average error than the other six flow conditions. The PIV flow data were taken from a different platform from the ASTEC Hummingbird that was used for the experiment. Understanding the fluid flow of quadrotors is essential to understanding how a quadrotor affects its environment.

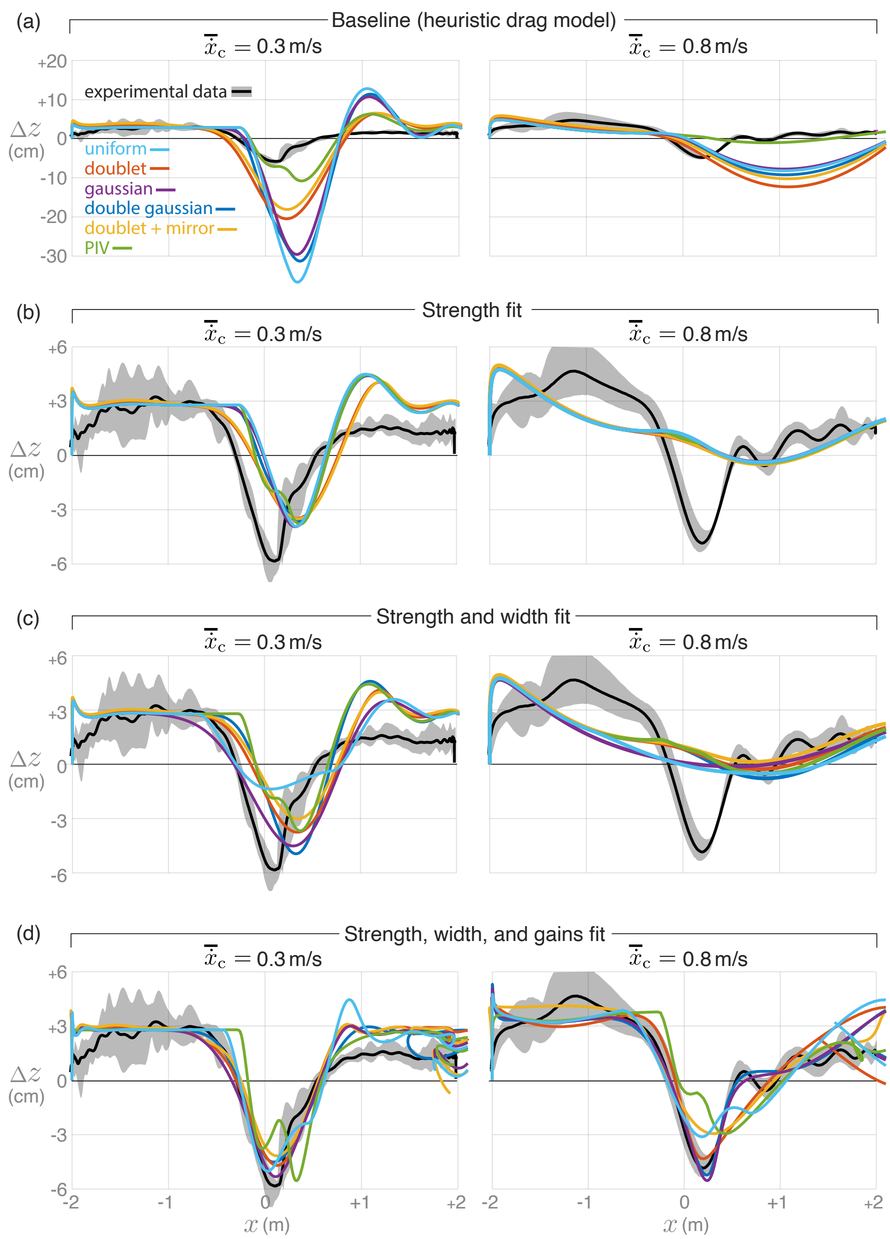

Figure 5.6: Simulated flight paths at the faster of the two flight velocities. The averaged experimental data is shown for comparison. .

5.5 IMU Wind Estimation

Undergraduate student Megan Mazzatenta and I explored the ability to use Inertial Measurement Unit (IMU) data to estimate wind velocity. Due to their hovering ability and light frame, Micro Aerial Vehicles (MAVs) have the potential to conduct cheaper wind measurements with greater spatial resolution than weather balloons. However, wind sensors increase MAV payload and therefore increase cost and decrease endurance. To avoid a mounted sensor, wind velocity estimation models have been constructed using on-board IMU data collected during flight. Existing models are able to relate IMU data to wind velocity, but they rely on calibrations and physical assumptions that limit measurement accuracy.

The Crazyflie MAV was flown in an arena equipped with OptiTrack cameras that track four reflective markers attached to the quadrotor. The Motive motion capture software streams position and orientation data to the Robot Operating System (ROS), where it is used for state estimation and control. Fans were placed as indicated by different colored fans below for three flow cases: jet, updraft, and vortex. The setup also includes a laser and cameras for conducting Particle Image Velocimetry (PIV) on airflow in the arena.

For all tests, the MAV was flown to each point in a 5x5 flight grid measuring 0.2m x 0.2m. The quadrotor hovered at each point for 45 seconds while logging IMU data. After landing, the battery was changed before the MAV was sent to the next point in the flight grid. The test was repeated for all 25 points in three different flow cases: still, jet, and updraft. In the future, PIV could be conducted on the flow in the flight grid for each different flow. IMU data from quadrotor flights in the still and jet cases were then analyzed to determine if the MAV was able to detect the flow using the collected data.

The results, especially the yaw data, show potential for using the Crazyflie MAV to measure wind velocity. However, more IMU data must be collected to identify trends and determine whether readings for the jet case are significantly different than those of the still

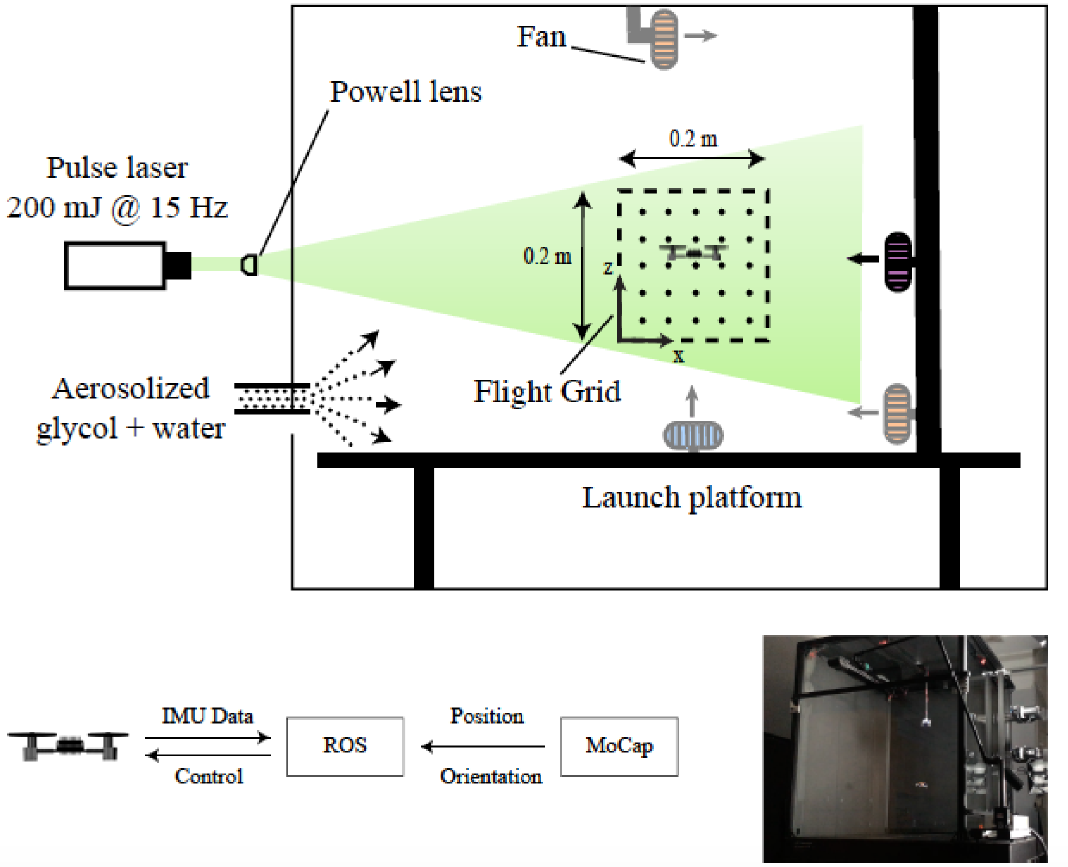

Figure 5.7: Above: MAV arena and testing equipment. Below: Data connections and Picture of Arena. .

control case. Therefore, more IMU data will be collected for the still and jet flows with PIV images taken for each case. Tests will also be run in the updraft and vortex cases. Data will then be used to evaluate how well existing models can estimate wind velocity using only IMU output, and results will be compared to PIV data to identify the assumptions in current models that are contributing to error in wind velocity estimation.

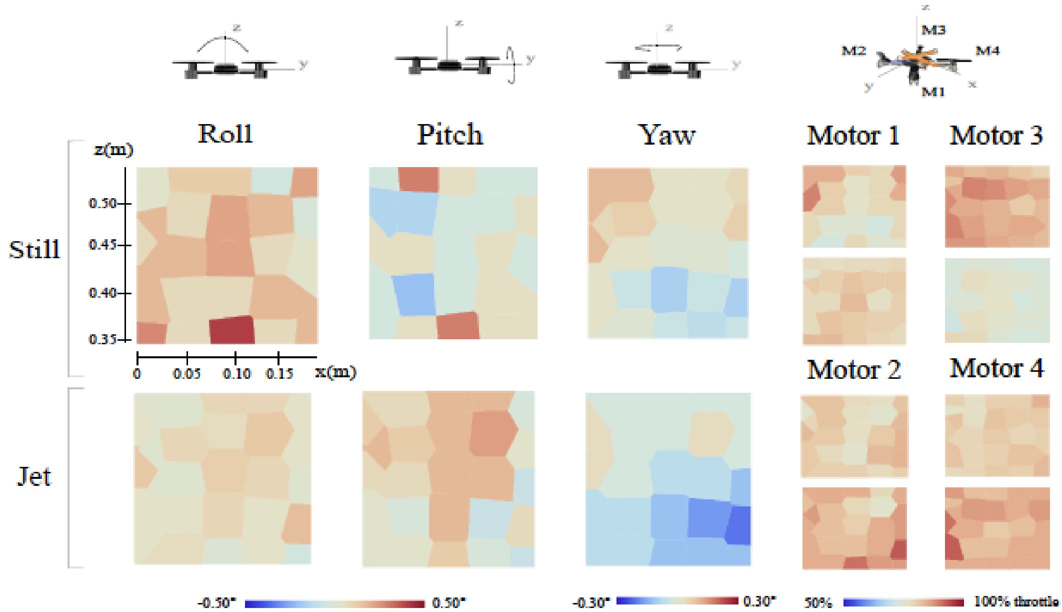

Figure 5.8: Hover forces and motor levels on a rotor during still and gusted conditions. .

5.6 Conclusion

Leveraging the equipment designed by our lab and near boundary effects, we were able to test a few near-boundary applications for UAV systems. Using the known ground effect experimental data, we were able to conduct sensorless landing experiments. My work on improving the models and understanding of ground effect on various rotors could lead to these landings being done without input from visual sensors. Surface-optimized path planning showed the energy saving potential of near-boundary flight. In a simple path planning experiment, we were able to demonstrate a saving of ~ 15% energy by utilizing boundaries. A safety study of near boundary models showcased how sensitive models are to input parameters, which can lead to higher crash frequencies. This further proves the necessity to generate more accurate near-boundary models, especially on a MAV-scale system where millimeters count. Utilizing our PIV to estimate the gust magnitude and direction led to the most accurate model of interaction between multiple vehicles. Through our MAV arena wind estimation testing, we demonstrated how IMU data could be used to estimate gust conditions.

Chapter 6

Rotor Property Dependencies in Solid/Water Ground Effect

Ground effect has been studied for a long time [13] due to the importance in helicopter landing. When it comes to landing on the water, this was only used in what is known as helicopter ditching [42]. No comprehensive study to the author's knowledge has been done on the ground effect phenomenon with multiple rotors over a water surface. The utility of this can be seen in examples like water sampling, which can be done over a large lake area shown in Figure 1.1. The energy saving and mission-extending ability seen in solid boundary ground effect is enough to make us curious. Similarly, these aerodynamic benefits have been seen in animals flying over the waters surface [11] [12]. However, since most UAUVs are optimized for aerial flights, not understanding this effect physically could lead to instabilities that could cause crashes. The amount of drag reduction due to ground effect is larger for a water surface than for a solid surface[12].

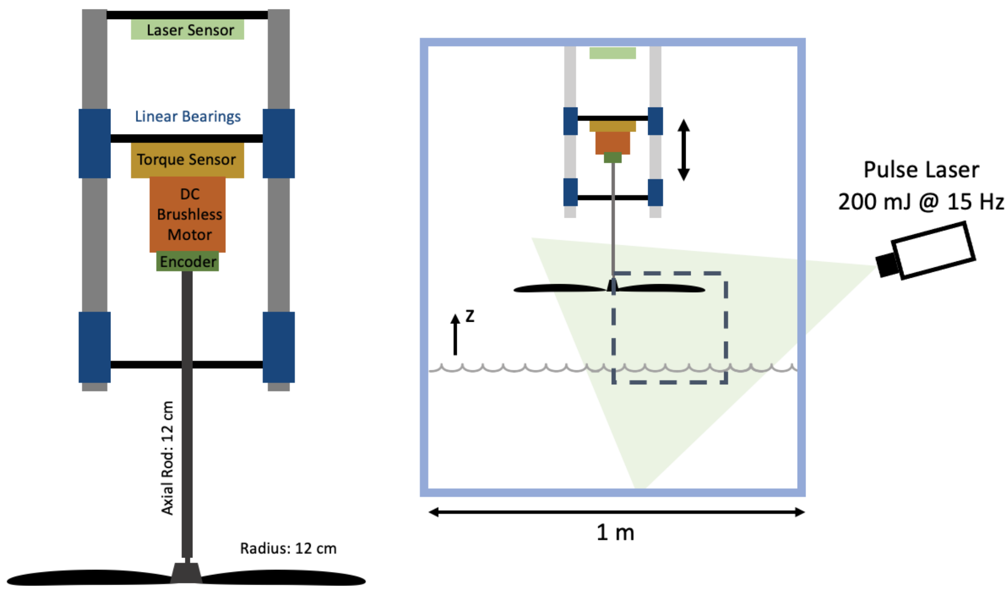

Figure 6.1: Left: Setup used to measure performance of the isolated rotor. Right: Schematic of rotor above water boundary with location of laser sheet and camera FOV.

6.1 Isolated Rotor over Water

6.1.1 Experiment Setup and Methods

Our goal from our system was to show that lift efficiency increased as a rotor neared a water surface. We used the rig from Chapter 2 so that our system was dynamic and free to move in the vertical direction. Our experimental procedure replicated Chapter 3 except for the water surface.

Boundaries within our testing arena play an important role in the results of our experiment. The main boundary we are interested in studying and manipulating is the water surface. We used tap water for our experiment that was room temperature ~ $20C$ The water was only seeded with neutrally buoyant tracer particles. The height of the water during test was adjusted to match the ground distance of interest. The water height level in the cube was between ~ 15 cm to ~ 40 cm. Within the testing cube itself Figure 6.1, which measures 1 m in all directions, the rotor was placed directly in the middle of the cube so the closest distance between the largest rotor tip and side wall was approximately ~ $36cm$. There were circulation affects in the air that we assumed to be negligible. There were transient affects in the water as well especially on the surface. We took experimental and PIV data long enough to see the steady state effects from the ground.

Time-averaged PIV was used to image the flow field of the rotors above the water's surface. The equipment and technique used for this experiment were identical to Chapter 3. The only difference was the angle of the laser. In the original test, the laser was parallel to the ground surface. However, when aligning the laser in that manner for a water surface, the waves caused by the air flow blocked the laser light. The blocked light from the perturbed water surface at the edge of the cube caused shadows in the camera's field of view. To account for this, the laser was raised a few centieters and then angled downward at ~ 10 $\deg$.

The testing in this experiment was done in two parts: (1) rotors hovered at specific $\hat{Z}$ values above the water and hovering frequencies were measured (2) PIV images were taken of these near-boundary rotors. The first step was determining the $\hat{Z}$ distances from the ground which were limited by the constraints of the systems. We could not go above $\hat{Z}$ = 2 because of the size of the cube, and we could not go below $\hat{Z}$ = 0.5 without the rotor crashing into the water due to instabilities in hover. With this in mind we measured data at $\hat{Z}$: [.5, .65, 1, 1.5, 2]. To average out the small oscillations from our PID control and its associated friction on the bearings, we captured data for 120 seconds. From these results, we conducted PIV on 6 different rotors (2 Diameters [25 & 28 cm] & 3 Pitches [3, 5, & 7 inches.]

6.1.2 Results

To compare experiments and models, we compared results near the water to the ground effect model derived in Chapter 3. There is no ground effect correction currently applied for a water surface compared to a solid surface. With this in mind, we used the traditional ground effect model from helicopter theory [43]. The model we use here is the same as the one used in Chapter 3.

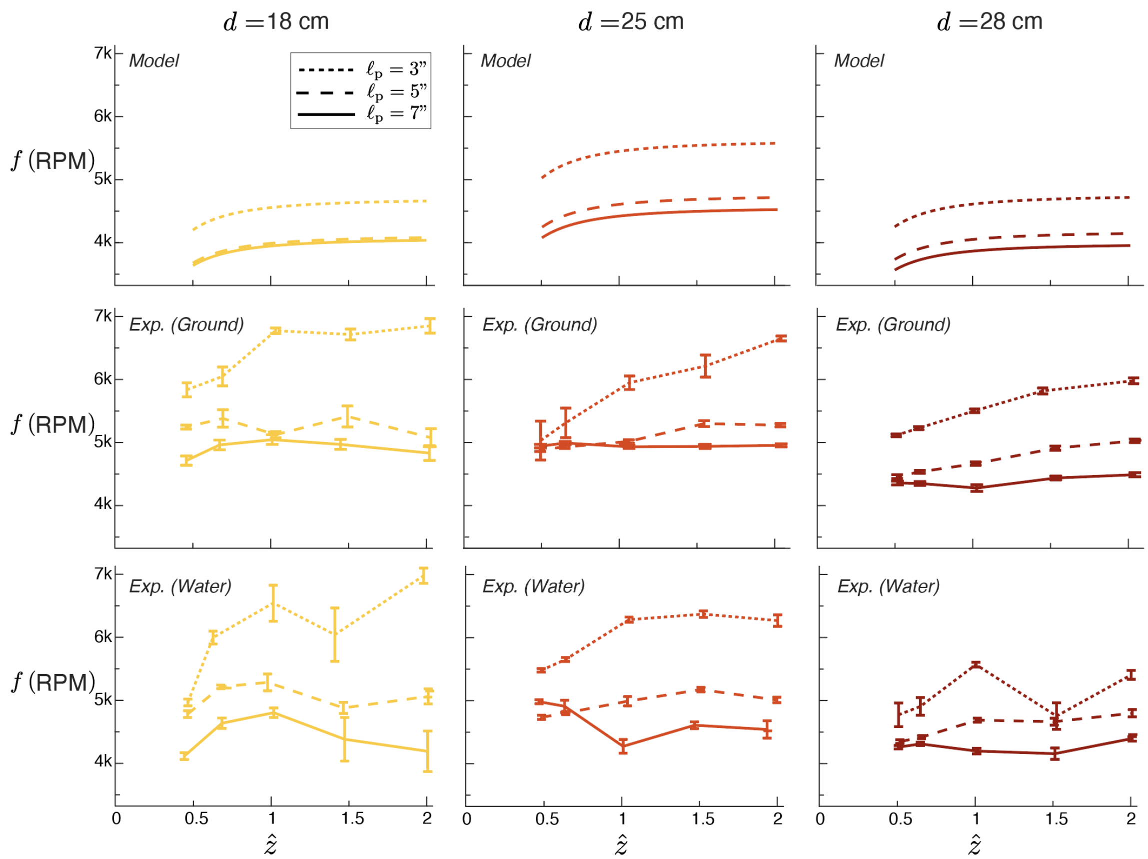

Figure 6.2: Top: Blade Element Theory combined with C-B Model to show the frequency needed to lift the experiments rig's weight. Middle: Hover frequency required to hover above the ground. Bottom: Hover frequency required to hover above water surface.

The model follows intuition by increasing the required frequency as the payload of a hovering rotor increases. In Figure 6.2, the top row of the figure shows the model results as line plots and is delimited into 4 plots showing the 4 tested rotor diameters. The colors reflect the diameter of the rotors where the smallest rotor (d = 18 cm) is the lightest as yellow and the largest rotor (d = 28 cm) is the darkest as maroon. The type of line from dashed to solid indicates which pitch was the blade. The model was created by using Eq: 3.7. The different pitches of the blades create three distinct levels of frequencies with similar paths to one another. The weight used for each model is based on the experimental weight which was consistent for each rotor diameter e.g. d = 28 cm the rotor system weight was 0.425 kg. All three rotor diameters show that the frequency decreases as the $\hat{Z}$ decreases. The frequency range for each rotor is similar between tests because we used counterweights to match the rotor's rated payload capacity. For all the rotor diameters, we see that as pitch decreases the frequency decreases as well.

The experimental data for water on the bottom row illustrates the frequencies necessary to maintain hover of our rotor system. In figure 6.2 (bottom row), we measured the frequency's average value and standard deviation at each of our prescribed $\hat{Z}$ values. The colors and line styles match the same pattern seen above for the model and ground experiment. The smallest pitch (3 inches) had the highest variation in frequency vs. distance to water. This pitch also showed the trend in all three cases that the rotor decreased frequency as it approached the surface. However in the two larger pitch cases, the blades had smaller slopes as the blades approached the surface.

Percent error showed no major trends in regards to the $\hat{Z}$ value (Figure 6.3). As $\hat{Z}$ decreased, there was a small increase in error as $\hat{Z} < 1$. For the error $\hat{Z} > 1$ we see a very steady error for most cases. For the case of d = 25 cm and pitch = 3 inches, we see a negative error as $\hat{Z}$ approaches 1. For the cases in which d = 18 cm, we do not see the trends as the other diameters and the error for these rotors are much higher. There does not seem to be a difference based on the pitch values of blades of the same diameter.

When averaging the percent error across all $\hat{Z}$s, multiple patterns and trends appear (Figure 6.3). The d = 18 cm cases all have substantially higher errors. The highest error was for pitch of 3 inches at around 30%, with pitches of 5 and 7 following next. For d = 20, 25, and 28 cm, the errors were concentrated in the 15-5% range and were similar. Even in the d = 18 cm case with a pitch of 7 inches, the error was below 20% and was more inline with the other blades. In the case of d = 25 cm and pitch of 3 inches, we see a high

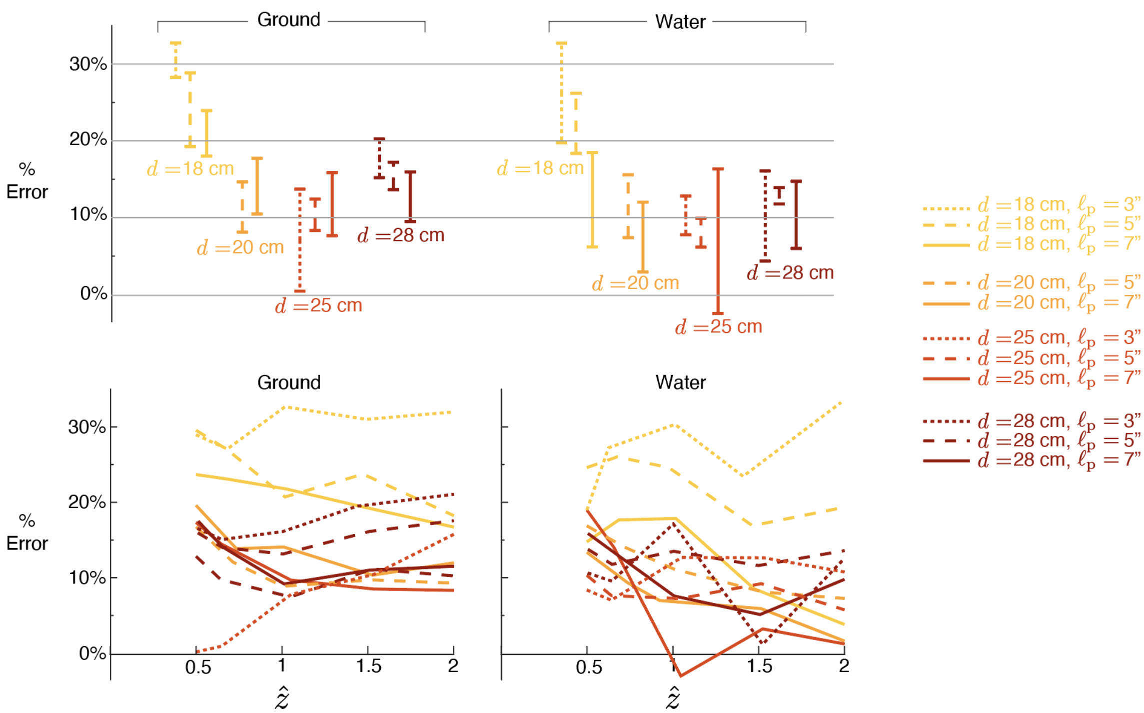

Figure 6.3: Absolute error between experimental data and model results. Left: Average error at all the distances for each rotor type. Right: Error versus distance to the ground or water.

variation that brought the error from

~

18% to -5% making this case have the lowest error.

The flow fields of the rotor shapes are dependent on the $\hat{Z}$ and less dependent on rotor size and pitch. In the top plot of Figure 6.4, we have the d = 25 cm rotor cases above water and solid surfaces. In the bottom plot of Figure 6.4, we have the d = 28 cm cases. The shapes of the steady state wake conditions were consistent across the three $\hat{Z}$ values: 2, 1, 0.66. In the water cases of $\hat{Z}$=0.66, the water caused splashing which distorted the data set. The stagnation zone witnessed in the ground case is seen in the water case. Unlike with the solid ground case, there is air passing through the ground plane into the water.

As the rotor is hovering above the water surface, it causes waves and deformation. The ground distance for each measurement is determined while the water is still. To visualize

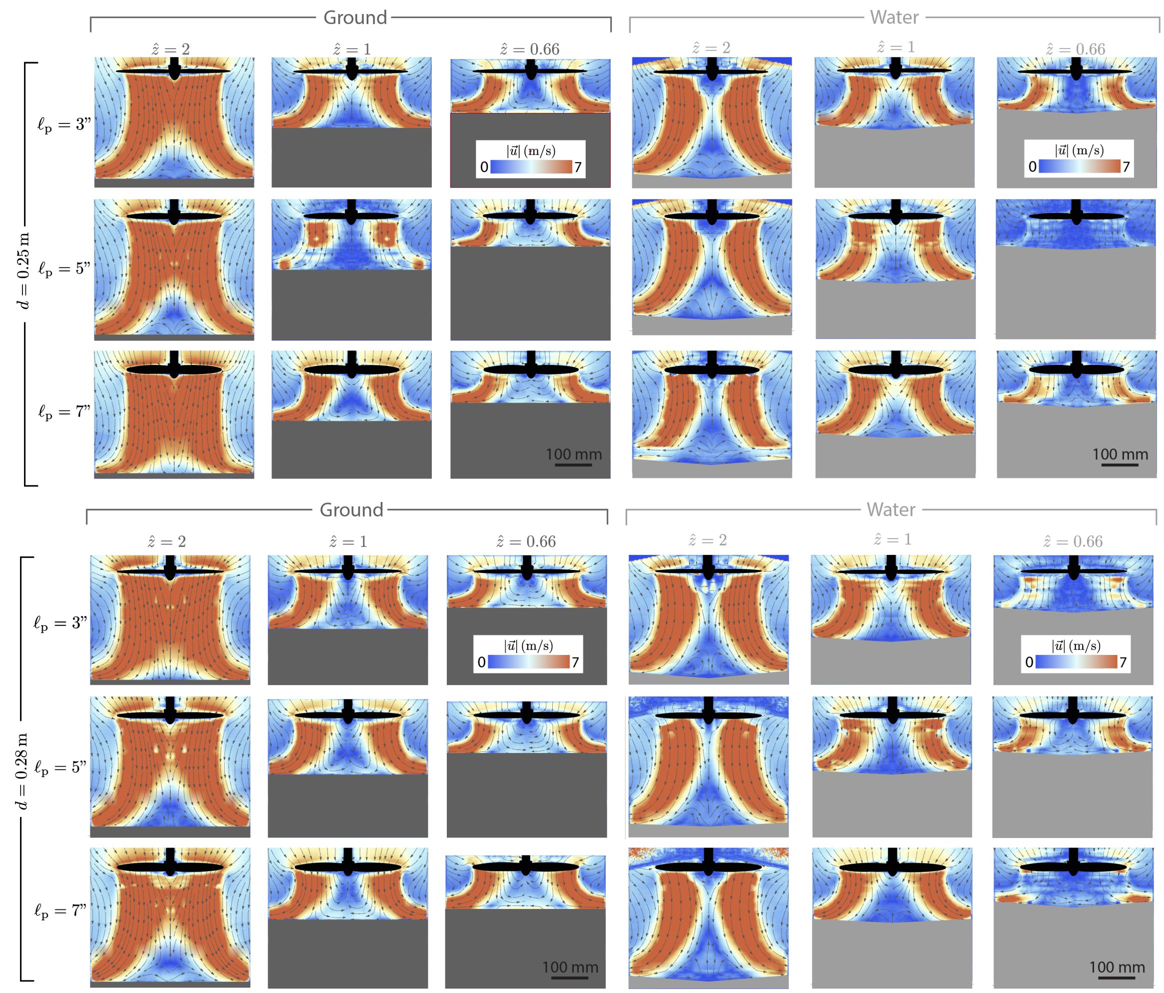

Figure 6.4: Time-Averaged PIV flow fields of for rotor diameters 25 cm & 28 cm at all 3 pitches.

the effects of the displaced water surface, we superimposed all the raw images on top of each other in Figure 6.5. At all three heights, the water's surface curved around the central axis. The deviation was highest for the $\hat{Z}$= 2 cases. The particles are not visible in this image because they are in random locations and therefore superimpose to a smooth grey background.

The momentum jets of wake for water ground effect follow the same trend when a rotor is in solid ground effect. In Figure 6.6, we show a trace of the centerline of the wake jets under the rotor. Due to the ground's presence, the jets are curved upward slightly as they exit the field of view. In the solid ground cases, the jet lines are the same for all the

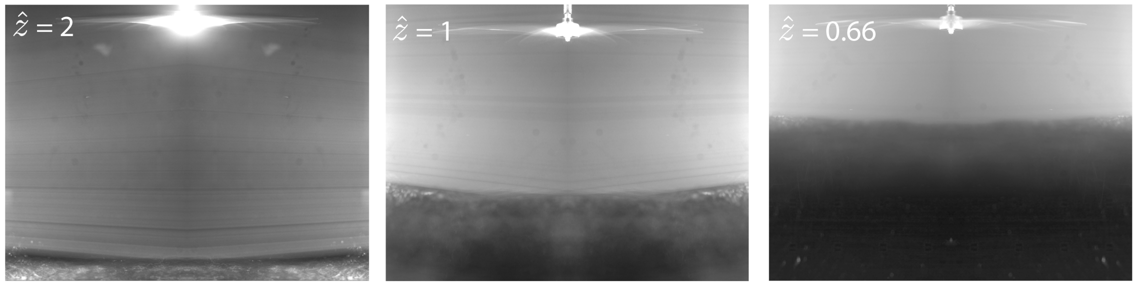

Figure 6.5: Averaged water shape from raw images (photo composite made in Adobe Photoshop).

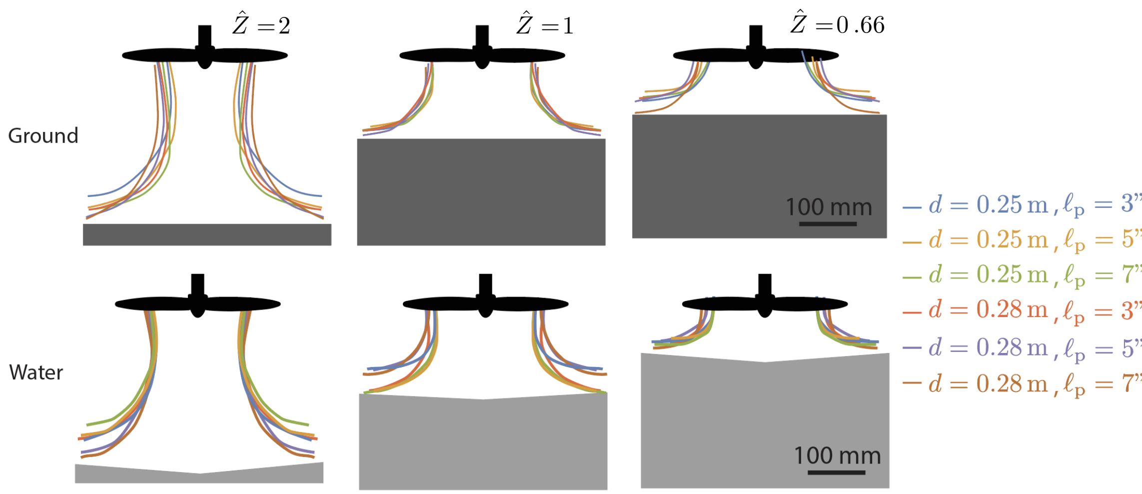

Figure 6.6: Wake jet directions

blades. However, in the water surface cases, there is greater variation in the jet directions and heights where they become angled.

The cross section velocity profiles show that the direction and intensity of the flow depends on distance from the water's surface. In Figure 6.7, we see the velocity cross section 1/6 rotor diameter beneath the rotor plane. As seen in Figure 6.4, the trends across the pitches and diameters are very similar to each other. In the water cases, we see that for the highest $\hat{Z}$ value of 2, the velocity goes to zero on the midplane. The velocity has a higher slope on the endpoints compared to the solid case as well.

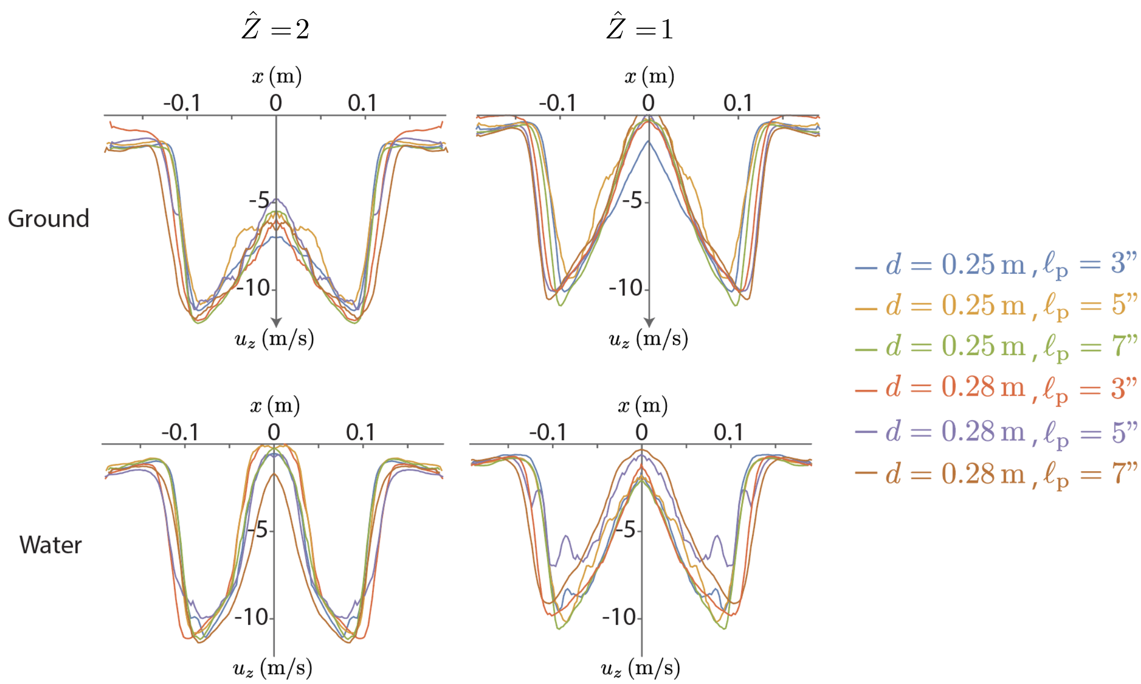

Figure 6.7: Velocity cross sections at two distances between the rotor and the ground and water surface.

6.1.3 Discussion

Water ground effect is less pronounced compared to solid ground effect. In Figure 6.2, the frequency remains relatively constant as $\hat{Z}$ decreases. We expected to see a larger decrease in frequency as the $\hat{Z}$ decreased. In the ground cases, the pitch = 3 inch rotors had decreased at all $\hat{Z}$ levels whereas the water case did not. One reason for this is because the water surface can allow flux of air unlike the solid surface. Due to the flux, the pressure underneath the rotor may be smaller. A trend that is in both data sets is the ordering of pitches, with the smallest pitch corresponding to a higher frequency requirement. The d = 28 cm case for water ground effect is closest in frequency to the model prediction.

Percent error for water ground effect variation was much higher than for solid ground effect. The percent error went from $> 30\%$ to $< 0\%$ for the water percent error. The deformation of the water's surface can lead to a varying distance from the rotor. Also the waves produced on the water's surface can cause more instabilities in the flow compared to a solid ground. The d = 18 cm cases were substantially higher than the other diameters. The model predicted much lower frequency requirements for the requirements of this rotor diameter and payload. There is a small increase in error as the $\hat{Z}$ decreases. This indicates that the ground effect model does not scale at the same rate as the experiment. In d = 25 cm pitch of 7 inch at one $\hat{Z}$, we get an error that is less than 0 showing great alignment. Because the rest of the distances are inline with other data, this is most likely an outlier point. However the pitch of 7 inch blades have the lowest error for most boundary distances.

Average percent errors were aligned for all the cases in water except for d = 18 cm, pitch of 3 & 5 inches. The water cases of d = 20, 25, and 28 cm had a consistent 5-15% error which can be attributed to an offset of the model and/or of the experimental setup. The errors for water are less than ground on average especially for those three diameters. This result suggests that either the model applies better to water surfaces or that water offsets the experimental data more in the direction of the model than in the case of solid ground. The average percent error was more consistent for each diameter blade as the pitch increased or decreased. The near-water condition had 5 cases in which the average error was under 10% compared to only one case in the near-ground condition. The water cases overall had a lower frequency than the solid cases which matched the model's output. Since the payload was the same for both conditions, the near-water effect was stronger in comparison.

In the flow images there is high agreement between the rotor diameters and the pitches of these rotors. The mean flow field and wake structure match what is seen in other ground effect studies. The blade pitch seems to have negligible effect on the structure of the wake. However, the intensity and the velocity tends to change somewhat. In the water case, the major difference is that the stagnation zone is larger for every case in comparison to ground. The $\hat{Z}$ = 2 cases in water have the stagnation zone going all the way to the rotor plane. Although this is a big difference compared to the solid case, the frequencies were comparable in all cases. Presumably the ability for flux at the water surface is changing the pressure in this region in comparison. Although the closest cases in water are distorted due to the waves and splashing the trend in wake shape is consistent.

The water's surface is disturbed by the presence of the rotor. In Figure 6.5, we can see the concave shape that the water's surface develops. By being pushed away, the surface effect may be be lessened because the ground is further away from rotor. On the scale of our experiments, the small deviation in distance did not create a noticeable change in the frequency required to hover. As the rotor approached the ground, we saw the shape of the water decrease the closer the rotor got to the surface. Two factors that lead to a flat average water surface are reduced induced velocity and decreased rotor speed. Ground effect was stronger at that distance, and therefore the rotor speed needed for hovering was lower. The presence of the ground and the lower speed of the rotor caused lower induced velocities. The slower induced velocity translates to slower velocity airflow reaching the surface. The shape of the water's surface affects where the flow can be directed.

The momentum jets in the wake of the rotor flow are altered by the shape of the water's surface. In Figure 6.6, we see how the wake directions in the ground case is different from in the water case. The shape of the water's surface causes the jet to have a higher angle at the ground compared to the comparable ground case. As the water's concaveness decreases with the lower $\hat{Z}$ values, the ground and water momentum jets become similar. The effect of the direction of momentum jets does not have a major impact on the strength of ground effect. The reduction of induced velocity and the stagnation zone and pressure is still prominent in both cases.

The stagnation zone for the water and the ground cases are vastly different. In the water cases when $\hat{Z} = 2$, the velocity at the rotor center approaches zero. Compared to the ground case, the stagnation zone is much higher in the water case than in the ground case. As the rotor approaches the water the wake begins to match the ground case.

6.2 Dual air and water PIV

6.2.1 Experimental Setup: Version 1

There are many phenomena to be discovered at the air water interface to explain the difference in their ground effect. Another important factor is the disturbance a UAV causes underneath the surface of the water. This could disturb a water sampling process [1] which is essential to environment management. To explore how water/air boundary phenomena, I worked with fellow graduate students Christopher Windle & Ke Zhou in Dr. Lin Ma's lab group. To better understand the water and air boundary for rotorcraft, it is necessary to capture flow information from both. In this section we will discuss the approach to conducting PIV in both water and air simultaneously.

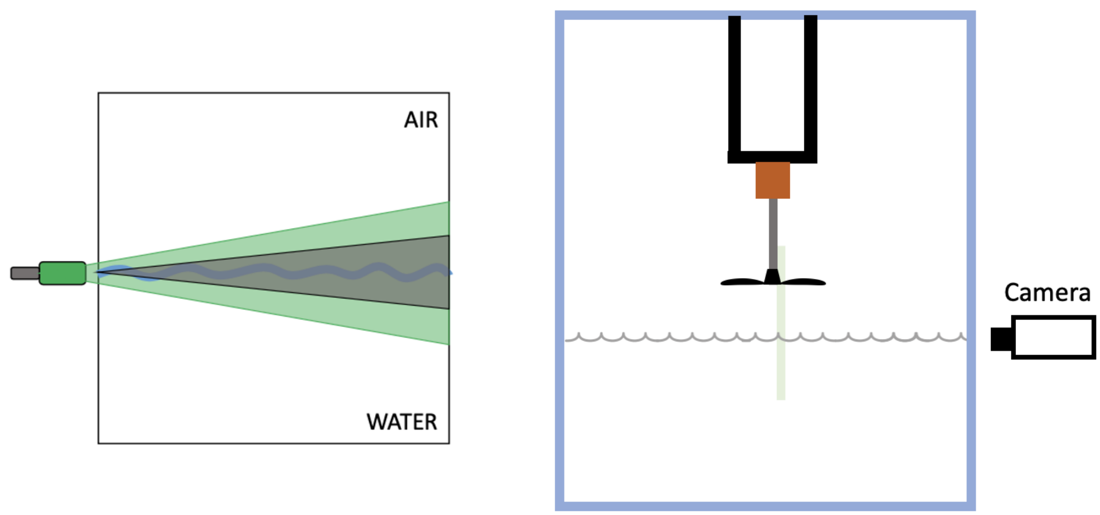

Figure 6.8: Version 1 laser and camera set up.

Our first attempt at dual air and water PIV was unsuccessful. We used the same equipment from Chapter 2. The key components of our equipment was a dual cavity 15 Hz laser and a 1 kHz high speed camera. Four main issues arose from this setup. First the laser was only 15 Hz which is too slow to get time-resolved PIV images which would showcase the transient nature of this boundary flow. The second issue was that the camera was too slow because the rotors were spinning at rotations of ~ 2000 RPM. Third, we used one camera to focus within the testing range. Lastly, the laser generated shadows at the walls of the glass cube seen in Figure 6.8.

The laser was not able to handle the specifications for time-resolved PIV in both air and water. The speed of the laser was too slow to handle the frequency necessary to capture time resolved flow. The laser sheet that was created was too wide and weak to illuminate the particles properly in both mediums. In air the wide laser sheet allowed for too many particles to be illuminated, causing a lower signal to noise ratio for the 2D plane of interest. Lastly, the orientation of the laser sheet was significant because being parallel to the water's surface would allow for shadows to occur from waves at the glass cubes surface.

The camera used originally did not fit the specifications necessary to capture time-resolved PIV simultaneously in both air and water. One camera was not enough to take images in both mediums because they had two different indices of refraction, creating two different focal planes. Another issue was that the camera was not fast enough to capture flow for commercial rotors in hover conditions.

6.2.2 Experimental Setup: Version 2

The issues in Version 1 were addressed in Version 2. Version 2 is shown in Figure 6.2.2. A new camera and laser was used to achieve the performance metrics needed for our time-resolved flow. The orientation of the laser sheet and its output were adjusted to allow for optimal performance. This solution uses two higher speed cameras at different distances to address the index of refraction differences.

The laser orientation and system was carefully chosen to allow for dual air-water PIV. The new laser is a DM Dual Head Green Series and is able to do 60 mJ at 1k Hz surpassing the requirements for our time-resolved flow. The laser has a power rating of 60 mJ enough to illuminate the particles in both fluids. We oriented the laser by moving the optics up and the sheet downward at a angle of ~ $15\deg$ to decrease shadows caused at the glass

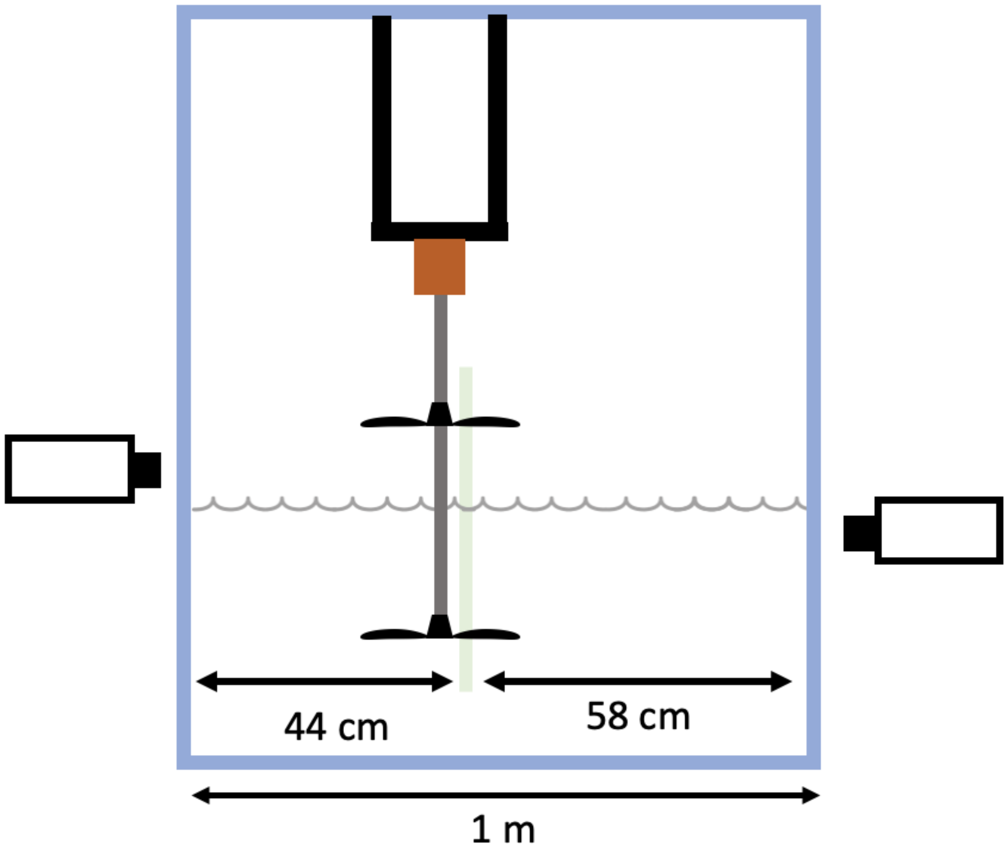

Figure 6.9: Camera set up for dual fluid imaging

surface. However, we do still get some shadow bands from particles on the water surface as the light shines into the water. These are much less pervasive and interpolation of the cross-correlation can account for this.

Two higher performing cameras were necessary to gather data from the flow. Since the index of refraction is different for water and air causing two different focal planes, the water camera has to be 1.3 times the distance away from the plane of interest. The cameras are also faster and can capture images at 3.6k Hz at full resolution.

To measure the flow around the rotor, the PIV system used a dual-cavity pulse laser. The particles in air were glycol and water (diameter 14 µm) and the water particles were glass beads (diameter 20 µm). The laser sheet created a plane just off center ~ $1\,cm$ of the rotors. Particle motion was captured by a high-speed camera at 3.6k Hz. These images were fed into custom cross-correlation software. We took 1800 images (0.5 s of data) to get multiple rotations of the rotor in steady state condition. The result of the averaged cross-correlations is a grid of velocity vectors, one for each 32 x 32 px window.

6.2.3 Results

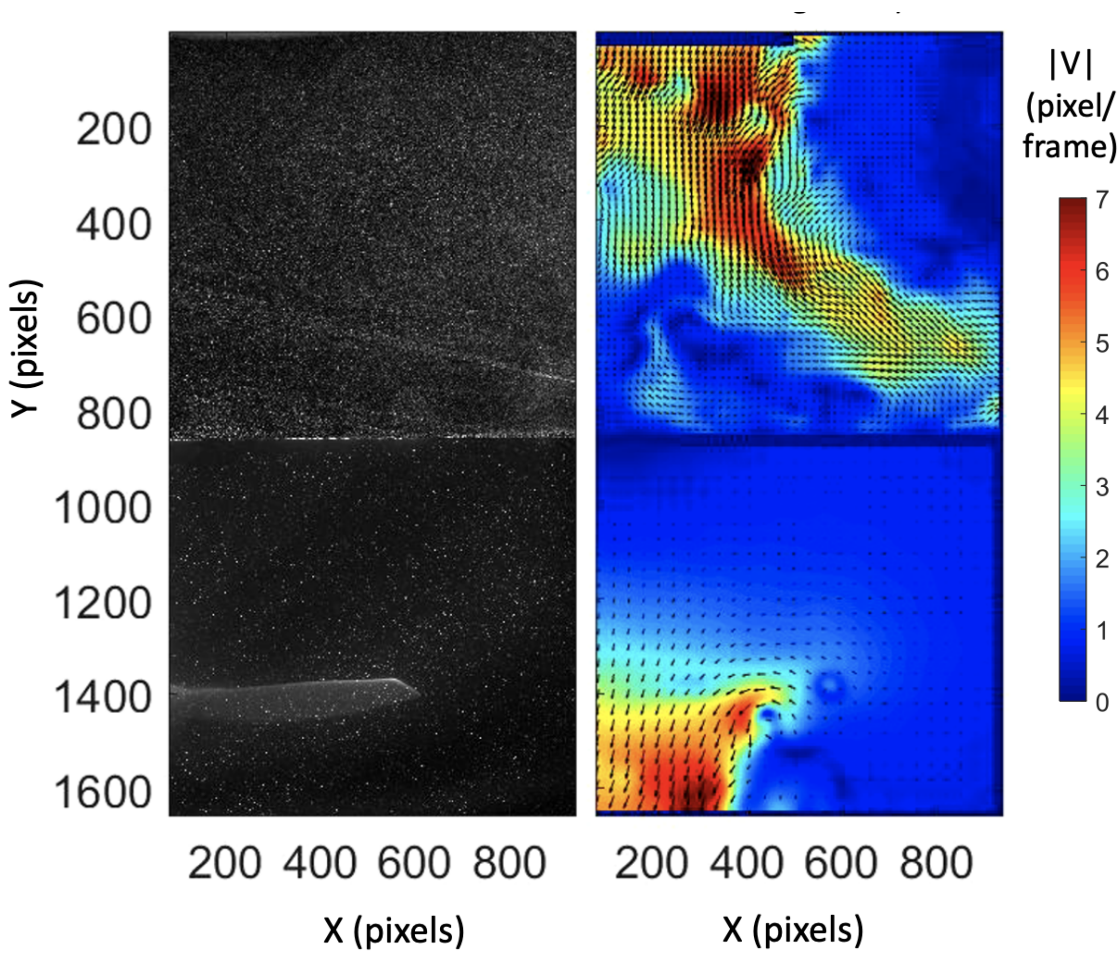

Figure 6.10: Left: Stitched still of seeded flow. Right: Time resolved velocity vector field.

Version 2 of our experiment design was successful in capturing images in both fluids. In Figure 6.10 we show a sample of our seeded flow and corresponding velocity field. Both fluids were uniformly seeded and illuminated. The images and the PIV were stitched together at the water line which is visible in both. Calibration was done by using a clear acrylic sheet with a checkerboard pattern on it. Before taking data we adjusted the magnification so that the pixel to distance ratio was the same in both images. The output of this is seen on the left of Figure 6.10.

The PIV was output from both fluids and aligned with the correct flow field. In Figure 6.10, we showcase a velocity vector field and contour map with the magnitude of the flow. In the top section for the flow image we are seeing a jet curved to the edge of the image because the rotor is in ground effect. This wake jet matches the results we saw early in Section 6.1.2 of a rotor above water in ground effect. Another property we see is a tip vortex confirming the accuracy of this PIV image.

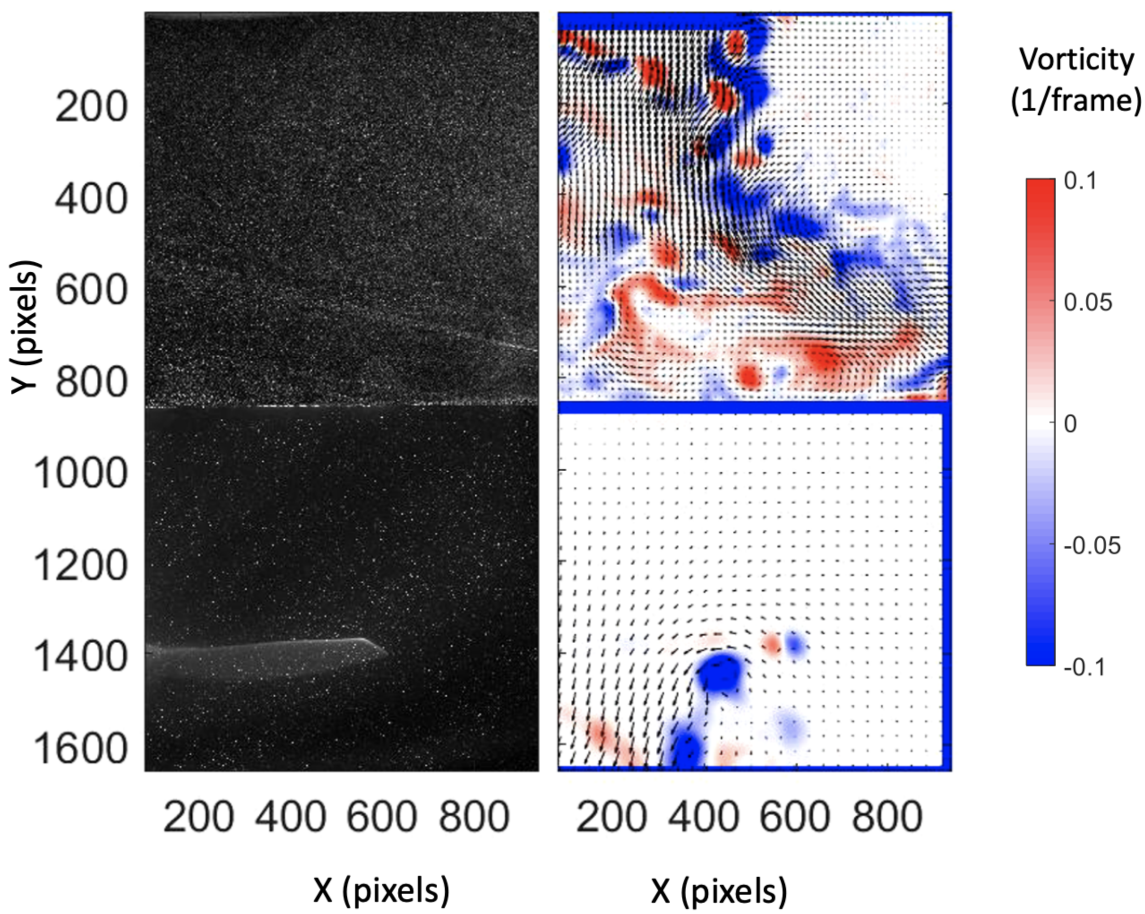

Figure 6.11: Left: Stitched still of seeded flow. Right: Time resolved vorticity field.

Figure 6.11 further confirms the accuracy of our PIV system. The still image is at the same time step as in figure 6.10. The figure shows vorticity in both domains of fluid. Underwater we can see what looks like a tip vortex being created. At the bottom we can see what looks like another vortex that could have been shed already. In the air section we see much more noise within our measurements. The appearance of positive tip vortex that have been shed from the rotor which is located above our field of view. At the water surface we see turbulence and broken up vortices.

6.3 Conclusion

Water ground effect provides comparable lift values at equivalent ground distances to a solid ground. The blade element theory and Cheeseman & Bennett [43] model is more accurate at predicting water ground effect because the frequency required to hover was slightly lower than solid ground effect. The flow images show a concave shape to the water surface dependent on how fast the air velocity was at that point and not a factor of distance. The shape of the water surface influenced the momentum jets direction causing an upward outflow compared to the horizontal flow for a solid case. The stagnation zone for a water ground case is more prominent at further ground distances compared to a solid ground case due to the flux into the water surface. Dual PIV in both a air and water is effect with specific laser location and angle and a time-resolved system.

Chapter 7

Concluding Remarks and Future Work

7.1 Development of Two Arenas for Quantifying Rotorcraft Performance

Our PIV system captures time-averaged flow fields capable of resolving all of our near-boundary flow conditions. The isolated rotor system (Version 2) allows for interchangeable hovering rotors. A counterweight system was designed that allows us to manipulate the hovering rotor's effective payload. The variability in payload allows the system to test different rotor sizes and shapes. The rotor system could successfully move in the lift direction with minimal friction, allowing for testing to be done in free hovering conditions. The Micro Aerial Vehicle arena allowed for the testing of both untethered and tethered MAV systems. The tethered near-boundary testing uses a linear actuator to measure precise boundary distances with a load cell to measure lift forces. The untethered system utilized a series of motion capture cameras allowing the MAV to conduct planned maneuvers within the cube. With the creation of both testing arenas, all of the near-boundary work conducted in this dissertation was made possible. The isolated rotor system can be used in the future for dynamic rotor breaching experiments. The MAV arena is capable of facilitating vehicle interaction studies using multiple untethered MAVs.

7.2 Ground Effect Modeling and Rotor Design Dependency

A simple model was created using Blade Element Theory and a potential flow ground effect model to predict the required hovering frequency of a rotor as it approaches the ground. From the model, we unlocked the relationship between required rotor frequency, hover weight/ thrust, coefficient of thrust, and rotor radius. The error between our model and the experiments was consistent, suggesting a constant correction coefficient may be possible. The rotor's blade pitch seems to have a minimal effect on the accuracy of our models. However, in our experiments the lower RPM/thrust ratio of a lower-pitched rotor tended to increase the influence and prominence of ground effect. Flow images confirm the presence of a stagnation zone under each rotor that grows as the ground distance decreases. The stagnation zone grows all the way past the rotor plane as ground distance decreases and even includes upward flow, suggesting a fountain effect. The cross-section velocity profile sharpens to a triangle shape and decreases amplitude as the rotor approaches the ground.

The results of Chapter 3 formed the basis of the following publications:

- **Carter, D.** & Quinn, D. Rotor property dependencies in air/water ground effect, AIAA Journal, In Preparation.

7.3 Influence of the Ground, Ceiling, and Side Wall on Micro Quadrotors

Micro aerial vehicles demonstrated similar near-boundary effects as those seen in larger flight vehicles. Sidewall boundaries created a negligible change in lift force. The variation between the models and experimental data presumably stems from the difference in vehicle size and shape. Ground effect flow fields indicate a stagnation zone between the rotors while in ground effect. However, there was no sign of reverse flow indicating fountain effect. Flow images show a prominent boundary layer for our MAV platform due to stronger viscous forces. The flow field around an MAV near a ceiling contained an upward-angled inflow, indicating vertically-directed momentum entering the volume and a corresponding lift force on the MAV. At small horizontal tilt angles, there were small alternating vortices in some cases, but overall the ground effect lift remained constant.

The results of Chapter 4 formed the basis of the following publications/presentations:

- **Darius J. Carter**, Lauren Bouchard, and Daniel B. Quinn, "Influence of the Ground, Ceiling, and Sidewall on Micro-Quadrotors, " AIAAJ, Vol. 59, No. 4 (2021), pp. 1398-1405 doi: doi/abs/10.2514/1.J059787.

- **Carter, D.**, Mazzatenta, M, Gao, S, Di Franco, C, Bezzo, N, & Quinn, D. Scaling effects on aerodynamic interactions of rotorcraft around boundaries (Presentation), Meeting of the American Physical Society Division of Fluid Dynamics, November 23rd, 2019

7.4 Near-Boundary Flight Applications

Leveraging the equipment in our lab and partnering labs, we were able to demonstrate a few applications of near-boundary UAV systems. Using experimental from thrust-to-altitude tests, we were able to successfully conduct sensorless landing experiments. Surface-optimized path planning can save energy by harnessing near-boundary flight benefits. In a simple path planning experiment, we were able to demonstrate energy savings of ~ 15% by leveraging ground and ceiling effect. A safety study of near-boundary models showcased how sensitive crash frequencies are to the form of near-boundary models. This sensitivity further highlights the necessity to create physics-based near-boundary models, especially for MAV-scale systems where even millimeter-scale precision can make a difference. Utilizing our PIV to estimate the gust magnitude and direction led to the most accurate model of gust forces from UAV platform. Through our MAV arena, wind estimation testing was performed, suggesting that one could use IMU data to estimate gust conditions on MAV platforms.

The results of Chapter 5 formed the basis of the following publications/presentations:

- S. Gao, C. D. Franco, **D. Carter**, D. Quinn and N. Bezzo. Exploiting Ground and Ceiling Effects on Autonomous UAV Motion Planning, 2019 International Conference on Unmanned Aircraft Systems

- Mazzatenta, M.,**Carter, D.**, and Quinn, D., “Using quadrotor IMU data to estimate wind velocity”, (Poster) Meeting of the American Physical Society Division of Fluid Dynamics 2019

7.5 Rotor property dependencies in solid/water ground effect

Water boundaries provided comparable lift values at equivalent distances to a solid ground. The ground effect blade element theory model is more accurate at predicting water ground effect, because the frequency required to hover was slightly lower than in solid ground effect. Our raw PIV images showed a concave shape of the water surface that was dependent on wake velocity. The water surface shape did not appear to be strong factor of ground distance. The shape of the water surface influenced the direction of the momentum jets, causing an upward outflow compared to the horizontal flow for a solid case. The stagnation zone for a near-water case was more prominent at higher altitudes compared to the solid ground case, presumably due to the flux of air into the water surface. Dual PIV in both air was shown to be possible with high laser heights and angles.

The results of Chapter 6 formed the basis of the following publications:

- **Carter, D.** & Quinn, D. Flow structures of a rotor breaching the water surface. Journal Fluid Mechanics, In Preparation.

7.6 Broader Impacts and Future Work

Gust estimation and multi-vehicle interaction are necessary next steps for improving understanding of MAV flight. The ability to utilize IMU or motor power consumption could revolutionize the HVAC and weather-sensing arenas. MAV platforms provide low cost and agile solutions to sensing, especially indoor sensing. However, before they can safely be allowed to fly indoors with other humans, we need provable safe flight models. Utilizing our MAV arena, future work could be conducted on gust estimation and flow sensing based on the reaction kinematics of a MAV platform. This would allow for a sensorless system which could reduce costs and allow weight sensing. Given the growing interest in indoor and urban air mobility, multi-vehicle interaction studies will inevitably become more common. A low computational cost multi-vehicle interaction simulation solution is necessary for path-planners, which requires more experimental data to train and validate the simulations.

One of the great challenges for amphibious UAUV vehicle design is dealing with breaching of the water surface and transitioning from an underwater vehicle into an aerial vehicle. Maia's UAUV [9] achieved this by using a coaxial rotor UAUV that can ensure that one rotor has transitioned before another (Figure 11). Another group created a buoyant miniature UAUV [56] whose rotors breach the surface at equilibrium. These vehicle designs purposely avoid the transition region due to the chaotic forces placed on the rotor as it experiences the shift between fluids. To understand the flow phenomenon in this transition region, our amphibious rotor arena could be used to conduct flow measurements at this breaching point. To the best of our knowledge, there have been no systematic studies of transitioning rotors. This work would offer UAUV designers better models to consider when designing amphibious rotors. The optimal inter-rotor distance between co-axial rotors, for example, is a design parameter that could be tuned based on our results.

Coaxial rotors are the most common form of multi-rotor UAUV. The purpose of this is to avoid the unstable transition region as the rotor breaches the water surfaces [9]. The coaxial separation distance is a critical design parameter: not only does it affect amphibious transitions, but also it affects performance in hover [57] [58]. At high Reynolds numbers, a single isolated rotor typically out-performs a coaxial rotor in terms of figure of merit [59, 60]. Due to these limitations in performance, a single isolated rotor is generally preferred for UAVs. However, the best solution currently for overcoming the challenging transition region for UAUV flights are coaxial setups. Our amphibious rotor arena could be used for a comprehensive study of the wake interactions of coaxial rotors in the transition region. These studies could combine our current understanding of aerial coaxial rotor performance with the necessary configuration for breaching the water's surface.

Above all, the key contribution of this thesis to the near-boundary flight literature is the development of new theoretical and experimental frameworks for studying near-boundary flight. Understanding the boundary effects and how they complement each other is the next frontier for this field and would be the logical next step with this work. My work on combining Blade Element Theory with a near-ground potential flow model (method of images) offers a way to interpret near-boundary lift data in the context of fundamental physics. Testing these models will require new forms of experimental setups designed specifically for studying small-scale rotors. The two new arenas developed as part of this thesis offer templates for what those types of setups could look like. By incorporating flow-mapping (PIV) into both arenas, I demonstrated how these arenas could be used not just for quantifying rotor performance but also for probing the flow physics that govern the performance. It is my hope that these models and arenas serve as a guide for those studying near-boundary flights in the years ahead.

Bibliography

[1] J.-P. Ore, S. Elbaum, A. Burgin, and C. Detweiler, "Autonomous aerial water sampling," *Journal of Field Robotics*, vol. 32, no. 8, pp. 1095–1113, 2015. eprint: https://onlinelibrary.wiley.com/doi/pdf/10.1002/rob.21591.

[2] W. Stewart, W. Weisler, M. MacLeod, T. Powers, A. Defreitas, R. Gritter, M. Anderson, K. Peters, A. Gopalarathnam, and M. Bryant, "Design and demonstration of a seabird-inspired fixed-wing hybrid uav-uuv system," *Bioinspiration & biomimetics*, vol. 13, no. 5, p. 056 013, 2018.

[3] A. Mohamed, K. Massey, S. Watkins, and R. Clothier, "The attitude control of fixed-wing mavs in turbulent environments," *Progress in Aerospace Sciences*, vol. 66, pp. 37–48, 2014.

[4] S. L. Waslander, G. M. Hoffmann, J. S. Jang, and C. J. Tomlin, "Multi-agent quadrotor testbed control design: Integral sliding mode vs. reinforcement learning," in *2005 IEEE/RSJ International Conference on Intelligent Robots and Systems*, IEEE, 2005, pp. 3712–3717.

[5] T. R. R. Staff and A. Wolf, *Foldable drone could aid search and rescue missions*, 2018.

[6] C. Koparan, A. B. Koc, C. V. Privette, and C. B. Sawyer, "In situ water quality measurements using an unmanned aerial vehicle (uav) system," *Water*, vol. 10, no. 3, p. 264, 2018.

[7] *Elios indoor drone bridge inspection - case study*, 2019.

[8] P. b. t. o. 2020-08-032020-08-03 and Transcendfpv, *How to waterproof a drone from snow, water, humidity and more!* 2020.

[9] M. M. Maia, P. Soni, and F. J. Diez, "Demonstration of an aerial and submersible vehicle capable of flight and underwater navigation with seamless air-water transition," *arXiv preprint arXiv:1507.01932*, 2015.

[10] R. Baudinette and K Schmidt-Nielsen, "Energy cost of gliding flight in herring gulls," *Nature*, vol. 248, no. 5443, pp. 83–84, 1974.

[11] J. M. Rayner, "On the aerodynamics of animal flight in ground effect," *Philosophical Transactions of the Royal Society of London. Series B: Biological Sciences*, vol. 334, no. 1269, pp. 119–128, 1991.

[12] H. Park and H. Choi, "Aerodynamic characteristics of flying fish in gliding flight," *Journal of Experimental Biology*, vol. 213, no. 19, pp. 3269–3279, 2010.

[13] I. Cheeseman and W. Bennett, “The effect of the ground on a helicopter rotor,” *R & M*, vol. 3021, 1957.

[14] Y. H. Hsiao and P. Chirarattananon, “Ceiling effects for surface locomotion of small rotorcraft,” in *2018 IEEE/RSJ International Conference on Intelligent Robots and Systems (IROS)*, IEEE, 2018, pp. 6214–6219.

[15] Z. Ning, R. W. Wlezien, and H. Hu, “An experimental study on small uav propellers with serrated trailing edges,” in *47th AIAA Fluid Dynamics Conference*, 2017, p. 3813.

[16] P. Sanchez-Cuevas, G. Heredia, and A. Ollero, “Characterization of the aerodynamic ground effect and its influence in multirotor control,” *International Journal of Aerospace Engineering*, vol. 2017, 2017.

[17] Y. H. Hsiao and P. Chirarattananon, “Ceiling effects for hybrid aerial-surface locomotion of small rotorcraft,” *arXiv preprint arXiv:1905.04632*, 2019.

[18] D. J. Pines and F. Bohorquez, “Challenges facing future micro-air-vehicle development,” *Journal of aircraft*, vol. 43, no. 2, pp. 290–305, 2006.

[19] S. Yoon, P. V. Diaz, D. D. Boyd Jr, W. M. Chan, and C. R. Theodore, “Computational aerodynamic modeling of small quadcopter vehicles,” in *American Helicopter Society (AHS) 73rd Annual Forum Fort Worth, Texas*, 2017.

[20] S. Yoon, H. C. Lee, and T. H. Pulliam, “Computational analysis of multi-rotor flows,” in *54th AIAA Aerospace Sciences Meeting*, 2016, p. 0812.

[21] W. Zhou, Z. Ning, H. Li, and H. Hu, “An experimental investigation on rotor-to-rotor interactions of small uav propellers,” in *35th AIAA Applied Aerodynamics Conference*, 2017, p. 3744.

[22] P. Sanchez-Cuevas, G Heredia, and A Ollero, “Multirotor uas for bridge inspection by contact using the ceiling effect,” in *2017 International Conference on Unmanned Aircraft Systems (ICUAS)*, IEEE, 2017, pp. 767–774.

[23] C. Powers, D. Mellinger, A. Kushleyev, B. Kothmann, and V. Kumar, “Influence of aerodynamics and proximity effects in quadrotor flight,” in *Experimental robotics*, Springer, 2013, pp. 289–302.

[24] S. Shen, N. Michael, and V. Kumar, “Autonomous multi-floor indoor navigation with a computationally constrained mav,” in *2011 IEEE International Conference on Robotics and Automation*, IEEE, 2011, pp. 20–25.

[25] S. A. Conyers, M. J. Rutherford, and K. P. Valavanis, “An empirical evaluation of ceiling effect for small-scale rotorcraft,” in *2018 International Conference on Unmanned Aircraft Systems (ICUAS)*, IEEE, 2018, pp. 243–249.

[26] I Sharf, M Nahon, A Harmat, W Khan, M Michini, N Speal, M Trentini, T Tsadok, and T Wang, “Ground effect experiments and model validation with draganflyer x8 rotorcraft,” in *2014 International Conference on Unmanned Aircraft Systems (ICUAS)*, IEEE, 2014, pp. 1158–1166.

[27] A. Kushleyev, D. Mellinger, C. Powers, and V. Kumar, "Towards a swarm of agile micro quadrotors," *Autonomous Robots*, vol. 35, no. 4, pp. 287–300, 2013.

[28] (2016). "A roadmap for US Robotics: 2016 Edition."

[29] A. Cesetti, E. Frontoni, A. Mancini, P. Zingaretti, and S. Longhi, "A vision-based guidance system for uav navigation and safe landing using natural landmarks," *Journal of intelligent and robotic systems*, vol. 57, no. 1-4, p. 233, 2010.

[30] G. Spedding and P. Lissaman, "Technical aspects of microscale flight systems," *Journal of Avian Biology*, pp. 458–468, 1998.

[31] B. Theys, G. Dimitriadis, T. Andrianne, P. Hendrick, and J. De Schutter, "Wind tunnel testing of a vtol mav propeller in tilted operating mode," in *2014 International conference on unmanned aircraft systems (ICUAS)*, IEEE, 2014, pp. 1064–1072.

[32] D. Lee, A. Awan, S. Kim, and H. J. Kim, "Adaptive control for a vtol uav operating near a wall," in *AIAA Guidance, Navigation, and Control Conference*, 2012, p. 4835.

[33] B. B. Kocer, T. Tjahjowidodo, and G. G. L. Seet, "Centralized predictive ceiling interaction control of quadrotor vtol uav," *Aerospace Science and Technology*, vol. 76, pp. 455–465, 2018.

[34] B. J. Emran and H. Najjaran, "A review of quadrotor: An underactuated mechanical system," *Annual Reviews in Control*, vol. 46, pp. 165–180, 2018.

[35] P.-J. Bristeau, P. Martin, E. Salaün, and N. Petit, "The role of propeller aerodynamics in the model of a quadrotor uav," in *2009 European Control Conference (ECC)*, IEEE, 2009, pp. 683–688.

[36] S. Waslander and C. Wang, "Wind disturbance estimation and rejection for quadrotor position control," in *AIAA Infotech@ Aerospace conference and AIAA unmanned... Unlimited conference*, 2009, p. 1983.

[37] H. Nobahari and A. Sharifi, "Continuous ant colony filter applied to online estimation and compensation of ground effect in automatic landing of quadrotor," *Engineering Applications of Artificial Intelligence*, vol. 32, pp. 100–111, 2014.

[38] L. Danjun, Z. Yan, S. Zongying, and L. Geng, "Autonomous landing of quadrotor based on ground effect modelling," in *2015 34th Chinese Control Conference (CCC)*, IEEE, 2015, pp. 5647–5652.

[39] S. Gao, C. Di Franco, D. Carter, D. Quinn, and N. Bezzo, "Exploiting ground and ceiling effects on autonomous uav motion planning," in *2019 International Conference on Unmanned Aircraft Systems (ICUAS)*, IEEE, 2019, pp. 768–777.

[40] B. Bahadir Kocer, M. Efe Tiryaki, M. Pratama, T. Tjahjowidodo, and G. G. L. Seet, "Aerial robot control in close proximity to ceiling: A force estimation-based nonlinear mpc," *arXiv*, arXiv–1907, 2019.

[41] A. E. Jimenez-Cano, P. J. Sanchez-Cuevas, P. Grau, A. Ollero, and G. Heredia, "Contact-based bridge inspection multirotors: Design, modeling, and control considering the ceiling effect," *IEEE Robotics and Automation Letters*, vol. 4, no. 4, pp. 3561–3568, 2019.

[42] M. Taber and J. McCabe, “Helicopter ditching: Time of crash and survivability,” *SAFE Journal*, vol. 34, pp. 5–10, Sep. 2006.

[43] I. Cheeseman and W. Bennett, “The effect of ground on a helicopter rotor in forward flight,” 1955.

[44] *Blade element propeller theory*.

[45] J. S. Hayden, “The effect of the ground on helicopter hovering power required,” in *Proc. AHS 32nd Annual Forum*, 1976.

[46] B. Landry and Others, “Planning and control for quadrotor flight through cluttered environments,” Ph.D. dissertation, Massachusetts Institute of Technology, 2015.

[47] A. Gautam, P. Sujit, and S. Saripalli, “A survey of autonomous landing techniques for uavs,” in *2014 international conference on unmanned aircraft systems (ICUAS)*, IEEE, 2014, pp. 1210–1218.

[48] N. Bezzo, K. Mohta, C. Nowzari, I. Lee, V. Kumar, and G. Pappas, “Online planning for energy-efficient and disturbance-aware uav operations,” in *2016 IEEE/RSJ International Conference on Intelligent Robots and Systems (IROS)*, IEEE, 2016, pp. 5027–5033.

[49] C. Di Franco and G. Buttazzo, “Coverage path planning for uavs photogrammetry with energy and resolution constraints,” *Journal of Intelligent & Robotic Systems*, vol. 83, no. 3-4, pp. 445–462, 2016.

[50] B. McCormick, *Aerodynamics, Aeronautics, and Flight Mechanics*, 2nd Editio. John Wiley & Sons, 1995.

[51] S. Bouabdallah and R. Siegwart, “Full control of a quadrotor,” in *2007 IEEE/RSJ International Conference on Intelligent Robots and Systems*, Ieee, 2007, pp. 153–158.

[52] D. Mellinger and V. Kumar, “Minimum snap trajectory generation and control for quadrotors,” in *IEEE International Conference on Robotics and Automation*, 2011, pp. 2520–2525.

[53] E. Yel, T. X. Lin, and N. Bezzo, “Computation-aware adaptive planning and scheduling for safe unmanned airborne operations,” *Journal of Intelligent & Robotic Systems*, vol. 100, no. 2, pp. 575–596, 2020.

[54] C. S. Subudhi and D Ezhilarasi, “Modeling and trajectory tracking with cascaded pd controller for quadrotor,” *Procedia computer science*, vol. 133, pp. 952–959, 2018.

[55] D. J. Carter, L. Bouchard, and D. B. Quinn, “Influence of the ground, ceiling, and sidewall on micro-quadrotors,” *AIAA Journal*, vol. 59, no. 4, pp. 1398–1405, 2021.

[56] J. Zha, E. Thacher, J. Kroeger, S. A. Mäkiharju, and M. W. Mueller, “Towards breaching a still water surface with a miniature unmanned aerial underwater vehicle,” in *2019 International Conference on Unmanned Aircraft Systems (ICUAS)*, 2019, pp. 1178–1185.

[57] T. Nagashima and K. Nakanishi, “Optimum performance and wake geometry of coaxial rotor in hover,” 1981.

[58] S. Sunada, K. Tanaka, and K. Kawashima, “Maximization of thrust-torque ratio of a coaxial rotor,” *Journal of Aircraft*, vol. 42, pp. 570–572, Mar. 2005.

[59] J. G. Leishman and M. Syal, “Figure of merit definition for coaxial rotors,” *Journal of the American Helicopter Society*, vol. 53, no. 3, pp. 290–300, 2008.

[60] D. Shukla and N. Komerath, “Drone Scale Coaxial Rotor Aerodynamic Interactions Investigation,” *Journal of Fluids Engineering*, vol. 141, no. 7, Jan. 2019, 071106. eprint: `https://asmedigitalcollection.asme.org/fluidsengineering/article-pdf/141/7/071106/6061910/fe\_141\_07\_071106.pdf`.